

---


Electronic Theses and Dissertations, 2004-2019

---

2006

## Fundamental Aspects Of Regenerative Cerium Oxide Nanoparticles And Their Applications In Nanobiotechnology

Swanand Patil  
*University of Central Florida*

 Part of the [Materials Science and Engineering Commons](#)  
Find similar works at: <https://stars.library.ucf.edu/etd>  
University of Central Florida Libraries <http://library.ucf.edu>

This Doctoral Dissertation (Open Access) is brought to you for free and open access by STARS. It has been accepted for inclusion in Electronic Theses and Dissertations, 2004-2019 by an authorized administrator of STARS. For more information, please contact [STARS@ucf.edu](mailto:STARS@ucf.edu).

---

### STARS Citation

Patil, Swanand, "Fundamental Aspects Of Regenerative Cerium Oxide Nanoparticles And Their Applications In Nanobiotechnology" (2006). *Electronic Theses and Dissertations, 2004-2019*. 1094.  
<https://stars.library.ucf.edu/etd/1094>

FUNDAMENTAL ASPECTS OF REGENERATIVE CERIUM OXIDE NANOPARTICLES  
AND THEIR APPLICATIONS IN NANOBIO TECHNOLOGY

by

SWANAND D. PATIL  
B.E. University of Pune, 1999  
M.S. University of Central Florida, 2003

A dissertation submitted in partial fulfillment of the requirements  
for the degree of Doctor of Philosophy  
in the Department of Mechanical, Materials and Aerospace Engineering  
in the College of Engineering and Computer Science  
at the University of Central Florida  
Orlando, Florida

Summer Term  
2006

Major Professor: Sudipta Seal

©2006 Swanand Patil

## ABSTRACT

Cerium oxide has been used extensively for various applications over the past two decades. The use of cerium oxide nanoparticles is beneficial in present applications and can open avenues for future applications. The present study utilizes the microemulsion technique to synthesize uniformly distributed cerium oxide nanoparticles. The same technique was also used to synthesize cerium oxide nanoparticles doped with trivalent elements (La and Nd).

The fundamental study of cerium oxide nanoparticles identified variations in properties as a function of particle size and also due to doping with trivalent elements (La and Nd). It was found that the lattice parameter of cerium oxide nanoparticles increases with decrease in particle size. Also Raman allowed mode shift to lower energies and the peak at  $464\text{ cm}^{-1}$  becomes broader and asymmetric. The size dependent changes in cerium oxide were correlated to increase in oxygen vacancy concentration in the cerium oxide lattice.

The doping of cerium oxide nanoparticles with trivalent elements introduces more oxygen vacancies and expands the cerium oxide lattice further (in addition to the lattice expansion due to the size effect). The lattice expansion is greater for La-doped cerium oxide nanoparticles compared to Nd-doping due to the larger ionic radius of La compared to Nd, the lattice expansion is directly proportional to the dopant concentration.

The synthesized cerium oxide nanoparticles were used to develop an electrochemical biosensor of hydrogen peroxide ( $\text{H}_2\text{O}_2$ ). The sensor was useful to detect  $\text{H}_2\text{O}_2$  concentrations as low as  $1\mu\text{M}$  in water. Also the preliminary testing of the sensor on tomato stem and leaf extracts indicated that the sensor can be used in practical applications such as plant physiological studies etc.

The nanomolar concentrations of cerium oxide nanoparticles were also found to be useful in decreasing ROS (reactive oxygen species) mediated cellular damages in various *in vitro* cell cultures. Cerium oxide nanoparticles reduced the cellular damages to the normal breast epithelial cell line (CRL 8798) induced by X-rays and to the Keratinocyte cell line induced by UV irradiation. Cerium oxide nanoparticles were also found to be neuroprotective to adult rat spinal cord and retinal neurons.

We propose that cerium oxide nanoparticles act as free radical scavenger (via redox reactions on its surface) to decrease the ROS induced cellular damages. Additionally, UV-visible spectroscopic studies indicated that cerium oxide nanoparticles possess auto-regenerative property by switching its oxidation state between  $\text{Ce}^{3+}$  and  $\text{Ce}^{4+}$ . The auto-regenerative antioxidant property of these nanoparticles appears to be a key component in all the biological applications discussed in the present study.

## **ACKNOWLEDGMENTS**

I wish to thank my faculty advisor, Prof. Sudipta Seal, for providing me the support and giving me an opportunity to work on various interesting projects during my course of study and research at UCF. Without his motivation and guidance this research work would not have been possible.

I am very grateful to Dr. Hyung J. Cho and his graduate student, Anjum Mehta, for designing and developing the MEMS based hydrogen peroxide sensor of cerium oxide nanoparticles. I also thank Dr. Cho for being on my thesis committee. I would like to thank Dr. Alfons Schulte for being on my thesis committee and his student Yu Guo for his assistance with the Raman spectroscopic study of the nanoparticles.

I am also thankful to Dr. Roy Tarnuzzer, Dr. William Self, Dr. James F. McGinnis, Dr. James J. Hickman and Mainak Das for various biological studies of cerium oxide nanoparticles and useful discussion. My sincere thanks to Drs. Ray Bucklin and Melanie Correll for providing the tomato plant cells for the hydrogen peroxide detection studies.

My sincere thanks to Dr. Helge Heinrich for being on my thesis committee and thoroughly evaluating this thesis and suggesting useful corrections. I also thank Dr. Samar Kalita for being on my thesis committee and evaluating this work.

I thank Materials Characterization Facility (MCF) at UCF for offering the characterization facilities required for conducting this research work. Also, I would like to acknowledge all

the students in the Surface Engineering and Nanotechnology Facility (SNF) and my friends for their cooperation and support.

I am grateful for financial support by NIH (R01AG022617), NSF (BES0541516) and UF-UCF space research initiative. Most of all, I would like to thank my parents and brother for all their love and for always being there for me.

## TABLE OF CONTENTS

LIST OF FIGURES.....	x
LIST OF TABLES.....	xiii
LIST OF ABBREVIATIONS.....	xiv
CHAPTER 1. INTRODUCTION.....	1
1.1. Nanotechnology: Introduction and Significance.....	1
1.2. Cerium Oxide: Background and Motivation.....	2
1.3. Organization.....	4
CHAPTER 2. SYNTHESIS OF CERIUM OXIDE NANOPARTICLES.....	6
2.1. Introduction.....	6
2.2. Microemulsion Process for Nanoparticles Synthesis.....	8
2.2.1. Thermodynamics of Micelle Formation and Microemulsion.....	8
2.2.2. Nanoparticles Synthesis.....	10
2.3. Cerium Oxide Synthesis using the Microemulsion Process.....	15
2.3.1. Cerium Oxide Nanoparticles Synthesis.....	17
2.3.2. Doping of Cerium Oxide Nanoparticles with Trivalent Elements.....	20
CHAPTER 3. PROPERTIES OF CERIUM OXIDE NANOPARTICLES.....	24
3.1. Introduction.....	24
3.2. Size Dependent Variation in Properties of Cerium Oxide Nanoparticles.....	25
3.2.1. X-ray Diffraction Studies.....	25
3.2.2. Raman Spectroscopic Analysis.....	27
3.3. Effect of Doping with Trivalent Elements.....	33



3.3.1. X-ray Diffraction Studies.....	34
3.3.2. Raman Spectroscopic Analysis.....	36
3.4. Conclusions.....	42
CHAPTER 4. ELECTROCHEMICAL BIOSENSOR FOR HYDROGEN PEROXIDE DETECTION .....	43
4.1. Introduction.....	43
4.2. Role of Hydrogen Peroxide in Biological Systems.....	44
4.3. Hydrogen Peroxide Detection.....	46
4.3.1. Importance .....	46
4.3.2. Current Detection Techniques and Their Limitations .....	47
4.3.2.1. Horse Radish Peroxidase – Linked Assays.....	47
4.3.2.2. Dichlorofluorescein Fluorescence.....	49
4.3.2.3. Ferrithiocyanate.....	50
4.3.2.4. Electrochemical Sensors .....	50
4.4. Nanocrystalline Cerium Oxide Based Biosensor for H <sub>2</sub> O <sub>2</sub> Detection .....	53
4.4.1. Sensor Design, Fabrication and Characterization.....	53
4.4.2. Sensor Test Results and Discussion.....	60
4.4.3. Regenerative Property of Cerium Oxide Nanoparticles.....	67
4.5. Conclusion.....	69
CHAPTER 5. APPLICATIONS OF CERIUM OXIDE NANOPARTICLES IN BIOLOGY	70
5.1. Introduction.....	70
5.1.1. Nanotechnology in Biomedical Applications.....	70
5.1.2. Reactive Oxygen Species (ROS): Role in Biology .....	71
5.1.3. Free Radical Scavengers .....	72
5.1.4. Cerium Oxide Nanoparticles as Free Radical Scavenger .....	73

5.2. Radioprotection to Normal Cells in Cancer Treatment.....	74
5.2.1. Radiation Therapy in Cancer Treatment .....	74
5.2.2. Experimental Results .....	75
5.2.3. Discussion .....	80
5.3. UV protection to Human Keratinocyte Cells.....	82
5.3.1. Toxic Effects of UV Radiation on the Skin: Role of ROS and Its Control.....	82
5.3.2. Experimental Results and Discussion .....	84
5.4. Neuroprotection to Adult Spinal Cord Neurons in Culture.....	86
5.4.1. Introduction .....	86
5.4.2. Experimental Results .....	87
5.4.3. Discussion .....	90
5.5. Neuroprotection in Retinal Cells .....	91
5.5.1. Introduction .....	91
5.5.2. Experimental Results and Discussion .....	92
5.6. Role of Cerium Oxide Nanoparticles in Radical Induced Cellular Damage Protection .....	95
CHAPTER 6. CONCLUSIONS .....	98
6.1. Fundamental Studies of Cerium Oxide Nanoparticles .....	98
6.2. Cerium Oxide Nanoparticles Based Biosensor of H <sub>2</sub> O <sub>2</sub> .....	98
6.3. Biological Applications of Cerium Oxide Nanoparticles .....	99
REFERENCES.....	100

## LIST OF FIGURES

Figure 2.1. Mechanism of synthesis of nanoparticles using mixing of microemulsions .	12
Figure 2.2. Mechanism of synthesis of nanoparticles using single microemulsion .....	13
Figure 2.3. Ternary phase diagram of water/AOT/isooctane system determined using experimental method <sup>49</sup> .....	16
Figure 2.4. Micelle size distribution curve for the synthesized cerium oxide nanoparticles containing sol measured using particle size analyzer.....	18
Figure 2.5. HRTEM images of the synthesized cerium oxide nanoparticles with particle size of (a) 3-5 nm and (b) 25-30 nm.....	19
Figure 2.6. HRTEM images of doped nanoceria samples. (a) CeO <sub>2</sub> - 1, (b) CeO <sub>2</sub> - 2, (c) CeO <sub>2</sub> - 3, (d) CeO <sub>2</sub> - 4, (e) CeO <sub>2</sub> - 5, and (f) CeO <sub>2</sub> - 6.....	23
Figure 3.1. XRD plots of ceria nanoparticles with varying particle size .....	26
Figure 3.2. Raman spectra of ceria nanoparticles for different particle sizes obtained experimentally (dotted line) and also from the curve fit according to the spatial correlation model (solid line) .....	29
Figure 3.3. Phonon dispersion curves for cerium oxide obtained using a rigid ion model from reference <sup>67</sup> (dotted lines) and the fitted data (solid lines).....	32
Figure 3.4. (a) XRD spectra of all the doped nanoceria samples. (b) Lattice parameter variation of the nanoceria samples as a function of doping amount.....	35
Figure 3.5. Raman spectra of (a) La- and (b) Nd-doped nanoceria samples obtained experimentally (dotted line) and also from the curve fit according to the spatial correlation model (solid line); (c) Raman peak shift of the nanoceria samples as a function of doping amount.....	40
Figure 3.6. (a) The correlation length and (b) oxygen vacancies concentration of the nanoceria samples as a function of doping amount .....	41
Figure 4.1. Schematic of the 3-terminal H <sub>2</sub> O <sub>2</sub> sensor design .....	54
Figure 4.2. Stepwise fabrication process for hydrogen peroxide sensor .....	56
Figure 4.3. Photograph of the fabricated wafer showing multiple sensors .....	57

Figure 4.4. SEM images of the fabricated hydrogen peroxide sensor (a) overall sensor and (b) working electrode.....	58
Figure 4.5. Cross sectional analysis of the working electrode studied using focused ion beam technique (a) Trench cut in the sensor working electrode and (b) cross section of the working electrode .....	59
Figure 4.6. Cyclic voltammogram of the nanoceria coated sensor in 1 mM H <sub>2</sub> O <sub>2</sub> solution in water.....	63
Figure 4.7. (a) Potentiostatic response of the nanoceria coated sensor for 0.1 mM H <sub>2</sub> O <sub>2</sub> concentration; (b) Potentiostatic current Vs H <sub>2</sub> O <sub>2</sub> concentration response of the nanoceria coated sensor, The inset graph is an enlargement of the low H <sub>2</sub> O <sub>2</sub> concentration region. The applied potential was 0.20 V .....	64
Figure 4.8. (a) Cyclic voltammograms of healthy stem and leaf extracts from a tomato plant; (b) Potentiostatic currents from the healthy and UV radiated stem (applied voltage: 0.60 V) and leaf (applied voltage: 0.35 V) extracts from a tomato plant. ....	66
Figure 4.9. Study of regenerative property of cerium oxide nanoparticles using UV-visible spectroscopy .....	68
Figure 5.1. Cytotoxicity of cerium oxide nanoparticles on CRL8798 and MCF-7 cell lines in culture.....	77
Figure 5.2. Dose response for ionizing radiation and effect on cell viability for MCF-7 cell line.....	77
Figure 5.3. Cell viability of (a) CRL8798 and (b) MCF-7 cell lines either with or without 10 nM cerium oxide nanoparticles treatment at 48 hrs after 10 Gy irradiation. ....	78
Figure 5.4. TUNEL staining of CRL8798 and MCF-7 cell lines either with or without 10 nM cerium oxide nanoparticles treatment at 48 hrs after 10 Gy irradiation studied using light microscopy (The arrows denote TUNEL positive apoptotic nuclei).....	79
Figure 5.5. TUNEL staining data for, adherent and non-adherent cells, of CRL8798 and MCF-7 cell lines either with or without 10 nM cerium oxide nanoparticles treatment at 48 hrs after 10 Gy irradiation.....	80
Figure 5.6. Cell viability of keratinocytes to UVA-B radiation induces damage to varying concentrations of cerium oxide nanoparticles treatment .....	85
Figure 5.7. Live-dead cell assay indicated that Cerium oxide treated cultures had significantly higher cell survival and significantly less cell death at day 15 and day 30 in culture as compared to the control cultures (*p < 0.05; **p < 0.01).....	89

Figure 5.8. Neuron-glia cell assays indicated that a significantly high neuronal survival in Ceria treated culture at day 15 and day 30 as compared to the control cultures (\* p < 0.05; \*\* p < 0.01) ..... 89

Figure 5.9. Live-dead cell assay after hydrogen peroxide treatment indicated that Cerium oxide treated cultures had significantly higher number of surviving cells as compared to the control (\*p < 0.05; \*\*p < 0.01) ..... 90

Figure 5.10. Percentage of apoptotic retinal neurons in culture with/without 5nM CeO<sub>2</sub> nanoparticle treatment at different time intervals (n=3, \*p < 0.05, \*\*p < 0.01) ..... 93

Figure 5.11. Relative viable retinal neurons with/without 5nM CeO<sub>2</sub> nanoparticle treatment at different time intervals for H<sub>2</sub>O<sub>2</sub> induced apoptosis, studied using flow cytometry (n=3, \*p < 0.05, \*\*p < 0.01) ..... 94

Figure 5.12. ROS generation in retinal neurons with/without 5nM CeO<sub>2</sub> nanoparticle treatment at different time intervals studied via oxidized DAFH-DC fluorescence density (n=3, \*p < 0.05, \*\*p < 0.01) ..... 95

## LIST OF TABLES

Table 2.1. Details of the samples doped with La and Nd .....	22
Table 3.1. Summary of size dependent changes in the properties of cerium oxide samples.....	27

## LIST OF ABBREVIATIONS

AMD	Age-related macular degeneration
AOT	Sodium bis(2-ethylhexyl) sulfosuccinate
CeO <sub>2</sub>	Cerium oxide
CNS	Central nervous system
CNT	Carbon nanotube
CNTF	Ciliary neurotrophic factor
CV	Cyclic voltammetry
DCF	2'-7'-dichlorofluorescein
DCFH	2'-7'-dichlorofluorescein
DLS	Dynamic light scattering
FBS	Fetal bovine serum
FIB	Focused ion beam
H <sub>2</sub> O <sub>2</sub>	Hydrogen peroxide
HMTA	Hexamethylenetetramine
HRP	Horse radish peroxidase
HRTEM	High Resolution Transmission Electron Microscopy
MB	Methylene blue
NER	Nucleotide excision repair
O/W	Oil in Water
PCD	Programmed cell death
ROS	Reactive oxygen species

SEM	Scanning electron microscopy
SOD	Superoxide dismutase
TEM	Transmission electron microscopy
TMB	Tetramethyl benzidine
UV	Ultraviolet
W/O	Water in Oil
$W_0$	water to surfactant molar ration ( $[H_2O]/[AOT]$ )
XPS	X-ray Photoelectron Spectroscopy
XRD	X-ray Diffraction



# CHAPTER 1. INTRODUCTION

## 1.1. Nanotechnology: Introduction and Significance

Nanotechnology was first introduced in the famous lecture of Nobel laureate Richard P. Feynman, “There’s Plenty of Room at the Bottom”, given in 1959 at California Institute of Technology<sup>1</sup>. Since then, there have been revolutionary developments in physics, chemistry and biology during past 25 years. These developments have proved Feynman’s ideas of manipulating and controlling matter at extremely small scale, even to the level of molecules and atoms, i.e. nanoscale<sup>2,3</sup>.

Literally, nanotechnology means any technology performed on a nanoscale that has applications in the real world. It deals with the production and application of physical, chemical and biological systems at scales ranging from a few nanometers to submicron dimensions, as well as integration of the resulting nanostructures into larger systems. According to Whatmore and Corbett<sup>3</sup>, the subject of nanotechnology includes almost any materials or devices which are structured on the nanometer scale in order to perform functions or obtain characteristics which could not be otherwise achieved.

When the dimensions of a material are decreased from macroscale to nanoscale, its properties such as electronic conductivity, optical absorption, chemical reactivity, mechanical properties etc. change significantly. With decrease in particle size, surface area of the material increases remarkably and more atoms are located on the surface of the particle. The surface area imparts a serious change of surface energy and surface

morphology. All these factors alter the basic properties and the chemical reactivity of the nanomaterials. The changes in the properties causes improved catalytic ability<sup>4</sup>, tunable wavelength-sensing ability<sup>5</sup>, better burning rate for propellants<sup>6</sup> and so on.

Although nanotechnology is now well-known, it still remains in its pre-exploration stage; it is just emerging from fundamental research to the industrial application. Further research in nanotechnology promises breakthroughs in materials and manufacturing, nanoelectronics, medicine and healthcare, energy, biotechnology and information technology. The discovery of novel materials, processes, and phenomena at the nanoscale, as well as the development of new experimental and theoretical techniques for research provide fresh opportunities for the development of innovative nanosystems and nanostructured materials. Nanosystems are expected to find various unique applications. Nanostructured materials can be made with unique nanostructures and properties. This field is expected to open new venues in science and technology.

## **1.2. Cerium Oxide: Background and Motivation**

Cerium is a rare earth element of the lanthanide series. Although a rare earth element, it is relatively abundant in the earth's crust. Among the lanthanides, it is the most abundant, and among the 78 common elements in the earth's crust, it ranks 25<sup>th</sup> in occurrence at an average distribution of 20 to 60 ppm<sup>7</sup>. After europium, cerium is the most reactive of the rare earth metals, easily oxidizing at room temperature. While most of the rare earths exist in trivalent state, cerium also occurs in +4 state and may flip-flop between the two in a redox reaction<sup>8-10</sup>. It is established that cerium oxides make excellent oxygen buffers, because of its redox capacity<sup>11</sup>. As a result of alterations in

cerium oxidation state, cerium oxide forms oxygen vacancies, or defects, in the lattice structure, by loss of oxygen and/or its electrons<sup>8,9</sup>. The valence and defect structure of cerium oxide is dynamic and may change spontaneously or in response to physical parameters such as temperature, presence of other ions, and oxygen partial pressure ( $pO_2$ )<sup>9,10,12</sup>.

The chemical behavior of cerium oxide nanoparticles may mirror the chemical properties of its bulk state to some extent, but altered characteristics are likely at the nanoscale. For example, Raman spectra of cerium oxide nanoparticles are very different from microparticles<sup>10</sup>. Additionally, at the nanoscale, the surface area of cerium oxide particles is dramatically increased. So greater oxygen exchange and redox reactions may occur<sup>13</sup>. During his master's thesis<sup>14</sup>, the author studied synthesis of uniformly distributed, non-agglomerated cerium oxide nanoparticles using microemulsion technique and used them as a coating material to prevent high temperature oxidation of AISI 304 stainless steel. It also mentioned some of the preliminary studies carried out on organotypic tissue culture model of rat brain cells. The original intent was to coat nanocerium with enzymes that might provide a cell surrogate, in the event of tissue damage. To examine this, the first initial experiment would obviously be to add the nanoparticles to cell cultures and investigate toxicity. *The results of these experiments were both striking and surprising, as described below.*

The published literature suggests that a major component of aging is free radical damage to cellular macromolecules. The preliminary experiments with cerium oxide nanoparticles were conducted in organotypic "mixed" brain cell cultures, which include

astrocytes, neurons, microglia, oligodendrocytes, and ciliated ependymal cells. Organotypic brain cell cultures cannot be maintained indefinitely ex vivo, and normally begin to die off after 23-30 days. However cultures treated with 10 nM cerium oxide nanoparticles survived an average of 82 days in vitro. The maximum life observed for these cultures was 123 days. Additionally, the nanoparticles protected the cell cultures from various free-radical induced injuries such as H<sub>2</sub>O<sub>2</sub> treatment, UV-radiation etc.

Based on the results, it was hypothesized that cerium oxide nanoparticles extend cellular longevity by scavenging free radicals generated during their lifespan. The unique structure of ceria nanoparticles, with respect to valence and oxygen defects, promotes cell longevity and decreases toxic insults by virtue of its antioxidant properties. The co-existence of both Ce<sup>3+</sup> and Ce<sup>4+</sup> oxidation states in CeO<sub>2</sub> nanoparticles play a critical role in its anti-oxidant behavior. It has been postulated that a transition in the oxidation state occurs in the biological environment; resulting in the therapeutic benefit of CeO<sub>2</sub> nanoparticles.

In view of the importance of nanoceria in various biological applications, the primary objective of this work is to understand the basic properties of cerium oxide nanoparticles and study its effect in various other free radical mediated applications in biotechnology.

### **1.3. Organization**

The work in this dissertation extends the author's master's thesis work at UCF. The primary focus of the master's thesis work was to synthesize uniformly distributed, non-agglomerated ceria nanoparticles and study their effect on improving high temperature

oxidation protection to AISI 304 steel. The present study focuses on the fundamental aspects of cerium oxide nanoparticles and their applications in nanobiotechnology.

The dissertation can be divided into two major parts namely, fundamental studies of cerium oxide nanoparticles and applications of the synthesized nanoceria in biotechnology. The fundamental study is categorized into size dependent changes in ceria properties and effect of doping with trivalent elements: La and Nd. Chapter 2 provides the basics of microemulsion process for nanoparticles synthesis and its use to synthesize cerium oxide nanoparticles. Also, it utilizes the same process to synthesize uniformly distributed ceria nanoparticles with varying doping amounts to change its defect chemistry. Chapter 3 elaborates on the variation in the properties of nanoceria as a function of particle size as well as doping concentration. Chapters 4 and 5 are based on the applications of synthesized nanoceria in biology. While chapter 4 is completely focused on development of a nanoceria based electrochemical biosensor for detection of hydrogen peroxide in biological systems, chapter 5 summarizes various biological applications of nanoceria to decrease reactive oxygen species (ROS) induced cellular damages *in vitro*, investigated in collaboration with different research groups specialized in their respective fields.

## **CHAPTER 2. SYNTHESIS OF CERIUM OXIDE NANOPARTICLES**

### **2.1. Introduction**

Production of nanoscale materials is one of the biggest challenges of science and technology today. Although the progress in this field has been very impressive in recent years, much has to be done in order to understand the properties of these systems and to achieve good control of the nanostructure of these materials.

Nanostructures are not new nor were they first created by man. There are many examples of nanostructures in nature in the way that plants and animals have evolved. Similarly, there are many natural nanoscale materials, catalysts, porous materials, certain minerals, soot particles etc. that have unique properties particularly because of the nanoscale features. What is new about nanotechnology is that we can now, at least partially, understand and control these structures and properties to make new functional materials and devices.

Approaches to nanotechnology research and development are grouped into two categories, “top down” and “bottom up”. “Top down” is an approach that downsizes things from large-scale structures into nanometer-scale structures. Here, small features are made by starting with larger materials and patterning and “carving down” to make nanoscale structure in precise patterns. Complex structures including microprocessors containing 100s of millions of precisely positioned nanostructures can be fabricated using micro- and nano-lithography and etching. Of all forms of nanotechnology, this is

the most well-established. The narrowest line pattern on a semiconductor device is now coming to the 50 nanometer level. This is an achievement of the top-down approach. In recent years, the same “top down” nanoprocessing techniques have enabled many non-electronic applications, including micromechanical, micro-optical, and micro-fluidic devices.

The “bottom-up” approach ingeniously controls the building of nanoscale structures. This approach shapes the vital functional structures by building atom by atom and molecule by molecule. Here we are using the forces of nature to assemble nanostructures – the term “self assembly” is often used. Here, the forces of chemistry are in control and we have, at least to date, somewhat less flexibility in making arbitrary structures. The nanomaterials created this way, however, have resulted in a number of consumer products. Significant advances are expected in the next decade in this area as we understand more completely the area of chemical nanotechnology.

Bottom-up construction process is one of the most promising directions for nanoparticles synthesis. When nanoparticles are created using the bottom-up approach, the size and the shape of a particle can be controlled by production conditions. Chemical synthesis – the spontaneous self-assembly of molecular clusters (molecular self-assembly) from simple reagents in solution – or biological molecules (e.g. DNA) are used as building blocks for the production of three dimensional nanostructures, including quantum dots (nanocrystals) of arbitrary diameter ( $\sim 10$  to  $10^5$  atoms).

## **2.2. Microemulsion Process for Nanoparticles Synthesis**

Several techniques have been developed for the synthesis of various types of nanoparticles. These include gas-phase techniques such as gas evaporation, laser vaporization and laser pyrolysis<sup>15-19</sup>; vacuum synthesis techniques like sputtering, laser ablation and ionic beam deposition<sup>20-23</sup>; and liquid phase techniques like precipitation from homogeneous solutions, sol-gel processing and freeze drying<sup>24-26</sup>. Precipitation reactions in microemulsions offer a novel and versatile technique for the synthesis of a wide variety of nanophase materials with the ability to control precisely the size and shape of the particles formed<sup>27-29</sup>.

Microemulsion is a special class of colloidal solutions with very small droplets of the dispersing phase stabilized by the surfactant molecules, spontaneously arranged as a monolayer between the two liquids, to give optically transparent solution. It is defined as an isotropic and thermodynamically stable single-phase system that consists of three components: water, oil, and an amphiphilic molecule, called surfactant<sup>30</sup>. The small droplets formed by the spontaneous arrangement of surfactant molecules at the water-oil interface are called micelles. These droplets may either consist of water or oil. When they consist of water, the emulsions are called water-in-oil (W/O) and oil-in-water (O/W) when they consist of oil.

### **2.2.1. Thermodynamics of Micelle Formation and Microemulsion**

The thermodynamic principles underlying micelle formation are conceptually simple: the hydrophobic effect of the surfactant tails provides the driving force for aggregation, whereas repulsion between hydrophilic head groups limits the size that a micelle can



attain. Both these factors vary with micelle size. The objective of a thermodynamic treatment is to relate the chemical potential of an amphiphile in the micellar state to the chemical potential of the free amphiphile in solution.

In general, the treatment of surface chemical behavior by means of thermodynamic equations suffers from lack of rigorous relationships between such equations and the molecular interactions taking place at an interface. Nevertheless in the past few years thermodynamic principles have been introduced into the study of microemulsion systems and have yielded some insight into their behavior.

Ruckenstein<sup>31</sup> modeled microemulsion as a dispersion of globules of oil (water) in a continuous medium (water (oil)) and the surfactant and co-surfactant distributed at equilibrium between the two media and their interface. Using this model he decomposed the Helmholtz free energy ( $f$ ) per unit volume of microemulsion as a sum of free energy  $f_0$  of dispersion of fixed, non-interacting globules in a continuous medium and free energy ( $\Delta f$ ) due to the entropy of dispersion and the interactions among the globules:

$$f = f_0 + \Delta f \quad (1)$$

This decomposition allows one to employ the Gibbs thermodynamics for  $f_0$  and the conventional statistical mechanics for  $\Delta f$ . Gibbs thermodynamics provides the expression for  $df_0$ :

$$df_0 = \gamma dA + C_1 dc_1 + C_2 dc_2 + \sum \mu_i dn_i - p_2 d\phi - p_1 d(1 - \phi) \quad (2)$$

where  $\gamma$  is the interfacial tension;  $C_1$  and  $C_2$  are the bending stresses associated with the curvatures  $c_1$  and  $c_2$ , respectively;  $A$  is the interfacial area per unit volume between the two media of the microemulsion;  $\mu_i$  and  $n_i$  are the chemical potential and the number of molecules of species  $i$  per unit volume, respectively; and  $\phi$  is the volume fraction of the dispersed phase which includes surfactant and co-surfactant molecules present at the interface of the globules. The chemical potentials were taken at pressure  $p_1$  for the species present in the continuous phase and at pressure  $p_2$  for those present in the dispersed phase. The more details of the thermodynamic treatment of microemulsion by Ruckenstein is discussed in the master's thesis of the author<sup>14</sup>.

### **2.2.2. Nanoparticles Synthesis**

Since the last decade, the water-in-oil (W/O) microemulsion technique has become very powerful tool to synthesize monodisperse nanoparticles of various kinds<sup>32-37</sup>, including magnetic nanoparticles<sup>34</sup>, semiconductor Q-dots<sup>36</sup>, dye-doped nanoparticles<sup>32,33,37</sup> etc. at room temperature. The water nanodroplets present in the bulk oil phase serve as nanoreactors for the synthesis of nanoparticles. Nanoparticles precursors (e.g. chemical reagents) undergo chemical reaction inside the nanoreactor to form nanoparticles, following atom-by-atom integration mechanism. The shape of the water pool is spherical which results in the formation of spherical nanoparticles. The size of the water pool greatly influences the size of the nanoparticles. Thus, the size of the spherical nanoparticles can be controlled and tuned by changing the size of the water pool ( $W_0$  value, the water-to-surfactant molar ratio). In general, the higher the value of  $W_0$ , the larger the particle size. The beauty of the W/O microemulsion technique is its versatility.

A variety of “tailor-made” nanoparticles such as core-shell, doped nanoparticles etc. can be synthesized. It is also possible to synthesize monodisperse nanoparticles as small as a couple of nanometers to a several hundreds of nanometers by controlling the synthesis parameters.

There are two ways to synthesize nanoparticles using the W/O microemulsion method. One way consists of mixing of microemulsions containing the reactants necessary for the preparation of desired particles. The schematic picture of this method is given in Figure 2.1. Care should be taken in using identical microemulsion systems for each reactant (precursor and precipitating agent) in order to avoid the complexities. The reaction takes place when the micelles containing the reacting species come into contact with each other either by collision or by coalescence. The precipitate particle is confined to the interior of the microemulsion droplets. This is the main principle utilized in the nanoparticle synthesis. When the chemical reaction rate is fast, the overall rate of the formation of the particles is controlled by the rate of coalescence of the microemulsion droplets containing the reactants. The interfacial rigidity plays an important role in such cases. A relatively rigid interface decreases the rate of coalescence leading to slower rate of reaction while a less rigid interface in the microemulsion enhances it. The structure of oil, surfactant, co-surfactant and the ionic strength of the aqueous phase affect the interface rigidity<sup>38,39</sup> and one can control the kinetics of the reaction by controlling the rigidity of the interface. Figure 2.1 shows the formation of nanoparticles by using two microemulsions, microemulsion A containing the precursor and the microemulsion B containing the precipitating or reducing agent. The exchange of the reactants takes place after collision of the droplets and nuclei are

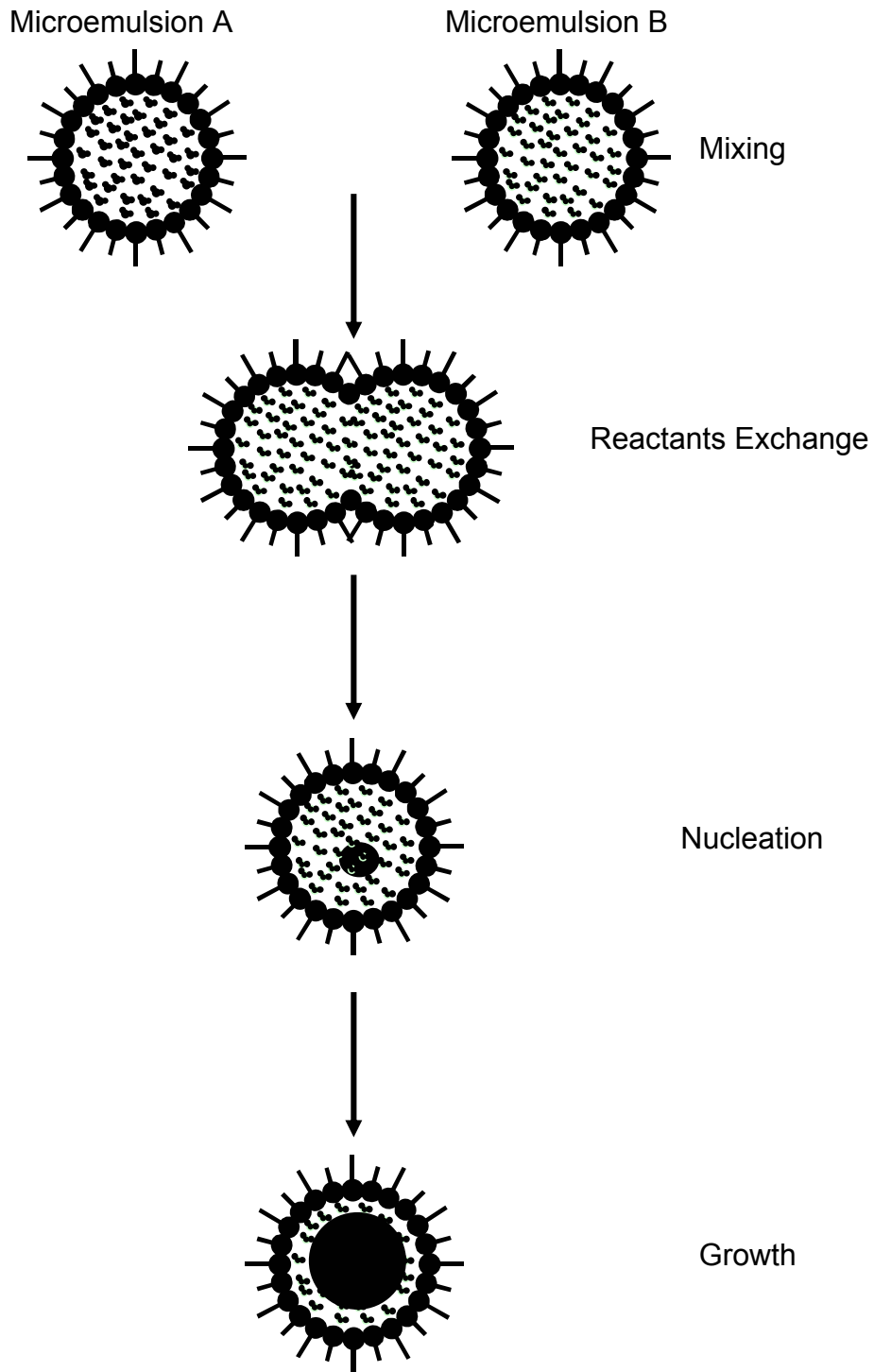


Figure 2.1. Mechanism of synthesis of nanoparticles using mixing of microemulsions

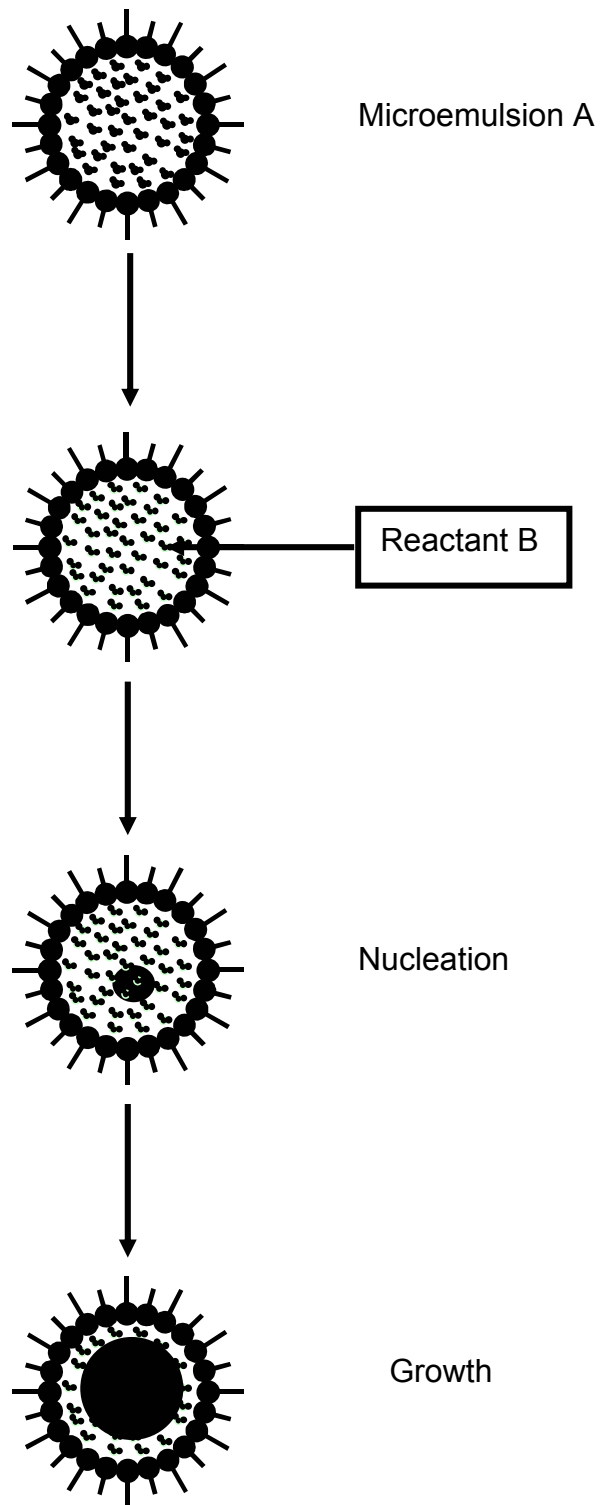


Figure 2.2. Mechanism of synthesis of nanoparticles using single microemulsion

simple, in reality the situation is quite complex because of the influence of various factors like viscosity, interface rigidity, mobility of the droplets etc. Several kinetic models have been proposed in order to explain the particle formation process in microemulsion systems<sup>40-43</sup>.

The nanoparticles can also be synthesized in a microemulsion by adding a precipitating or reducing agent in the form of a liquid or a gas to the microemulsion containing the primary reactant dissolved in its aqueous core. The chances of particle growth in this system due to collision of microemulsion droplets are minimized because of the increased interface stability. Initially, the precipitation or reducing agent will be accessible to the water core of the microemulsion due to the percolation. Subsequently, nuclei of the precipitate are formed inside the water core, which eventually grow till the precipitation or reduction reaction is almost completed inside the microemulsion droplet. Therefore, the size of the grown particle will be limited by the size of the water droplet that acts as the nanoreactor in such cases. Many times, the diameter of the particle formed inside the water droplet is almost equal to the size of the water droplet itself. The reaction scheme is shown in Figure 2.2. Such percolation of the precipitating or reducing agent has been reported for synthesis of various metal-boride and metal-oxide nanoparticles<sup>44,45</sup>.

Nanoparticles synthesis using the microemulsion technique offers different advantages over other techniques. It does not require extreme temperature or pressure conditions; it can be used, in principle, with almost all chemical reactions that have been developed to obtain particles in homogeneous solutions; and it does not require special equipment.

But still it is limited as a laboratory technique and different schemes have been proposed to extend this technique to industrial scales.

### **2.3. Cerium Oxide Synthesis using the Microemulsion Process**

Cerium oxide nanoparticles have been prepared by hydrothermal<sup>46</sup> and sol-gel<sup>47</sup> methods. The sol-gel method is useful in coating complex geometry and large sizes. However, a major problem associated with preparation of nanoparticles is agglomeration. The beneficial effect of the nanosized particles is usually lost by agglomeration. Therefore, synthesis of non-agglomerated nanocrystalline cerium oxide particles is of critical importance. The present study utilizes the water in oil (W/O) microemulsion method to produce spherical cerium oxide nanoparticles with a controlled particle size.

When water is added to a solution of a non-polar solvent (hydrocarbon) and surfactant, the surfactant molecules get coordinated to form reverse micelles (surfactant heads forming the interior of the micelle) confining the water molecules. The reverse micelles formed this way have been advantageously used for the synthesis of nanoparticles. Sodium bis(2-ethylhexyl) sulfosuccinate (AOT) is a popular surfactant in reverse micelle applications because of its ability to solubilize relatively large amounts of water in a variety of hydrophobic organic solvents and to form thermodynamically stable reverse micelles and microemulsions<sup>48</sup>. A typical phase diagram of water/AOT/isooctane system (Figure 2.3) determined using the experimental method by Tamamushi and Watanabe<sup>49</sup> shows the large W/O region, which is useful for nanoparticles synthesis.

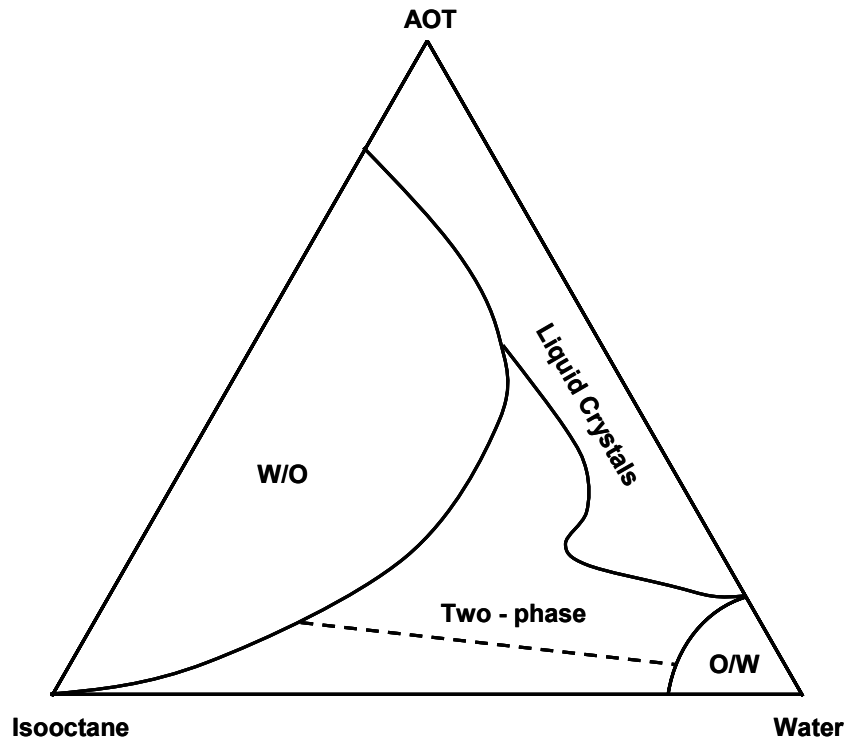


**Figure 2.3.** Ternary phase diagram of water/AOT/isooctane system determined using experimental method<sup>49</sup>

AOT is an anionic surfactant with two hydrocarbon chains and does not require co-surfactant to enable to form microemulsion<sup>50</sup>. Therefore, it has been widely used for the synthesis of nanoparticles of various metals as well as oxides<sup>44,51-54</sup>. The microemulsion system consisting of toluene or isooctane as oil and AOT as surfactant was utilized in the present study for the synthesis of cerium oxide nanoparticles. The study was divided into two major objectives namely, particle size variation and doping of nanoparticles with no particle size variation. The details of the experiments and the results are discussed in the following sections.



### 2.3.1. Cerium Oxide Nanoparticles Synthesis

As mentioned earlier, the use of reverse micelles as nanoreactors for synthesis of nanoparticles is very promising. Reverse micelles consist of aqueous droplets of small size that are separated from the bulk organic phase by a monolayer of surfactant. The water pool diameter is believed to govern the size of the reverse micelle, characterized by the molar ratio ( $W_0$ ), of water to surfactant ( $[\text{H}_2\text{O}]/[\text{AOT}]$ ). As the nanoparticles are formed in the interiors of the reverse micelle, the particle size is controlled by the size of the reverse micelle, which is directly proportional to  $W_0$ <sup>55,56</sup>.

All the chemicals were obtained from Aldrich Chemicals Company Inc. and used without further purification. 0.5 gm AOT was dissolved in toluene to obtain an AOT/toluene stock solution. A 2.5ml of 0.1M aqueous cerium nitrate solution was added dropwise to the AOT/toluene solution under magnetic stirring. 5ml of 1.5M hydrogen peroxide was then added to the reverse micellar solution to obtain the cerium oxide nanoparticles. The solution was kept standstill after completion of reaction to obtain a stable yellow sol containing cerium oxide nanoparticles as a top layer. Excess water phase at the bottom was removed.

As mentioned before, the diameter of the water pool is believed to control the final nanoparticle size. This diameter can be estimated by measuring the reverse micelle hydrodynamic diameter and subtracting the thickness of the surfactant layer, which is about 1.2 nm for AOT<sup>57</sup>. Dynamic light scattering (DLS) was used to measure the hydrodynamic diameter of the micelles using Zetasizer Nano ZS particle size analyzer from Malvern Instruments Ltd. Figure 2.4 shows the micelle size distribution curve for

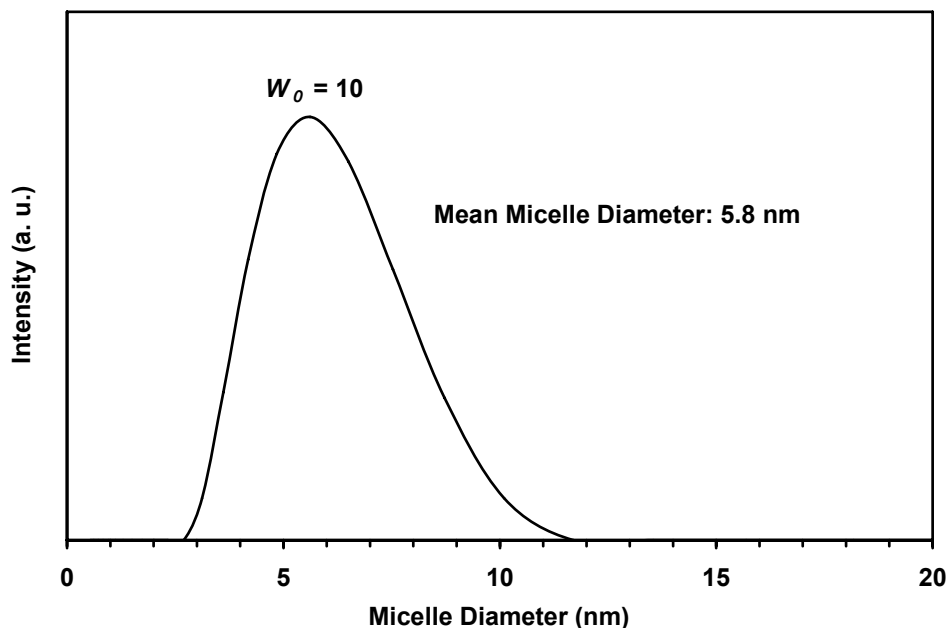


**Figure 2.4. Micelle size distribution curve for the synthesized cerium oxide nanoparticles containing sol measured using particle size analyzer**

the synthesized cerium oxide nanoparticles containing microemulsion sol. The mean hydrodynamic diameter of the micelles was found to be 5.8 nm for this micellar system giving the cerium oxide nanoparticles size of about 3.4 nm.

The cerium oxide nanoparticles were precipitated from the micellar solution by addition of excess amount of ammonium hydroxide. The nanoparticles precipitate was then washed several times with acetone and water and the obtained powder was then dried at 400°C for 2hrs. To study the size dependent properties in cerium oxide, the nanoparticles powder was also heated at 600°C to grow the particles to larger sizes.

The shape and size of the synthesized cerium oxide nanoparticles was determined using a Philips (Tecnai series) High Resolution Transmission Electron Microscope

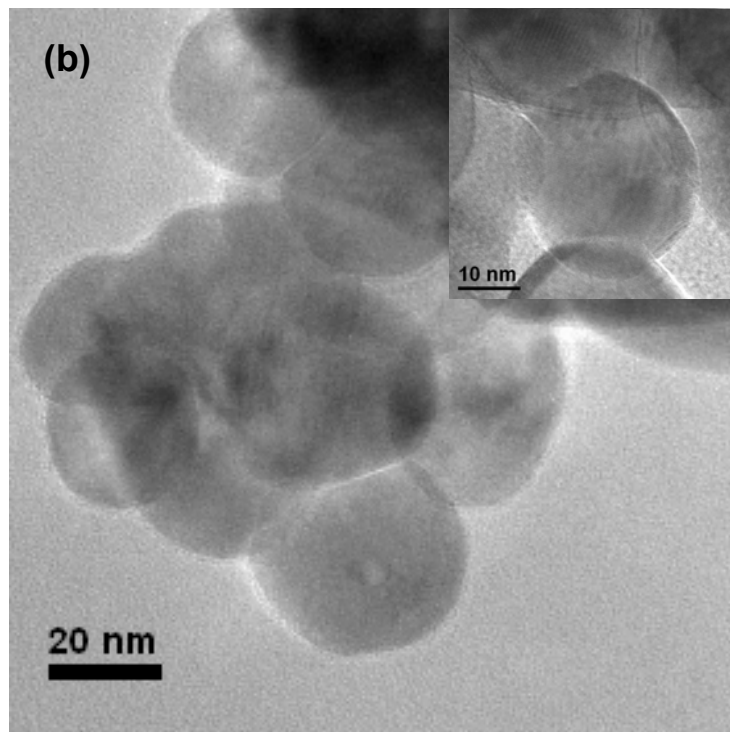
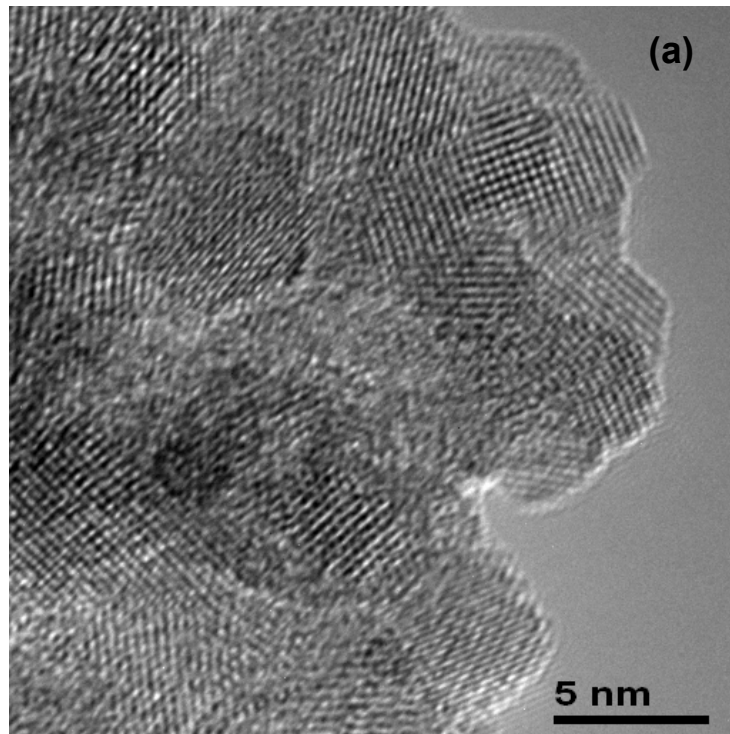


Figure 2.5. HRTEM images of the synthesized cerium oxide nanoparticles with particle size of (a) 3-5 nm and (b) 25-30 nm

(HRTEM) operated at an accelerating voltage of 300 keV. The nanopowder was dispersed in acetone by ultrasonication. The TEM sample was then prepared by dipping a carbon-coated copper grid in the nanoparticles dispersion and subsequently drying it at room temperature under vacuum. Figure 2.5 gives the HRTEM images of the synthesized cerium oxide nanoparticles. The as-synthesized nanoparticles were 3-5 nm in size with near-spherical morphology. The formation of such nanosized particles was highly expected. AOT reverse micelles act as nanoreactors to facilitate the formation of nanoparticles in a controlled manner. The nanoparticles obtained by heating the nanopowder of cerium oxide also had a near-spherical morphology with particle size in the range of 25-30 nm.

### **2.3.2. Doping of Cerium Oxide Nanoparticles with Trivalent Elements**

Recently, a lot of interest has been generated in cerium oxide nanoparticles for various catalytic applications due to its ability to easily absorb and release oxygen<sup>58</sup>. The ability to store oxygen is a result of cerium's ability to change valence states and the presence of intrinsic O vacancies in the CeO<sub>2</sub> lattice. The addition of trivalent elements in the CeO<sub>2</sub> crystal lattice also causes the formation of O vacancies by replacing one Ce<sup>4+</sup> ion for every two trivalent ions in the CeO<sub>2</sub> lattice. These vacancies increase O diffusion and thereby increase the ease with which the material can absorb and release O.

Although, several doped-CeO<sub>2</sub> systems have been investigated, the doping effect in cerium oxide nanoparticles with well characterized particle size has not been studied. The doping of ceria at that small size can be very beneficial to further improve its catalytic properties. Therefore, the doping effect of mono-disperse cerium oxide

nanoparticles with varying amounts of La and Nd for controlled particle size of 3-5nm was studied.

The same microemulsion system (used to synthesize cerium oxide nanoparticles) consisting of AOT, toluene and water was utilized for synthesizing the doped nanoparticles. Cerium nitrate, lanthanum nitrate and neodymium nitrate were used as the precursors while ammonium hydroxide was used as a co-precipitating agent. All the chemicals were obtained from Aldrich Chemicals Company Inc. and used without further purification. The precursors were mixed with different  $N_{RE}/N_{Ce}$  atomic ratios, where RE = La or Nd. The dopant (La or Nd) percentage was determined by the formula:

$$\text{atomic \% dopant} = (100 \cdot N_{RE}) / (N_{Ce} + N_{RE}) \quad (3)$$

The details of the samples are given in Table 2.1. The synthesis process was the same as that explained in section 2.3.1. Figure 2.6 shows the bright field HRTEM micrographs of all the doped samples exhibiting near-spherical 3-5nm particles with a uniform particle size distribution. The same particle size for all the samples was expected as  $W_0$  was kept constant for all samples synthesis. The selected area diffraction patterns shown in the inset of the micrographs indicate the fluorite crystal structure for all the doped nanoceria samples.

**Table 2.1. Details of the samples doped with La and Nd**

Sample	Atomic ratio of dopants used for synthesis		Dopant amount (atom %)
	$N_{La}/N_{Ce}$	$N_{Nd}/N_{Ce}$	
CeO <sub>2</sub> – 0	-	-	0
CeO <sub>2</sub> – 1	5/100	-	4.76
CeO <sub>2</sub> – 2	10/100	-	9.09
CeO <sub>2</sub> – 3	20/100	-	16.67
CeO <sub>2</sub> – 4	-	5/100	4.76
CeO <sub>2</sub> – 5	-	10/100	9.09
CeO <sub>2</sub> – 6	-	20/100	16.67

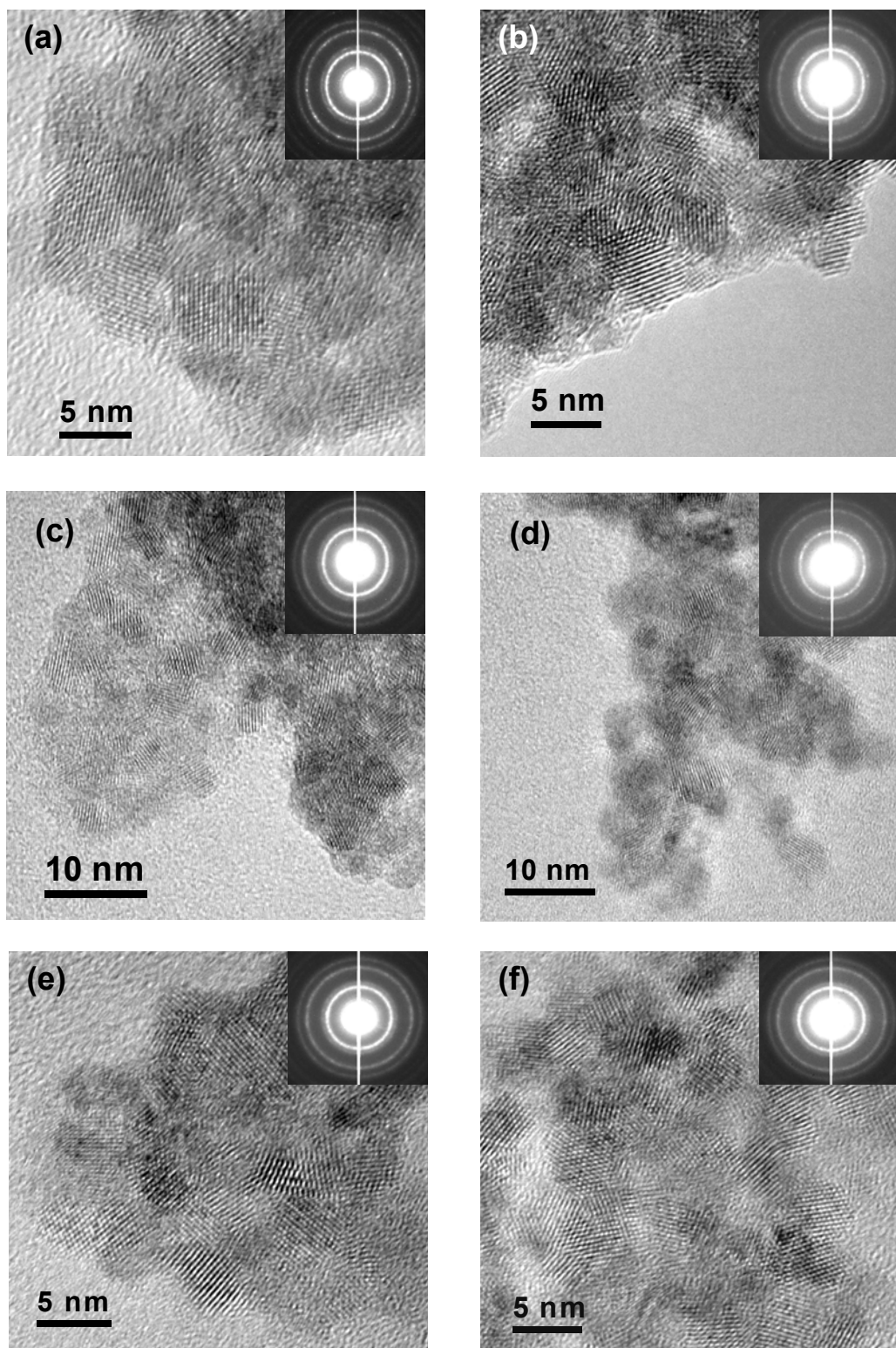


Figure 2.6. HRTEM images of doped nanoceria samples. (a) CeO<sub>2</sub> - 1, (b) CeO<sub>2</sub> - 2, (c) CeO<sub>2</sub> - 3, (d) CeO<sub>2</sub> - 4, (e) CeO<sub>2</sub> - 5, and (f) CeO<sub>2</sub> - 6

## CHAPTER 3. PROPERTIES OF CERIUM OXIDE NANOPARTICLES

### 3.1. Introduction

Nanostructured materials have attracted much attention due to their reported unique structure and physical properties attributed to the grain boundary and grain-size dependent non-stoichiometry<sup>59,60</sup>. Structural and physical properties of metal clusters and semiconducting nanoparticles prepared in many ways have been studied widely<sup>17,61-63</sup>. A number of studies have shown that materials with grain sizes less than 100 nm exhibit optical, electrical, catalytic and mechanical properties that are different from those observed for conventional microcrystalline specimens<sup>4,59</sup>. But structural and physical properties of oxide nanoparticles less than 10nm are rarely investigated, because of the difficulties in controlling monodisperse particle size distribution at that range. The ability to enhance the properties by controlling the particle size may lead to potentially useful technological applications of nanocrystalline oxides in gas sensors, fuel cells, ionic membranes and many more new applications.

Cerium oxide is an important technological ceramic whose electrical properties are strongly related to the microstructure such that an enhancement of about four orders of magnitude in electronic conductivity was observed when the changed microstructure changed from the micro- to nanocrystalline region<sup>64</sup>. This effect was probably attributed to extended interfacial area and reduced enthalpy for defect formation. Recent work has



shown that cerium oxide films with ultrafine grain size can greatly improve the resistance of metals and alloys to high temperature oxidation<sup>65,66</sup>.

Since the physical properties of nanocrystalline cerium oxide are different than that of bulk or microcrystalline cerium oxide, it is very important to study the variation in these properties in nanoparticle range. This can lead to optimization of the properties obtained from nanocerium for specific applications. In this chapter, the studies related to the fundamental properties of nanocrystalline cerium oxide are presented. The objective was to analyze the properties such as lattice parameter and defects concentration of the cerium oxide nanoparticles as a function of their particle size and dopant concentration (at a constant particle size). The analysis was carried out using X-ray diffraction (XRD) and Raman spectroscopy.

### **3.2. Size Dependent Variation in Properties of Cerium Oxide Nanoparticles**

The study was aimed to determine the effect of the particle size of cerium oxide nanoparticles on the lattice parameter and the defect chemistry. Nanocrystalline cerium oxide particles of varying size were synthesized using the W/O microemulsion technique as discussed in 2.3.1.

#### **3.2.1. X-ray Diffraction Studies**

The crystal structure was determined with XRD (Rigaku model) using Cu K<sub>α1</sub> radiation. The data were recorded at a scan rate of 0.2 degree/min. The XRD patterns of both, 3-5 nm and 25-30 nm ceria, along with microceria (obtained from Johnson Matthey) are shown in Figure 3.1. The peaks can be indexed to the fluorite structure of cerium oxide.

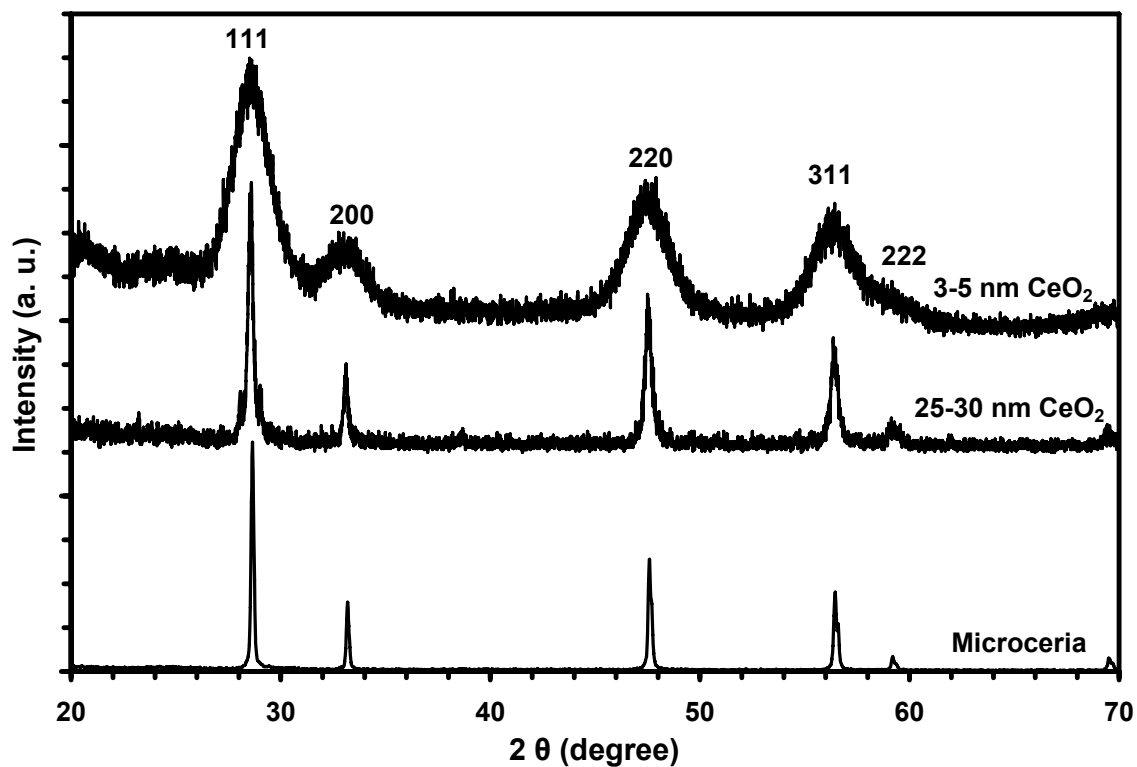


Figure 3.1. XRD plots of ceria nanoparticles with varying particle size

This is in line with the results obtained by HRTEM analysis. The d-spacing of the different planes was calculated using the Bragg's equation:

$$n\lambda = 2d\sin\theta \quad (4)$$

where  $\lambda$  is wavelength of X-rays ( $\text{Cu-K}\alpha_1 = 1.54056\text{nm}$ ),  $\theta$  is the diffraction angle and  $n = 1$ . The lattice parameter,  $a$ , was further calculated using the relation between  $d$  and  $a$  as:

$$a = d / (h^2+k^2+l^2)^{1/2} \quad (5)$$

**Table 3.1. Summary of size dependent changes in the properties of cerium oxide samples**

<b>Cerium Oxide Sample</b>	<b>Lattice Parameter (nm)</b>	<b>Raman Shift (cm<sup>-1</sup>)</b>	<b>Correlation Length, L (Å)</b>	<b>Defect Concentration, N (cm<sup>-3</sup>)</b>
Microceria	0.5412	464.40	100	2.38 x 10 <sup>17</sup>
25 – 30 nm	0.5417	456.75	19	3.48 x 10 <sup>19</sup>
3 – 5 nm	0.5429	458.03	11.5	1.57 x 10 <sup>20</sup>

The lattice parameter increased from 0.5410 nm for microceria to 0.5429 for the 3-5 nm cerium oxide nanoparticles. This indicates the size dependent lattice expansion for cerium oxide nanoparticles. Table 2.1 gives the lattice parameter, *a*, of microceria and the synthesized cerium oxide nanoparticles.

### **3.2.2. Raman Spectroscopic Analysis**

Raman scattering is an excellent, non-destructive and rapid analysis technique for investigating the electronic and phonon structure of materials. The different symmetries involved govern whether vibrations are Raman active and appear in the spectra, whilst changes in lattice spacing and chemical environment shift band frequencies.

Cerium oxide has a cubic fluorite type structure and belongs to the  $O_h^5$  (*Fm3m*) space group. This structure has six optical-phonon branches, which yield three zone-center frequencies. These frequencies are 272, 465 and 595 cm<sup>-1</sup>, corresponding to the doubly degenerated TO mode, the triply degenerate Raman-active mode and the nondegenerate LO mode, respectively. The triply degenerate Raman-active mode

frequency can be directly detected by Raman measurements, whereas the TO and LO frequencies are given indirectly by fits to infrared reflectivity<sup>67</sup>.

Raman spectroscopy is an effective method for studying material structure, so it is beneficial to use it to explore the surface layer structure of nanometer-sized crystals of CeO<sub>2</sub>, and to look for correlation between the change of the Raman spectrum of nanometer CeO<sub>2</sub> and its crystal size. Up till now, many temperature dependence measurements of the linewidths and frequency of the normal vibration of a crystal lattice have been carried out for crystals with various structures<sup>67-69</sup>. However, few experimental results dealing with correlation between the changes of the Raman spectrum of nanometer CeO<sub>2</sub> as a function of its particle size have been obtained. This study focuses on the change of the Raman spectrum with crystallite sizes of nanometer CeO<sub>2</sub>.

Raman spectra for the synthesized samples along with microceria were measured using a Horiba Jobin Yvon LabRam IR micro-Raman system with a spatial resolution of 2 micron. A helium-neon laser provided excitation at 633nm with a power of 3mW. The Raman scattered light was collected by a 50x objective in a back-scattering geometry and dispersed with a single stage 800mm spectrograph equipped with a CCD detector. A 1200 grooves/mm grating and a pinhole size of 100 microns resulted in a spectral resolution of 2 cm<sup>-1</sup>. A combination of Holographic notch and edge filters was used for Rayleigh line rejection.

Figure 3.2 shows the measured Raman spectra for the nanoceria samples along with the spectra for microceria. The influence of the particle size of CeO<sub>2</sub> on the shape of the

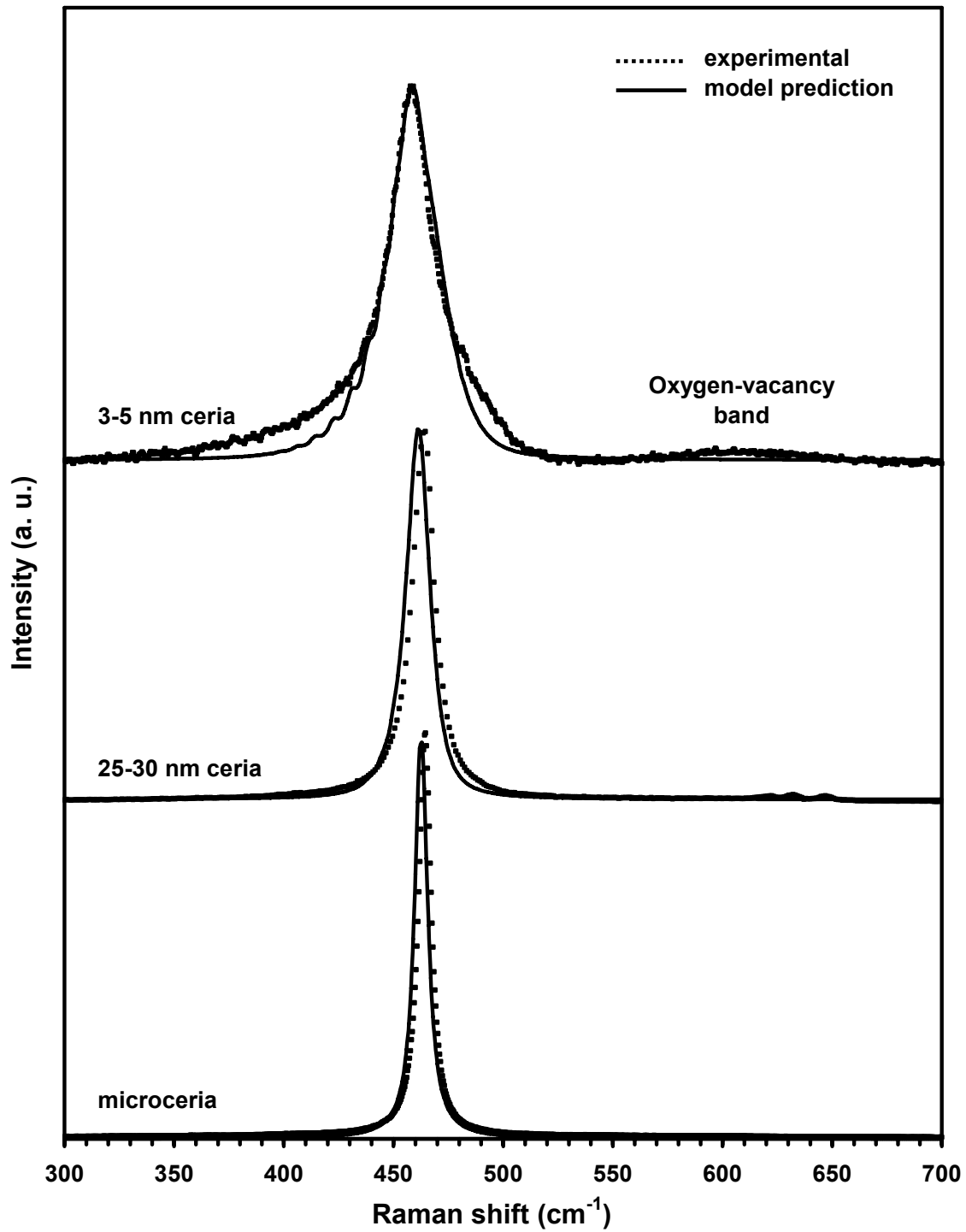


Figure 3.2. Raman spectra of ceria nanoparticles for different particle sizes obtained experimentally (dotted line) and also from the curve fit according to the spatial correlation model (solid line)

Raman spectrum was observed by a broadening of the line and an increase in its asymmetry which is attributed to reduction of the phonon lifetime in the nanocrystalline regime<sup>67,70-72</sup>. The peak frequencies for the single Raman line were determined by fitting the data to a Lorentzian line shape using PeakFit (Version 4.0) software. Table 3.1 gives the Raman allowed mode frequency shifts measured for all the samples. A larger peak shift (to lower energies) for smaller particle size indicates more lattice distortion in the nanoparticles. The increasing lattice constant with decreasing particle size as measured by XRD explains the Raman shift well.

In bulk, defect free crystalline materials,  $q = 0$  phonons can be Raman active and observed. As the dimension and size of a material is reduced, an increasing volume of reciprocal space is sampled in Raman scattering. Several factors can contribute to the changes in Raman peak position and linewidth of  $464 \text{ cm}^{-1}$  peak with nanoparticle size. These include phonon confinement, strain, broadening associated with the size distribution, defects and variations in phonon relaxation with particle size<sup>73</sup>.

Important information regarding the lattice disorder can be obtained from the analysis of the shape of the Raman line, which has been studied using the spatial correlation model<sup>74,75</sup>. According to this model, the Raman line intensity,  $I(\omega)$  at frequency  $\omega$  can be written as:

$$I = \int_0^l \exp\left(\frac{-q^2 L^2}{4}\right) \frac{d^3 q}{[\omega - \omega(q)]^2 + \left(\frac{\Gamma_0}{2}\right)} \quad (6)$$

where  $q$  is the wave vector expressed in units of  $2\pi/a$  ( $a$  is the lattice constant).  $\Gamma_0$  is the FWHM of Raman line of large grain sized material ( $6.9 \text{ cm}^{-1}$  observed for microceria sample). The expression  $\exp(-q^2L^2/4)$  represents a Gaussian spatial correlation function with parameter  $L$  as correlation length and  $w(q)$  is the function of Raman phonon dispersion.

For dispersion  $w(q)$ , we fitted the phonon dispersion determined from rigid-ion model<sup>67</sup> with analytical model relations:

$$[w(q)]_1 = 506 - 44.105 \cos(\pi q) \quad (7)$$

$$[w(q)]_2 = 462.5 - 175 q^2 \quad (8)$$

$$[w(q)]_3 = 377.1 + 86.58 \cos(\pi q) \quad (9)$$

Figure 3.3 shows the experimental data reported in reference<sup>67</sup> and our fitting results which were obtained with the equations (7) to (9) given above. The fitted data are in good agreement with the experimental data.

As the triple degeneracy of the Raman mode at  $464 \text{ cm}^{-1}$  is removed away from  $q = 0$ , equation (6) was summed over three equally weighted branches of the phonon dispersion given by equations (7), (8) and (9).

The Raman spectra line-shape fit was performed using the spatial correlation model explained above with only correlation length,  $L$  as a fitting parameter. The correlation length was found to be 10nm for microceria and it decreased to 1.9 nm and 1.15nm (less than 2 lattice constants) for the 25-30nm and 3-5 nm nanoceria samples

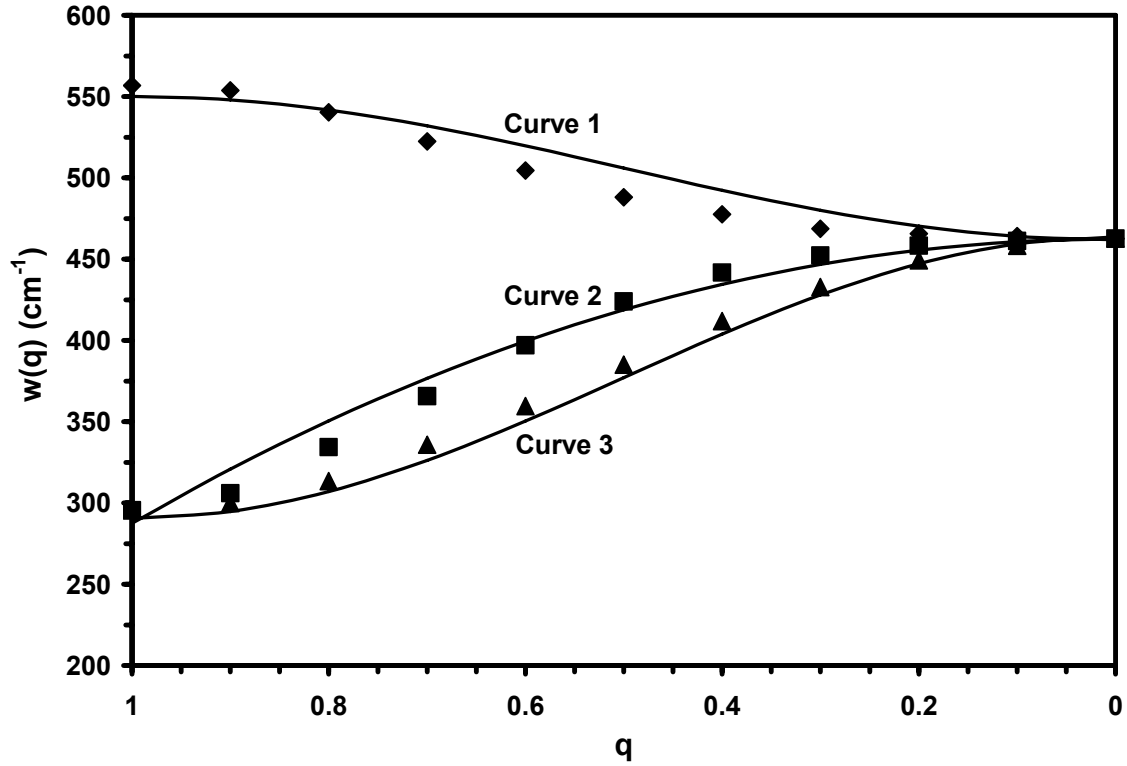


Figure 3.3. Phonon dispersion curves for cerium oxide obtained using a rigid ion model from reference <sup>67</sup> (dotted lines) and the fitted data (solid lines)

respectively. The Raman spectra obtained with curve fitting according to the spatial correlation model are also given in Figure 3.2.

The correlation length,  $L$  corresponds to the spheres with diameters equal to the distance between two next oxygen vacancies and can be used to determine the defect concentration,  $N$  as<sup>75</sup>:

$$N = \frac{3}{4\pi L^3} \quad (10)$$

The particle size effect increased the defect concentration by approx. 3 orders of magnitude from  $10^{17} \text{ cm}^{-3}$  for microceria to  $10^{20} \text{ cm}^{-3}$  for nanoceria. Table 3.1 gives the



defect concentration and the corresponding correlation length for the cerium oxide samples studied. The oxygen vacancies concentration studied from the electrical conductivity measurements has been given as<sup>75</sup>:

$$[V_{O^{\cdot\cdot}}] = N_0 \exp\left(\frac{-\Delta H}{3kT}\right) \quad (11)$$

where  $N_0 = 4.99 \times 10^{22} \text{ cm}^{-3}$  is the concentration of oxygen atoms in the  $\text{CeO}_2$  lattice and  $\Delta H$  denotes the changes in the enthalpy of oxygen vacancy formation. It was determined that  $\Delta H$  changes with the grain size of cerium oxide nanoparticles<sup>75</sup> making the oxygen vacancies formation more favorable at smaller size.

Additionally, there is a broad band in the range of  $540\text{-}640 \text{ cm}^{-1}$  for 3-5 nm cerium oxide nanoparticles. McBride *et al.*<sup>76</sup> used a model based on Green's function to attribute this feature to oxygen vacancies. This also confirms high oxygen vacancies in 3-5 nm ceria.

### 3.3. Effect of Doping with Trivalent Elements

Doping of cerium oxide with trivalent elements induces formation of oxygen vacancies in the  $\text{CeO}_2$  lattice. As seen in 3.2, cerium oxide shows size dependent changes in its properties. The particle size effect induces lattice expansion and the Raman spectroscopic studies indicate the increase in the oxygen vacancies as the particle size of cerium oxide nanoparticles decreases. Based on this background, the objective of this study was to increase the oxygen vacancies concentration in cerium oxide nanoparticles further by doping the nanoparticles with trivalent elements. As La and Nd give highest lattice expansion in ceria for a large doping concentration range<sup>76</sup>, they

were selected as dopants for ceria nanoparticles synthesized using the microemulsion technique. As discussed in 2.3.2, we were able to synthesize doped ceria nanoparticles of the same particle size of 3-5 nm for different doping concentrations using the microemulsion process. The synthesized nanoparticles were used for further analysis for changes in lattice parameter and defects concentration, studied using XRD and Raman spectroscopy.

### 3.3.1. X-ray Diffraction Studies

The XRD patterns of all the samples along with nanoceria are shown in Figure 3.4 (a). The broadened peaks in all the diffractograms confirm the nanocrystalline nature of the synthesized powder samples and the peaks can be indexed to the fluorite structure of cerium oxide. The absence of the additional peaks related to  $\text{La}_2\text{O}_3$  or  $\text{Nd}_2\text{O}_3$  in La-doped and Nd-doped ceria samples respectively, indicate the formation of a single phase  $\text{Ce}_{1-x}\text{RE}_x\text{O}_{2-y}$  type solid solution for the full doping range.

The lattice constant for all the samples was measured by fitting the peaks using PeakFit (Version 4.0) software. Figure 3.4 (b) shows the increase in the lattice constant with the dopant concentration. This means that doping affects the crystal structure of nanoceria. The lattice constant shifts shown in Figure 3.4 (b) can be directly correlated with the ionic size of the dopants; the larger or smaller dopants will dilate or contract the lattice, respectively, with the amount of change in lattice constant being approximately proportional to the ionic size. As the ionic radius of  $\text{La}^{3+}$  (0.122 nm) is larger than that of  $\text{Nd}^{3+}$  (0.115 nm), the lattice constant is larger for all the La-doped samples ( $\text{CeO}_{2-1}$  to  $\text{CeO}_{2-3}$ ) compared to the corresponding Nd-doped samples ( $\text{CeO}_{2-4}$  to  $\text{CeO}_{2-6}$ ). The

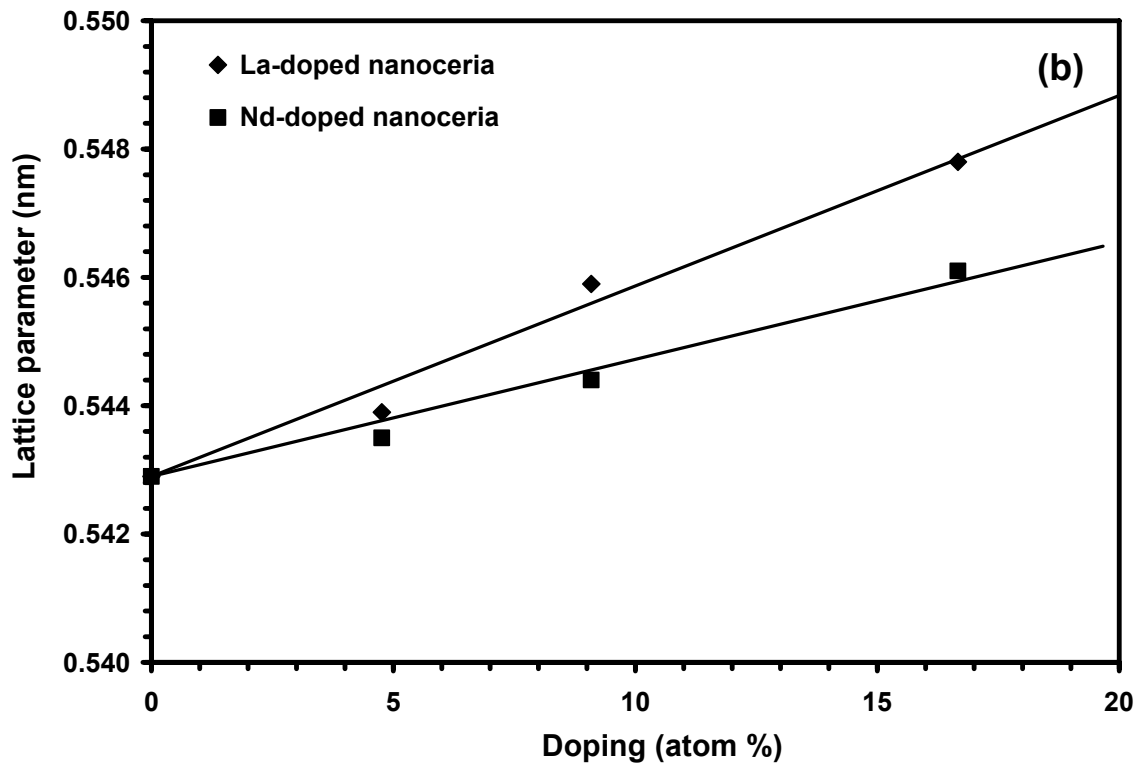
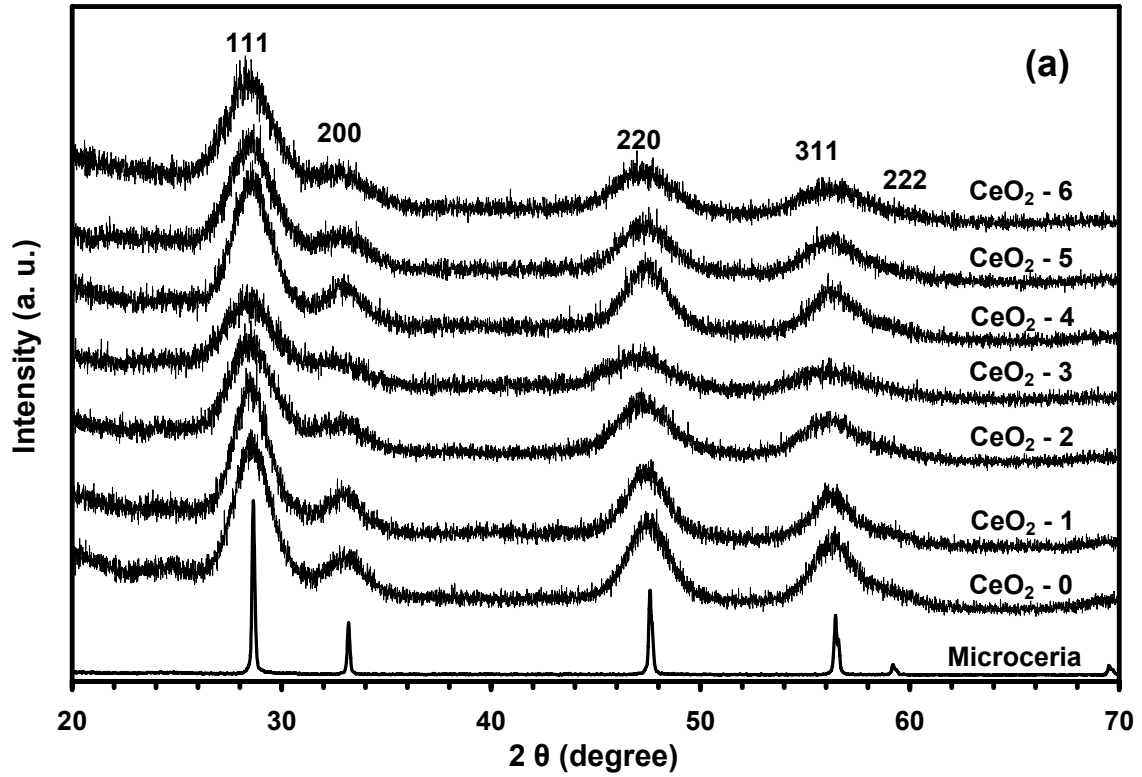


Figure 3.4. (a) XRD spectra of all the doped nanoceria samples. (b) Lattice parameter variation of the nanoceria samples as a function of doping amount

data obtained in Figure 3.4 (b) can be fitted by a straight line showing a linear trend in lattice expansion with the doping concentration. The slopes of the lines can be found to be 0.0297 and 0.0182 nm/atomic fraction for La and Nd doping respectively.

### 3.3.2. Raman Spectroscopic Analysis

$\text{RE}^{3+}$  in the  $\text{CeO}_2$  lattice deforms the structure and can be detected by Raman analysis. Figure 3.5 (a) and (b) show the measured Raman spectra for the La- and Nd-doped nanoceria samples, respectively, along with the spectra for nanoceria. The peak frequencies for the single Raman line were determined by fitting the data to a Lorentzian line shape using PeakFit (Version 4.0) software. Figure 3.5 (c) shows the Raman-allowed mode frequency shifts measured for all the samples. More peak shift (to lower energies) for the La-doped samples compared to Nd-doped samples indicates more lattice distortion in case of La-doped samples. This Raman shift can be explained by increasing the lattice constant with doping amount as measured using XRD.

With increasing dopant concentration the lineshape of the Raman-allowed mode gets progressively broader and asymmetric. The lattice disorder induced by the substitution of  $\text{RE}^{3+}$  ions causes this shape change in the Raman line. The Raman spectra lineshape fit was performed using the spatial correlation model explained in 3.2.2 with only correlation length,  $L$  as a fitting parameter. The correlation length was found to be decreasing gradually from 1.15nm for pure nanoceria to 0.86nm and 0.90nm for 16.67 atom% La-doped and Nd-doped samples respectively. The Raman spectra obtained with curve fitting according to the spatial correlation model are also given in Figure 3.5 (a) and (b) respectively for the La- and Nd-doped cerium oxide nanoparticles. Figure 3.6

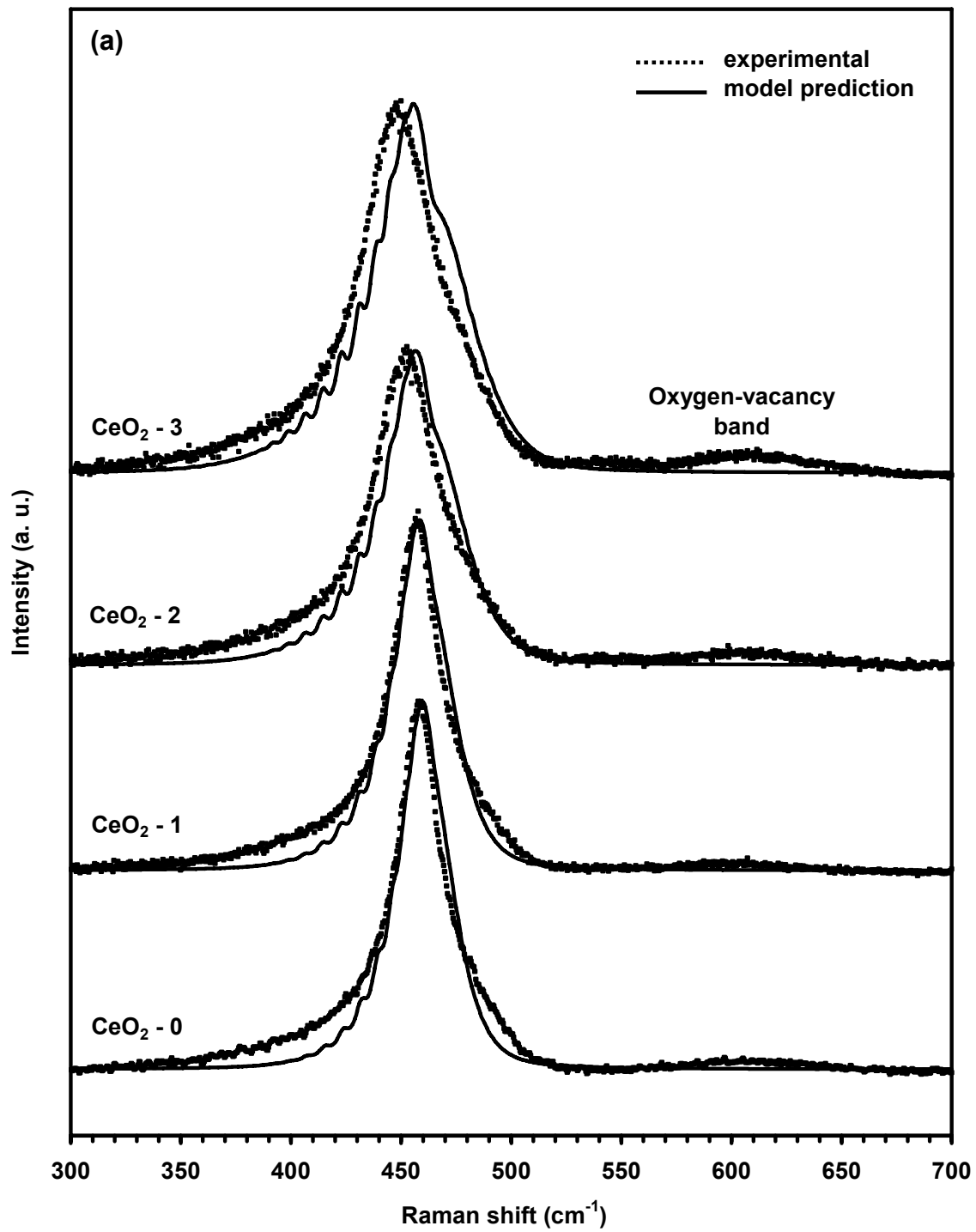
(a) shows the determined correlation length for doped nanoceria as a function of doping concentration.

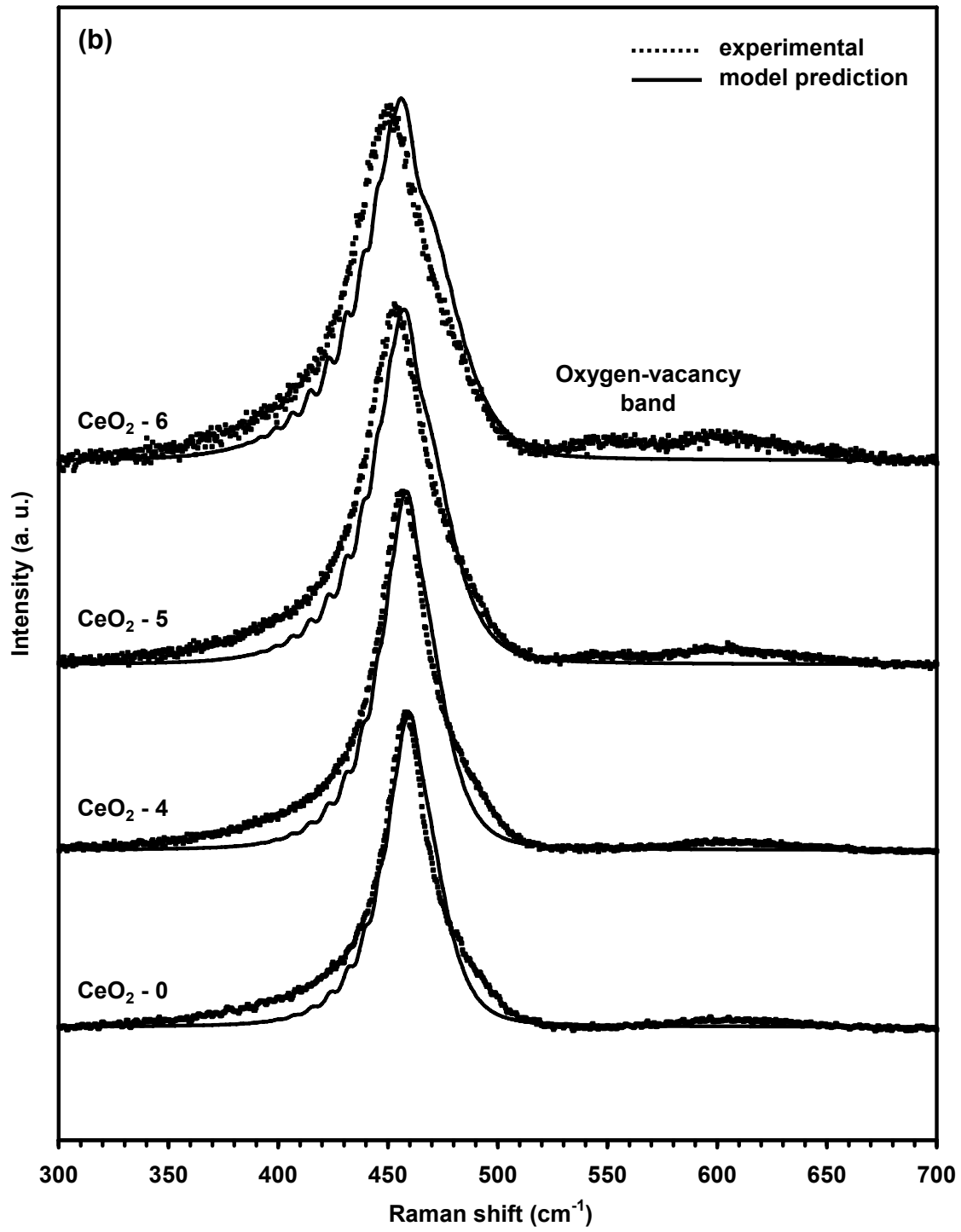
Figure 3.6 (b) presents the defect concentration calculated from the correlation length as given in equation (10). The defect concentration gradually increases with dopant concentration. When  $\text{Ce}^{4+}$  ions are substituted by  $\text{RE}^{3+}$  ions, the oxygen vacancies are introduced into the fluorite lattice by partial reduction of  $\text{Ce}^{4+}$  to  $\text{Ce}^{3+}$  so as to maintain the electric neutrality. This reduction process can be given as follows:



where RE = La or Nd.

Additionally, the broad band in the range of  $540\text{-}640\text{ cm}^{-1}$  increases with doping amount and can be attributed to increased oxygen vacancies in the doped cerium oxide nanoparticles.





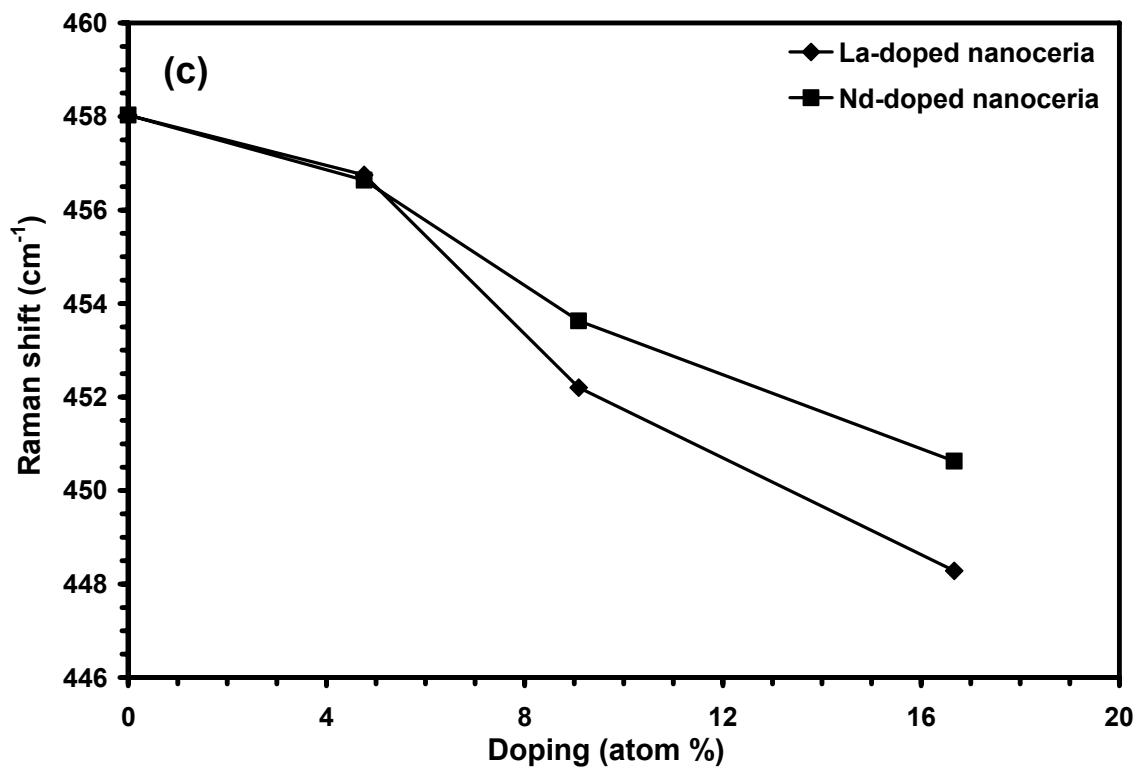


Figure 3.5. Raman spectra of (a) La- and (b) Nd-doped nanoceria samples obtained experimentally (dotted line) and also from the curve fit according to the spatial correlation model (solid line); (c) Raman peak shift of the nanoceria samples as a function of doping amount



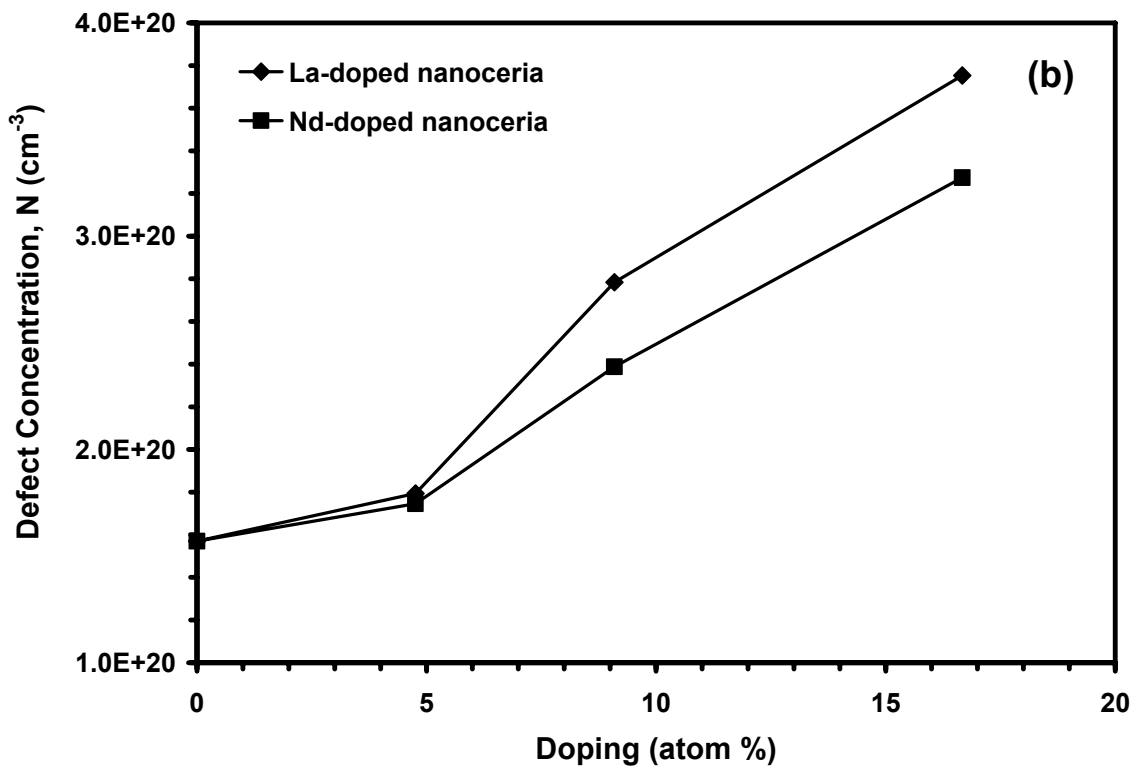
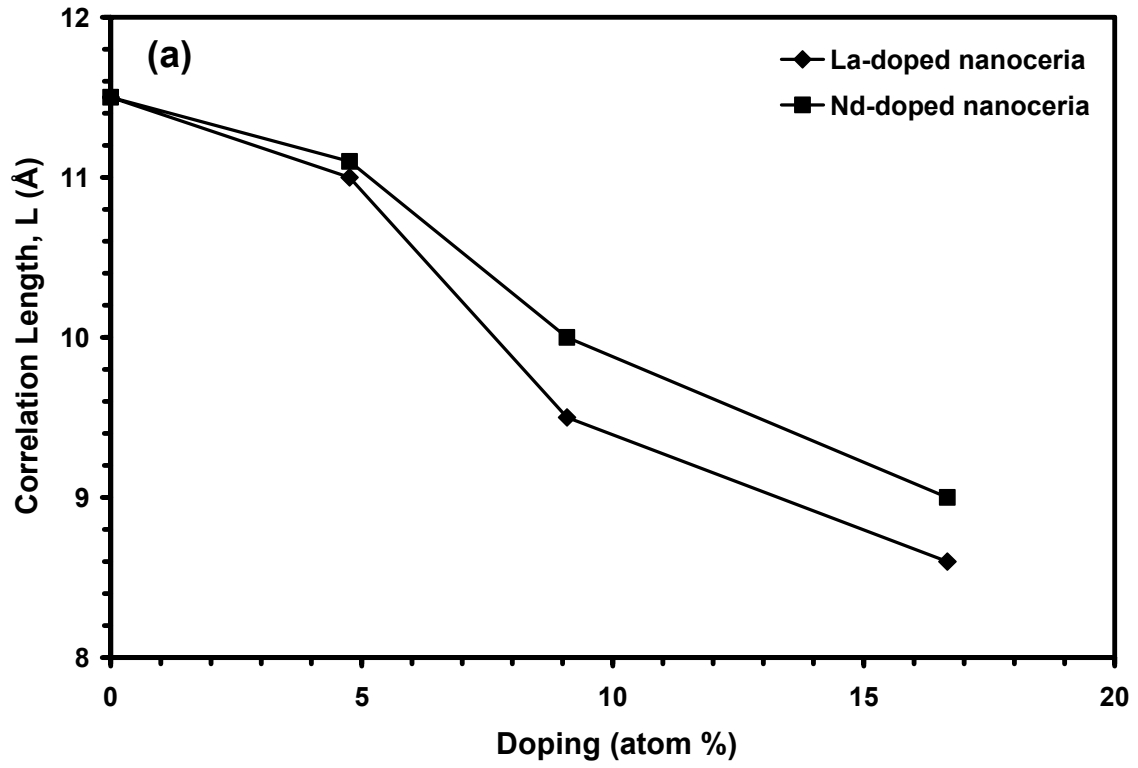


Figure 3.6. (a) The correlation length and (b) oxygen vacancies concentration of the nanoceria samples as a function of doping amount

### 3.4. Conclusions

Cerium oxide nanoparticles show size dependent lattice expansion. The lattice parameter was found to be inversely proportional to the particle size of cerium oxide nanoparticles. Raman spectroscopic studies showed shifting of the Raman allowed line in  $\text{CeO}_2$  ( $464 \text{ cm}^{-1}$ ) to progressively lower energies as the particle size gets smaller and the peak gets broader and asymmetric. The increasing lattice constant with decreasing particle size explains the Raman shift well. The size-dependent lattice expansion and Raman shifting and broadening in  $\text{CeO}_2$  nanoparticles can be further increased by the trivalent dopants. Due to a larger ionic radius, La-doping generates more lattice distortion in the nanocerium compared to Nd-doping.

Spatial correlation model was developed for cerium oxide and used to fit the experimental Raman spectra using the correlation length,  $L$  as the only fitting parameter. The analysis indicated that the lattice expansion observed in cerium oxide nanoparticles as a function of particle size or dopant concentration is due to the formation of oxygen vacancies in the  $\text{CeO}_2$  lattice. The vacancy defects in the nanocrystalline ceria are formed due to reduced enthalpy of oxygen vacancy formation for nanocrystalline microstructure. In case of doping with trivalent elements, the oxygen vacancies are formed to maintain the electric neutrality.

Such non-stoichiometric cerium oxide nanoparticles can be useful in various applications.

## **CHAPTER 4. ELECTROCHEMICAL BIOSENSOR FOR HYDROGEN PEROXIDE DETECTION**

### **4.1. Introduction**

Medical and biotechnological advances in the area of disease diagnosis and treatment are dependent on an in-depth understanding of biochemical processes. Diseases can be identified based on anomalies in the molecular level and treatments are designed based on activities in such low dimensions. Although a multitude of methods for disease identification as well as treatment already exists, it would be ideal to use research tools with dimensions close to the molecular level to better understand the mechanisms involved in the processes. These tools can be nanoparticles, nanoprobes or other nanomaterials, all of which exist in ultra small dimensions and can be designed to interrogate a biochemical process of interest.

Rapid advances in nanotechnology and nanoscience have provided a variety of nanoscale materials with highly controlled and unique optical, electrical, magnetic or catalytic properties. The diversity in composition (organic or inorganic, metals or semiconductors), shape (particles, rods, wires or tubes) and the readiness for surface functionalization (physical, chemical or biological) has enabled the fabrication of various functional nanoscale devices<sup>77-81</sup>. Biologists have recently begun to use these tools and apply them to a variety of applications ranging from diagnosis of disease to gene therapies.

## 4.2. Role of Hydrogen Peroxide in Biological Systems

Hydrogen peroxide is normally found in each aerobic cell. It is generated during normal cell respiration by different metabolic processes and by oxidative stress<sup>82</sup>. It is formed intracellularly by mitochondria, endoplasmic reticulum and peroxisomes, which contain a number of H<sub>2</sub>O<sub>2</sub> generating enzymes. These enzymes include superoxide dismutase (SOD), several oxidases such as glycolate oxidase, urate oxidase and fatty acyl-CoA oxidase and flavin dehydrogenases<sup>83,84</sup>. Superoxides ( $\cdot\text{O}_2^-$ ) can rapidly dismutate to form H<sub>2</sub>O<sub>2</sub> by a protonation reaction. This reaction can occur spontaneously [ $10^5$  (mol/lit)<sup>-1</sup>.s<sup>-1</sup>] or is catalyzed by SOD [ $10^9$  (mol/lit)<sup>-1</sup>.s<sup>-1</sup>]<sup>83,85</sup>.



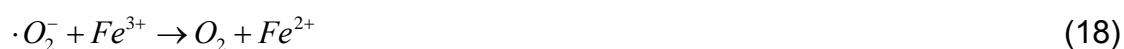
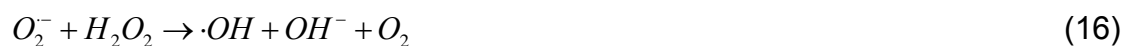
Hydrogen peroxide is not a radical since it does not have unpaired electrons in its outer shell. But it is considered as a reactive oxygen species (ROS) as it can be converted into  $\cdot\text{OH}$  radical by a chain of reactions with other molecules that then can induce toxic effects. Inactivation of critical enzymes by H<sub>2</sub>O<sub>2</sub> can also induce toxicity.

Fenton described in the late nineteenth century the oxidizing potential of hydrogen peroxide mixed with ferrous salts<sup>86</sup>. Forty years later, Haber and Weiss<sup>87</sup> identified the hydroxyl radical as the oxidising species in these reactions:



In biological systems the availability of ferrous ions limits the rate of reaction, but the recycling of iron from the ferric to the ferrous form by a reducing agent can maintain an

ongoing Fenton reaction leading to the generation of hydroxyl radicals. One suitable reducing agent is superoxide which participates in the overall reaction (16) as two half reactions shown in reactions (17) and (18):



Therefore, in the presence of trace amounts of iron, the reaction of superoxide and hydrogen peroxide will form the destructive hydroxyl radical and initiate the oxidation of organic substrates. Metals other than iron may also participate in these electron transfer reactions by cycling between oxidized and reduced states.

In plants,  $H_2O_2$  is generated by many developmental and environmental stimuli and is involved in programmed cell death (PCD), stress adaptation, and plant development<sup>88</sup>. It can act as a signaling molecule as well in these processes.  $H_2O_2$  induced PCD is essential for a number of developmental processes and environmental responses, including aleurone cell death, the hypersensitive response to pathogens and allelopathic plant-plant interactions.

As  $H_2O_2$  is both, important signaling molecule and a toxic byproduct of cell metabolism, its cellular levels are under tight control, and their maintenance has hallmarks of homeostatic regulation. The cell can sense sublethal doses of  $H_2O_2$  and activate peroxide-detoxifying mechanisms; alternatively, upon different cell death stimuli various

H<sub>2</sub>O<sub>2</sub>-producing mechanisms can be activated, and a result of this deliberate H<sub>2</sub>O<sub>2</sub> production a self-destructive PCD is triggered<sup>89-91</sup>.

### **4.3. Hydrogen Peroxide Detection**

#### **4.3.1. Importance**

Hydrogen peroxide is not only the product of the reactions catalyzed by a large number of highly selective oxidases but also an essential mediator in food, pharmaceutical and environmental analysis. Its determination plays an important role in chemical, biological, clinical and many other fields. Accurate measurements of H<sub>2</sub>O<sub>2</sub> using a reliable sensor can be useful in many different ways.

It can be used as an increasingly important tool by preventive medicine practitioners, and can become an integral component of routine medical examinations. By utilizing an individual's Oxidative Stress Profile in conjunction with other medical data, a physician can advise patients whether they are at unusual risk for oxidative stress-mediated disease and can recommend what follow-up action needs to be taken. Many hereditary diseases, including Down's syndrome, sickle cell anemia and diabetes appear to be accompanied by unusually high levels of oxidative damage. Oxidative stress damage measurement by means of H<sub>2</sub>O<sub>2</sub> determination can provide useful information for treatment to reduce the severity of the disease. There are a number of drugs that have serious side effects associated with unusually high levels of oxidative stress. Monitoring an individual's oxidative stress profile will aid physicians in controlling these side effects. It can play an important role in the development of new drugs having minimum side

effects, as well as in the development of drugs and functional food formulations designed to control oxidative stress levels.

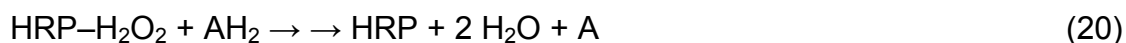
The food we eat represents an important source of our essential antioxidants to reduce oxidative stresses. Yet a specific strain of vegetable, fruit, or any other plant can have wide differences in antioxidant content depending on breeding, cultivation, harvesting and processing conditions. Quality control during food manufacturing and processing often requires close monitoring of the antioxidant status. A reliable H<sub>2</sub>O<sub>2</sub> sensor provides the advanced analytical techniques to assess the antioxidant content of plants as well as food products. This allows us to identify the best strains, and harvesting and food processing conditions to ensure maximum antioxidant content.

#### **4.3.2. Current Detection Techniques and Their Limitations**

Sensitive technique for the analysis of H<sub>2</sub>O<sub>2</sub> is required for developing better insight into the complex interactions that characterize the role of H<sub>2</sub>O<sub>2</sub> in biological systems. Many techniques such as titrimetry<sup>92</sup>, spectrometry<sup>93</sup> and electrochemistry<sup>94</sup> have been developed for this purpose.

##### **4.3.2.1. Horse Radish Peroxidase – Linked Assays**

Several assays for detection of H<sub>2</sub>O<sub>2</sub> depend on the oxidation of a detector compound. Horse radish peroxidase (HRP) oxidizes hydrogen donors in presence of H<sub>2</sub>O<sub>2</sub><sup>95</sup> as shown below:



The amount of  $\text{H}_2\text{O}_2$  is estimated by from the decrease in fluorescence of initially fluorescent probes such as scopoletin (7-hydroxy-6-methoxy-coumarin)<sup>96</sup> or by monitoring the increase in fluorescence from previously non-fluorescent materials such as diacetyldichlorofluorescein<sup>97</sup>, *p*-hydroxyphenylacetate<sup>98</sup>, homovanillic acid (3-methoxy-4-hydroxyphenylacetic acid)<sup>99</sup> or *N*-acetyl-3,7-dihydroxyphenoxazine<sup>100</sup>. Spectrophotometric assays based on oxidation of tetramethylbenzidine<sup>101</sup> or phenol red<sup>102</sup> use the same principle.

Although useful, several precautions are necessary to reasonably use and interpret the results obtained from these tests systems for  $\text{H}_2\text{O}_2$  determination. Firstly, several biological substances, including thiol compounds and vitamin C, can serve as substrates for HRP and thus compete with the detector molecule for oxidation, leading to underestimation of  $\text{H}_2\text{O}_2$  formation. Secondly, endogenous catalase for  $\text{H}_2\text{O}_2$  competes with HRP leading to underestimation of  $\text{H}_2\text{O}_2$ . For example, in the scopoletin-HRP-coupled assay, rates of  $\text{H}_2\text{O}_2$  formation in isolated mitochondria or submitochondrial particles ranged from 2% to 76% of those detected by either oxygen consumption or by  $\text{H}_2\text{O}_2$ -induced cytochrome *c* peroxidase formation<sup>96</sup>.

Spectrophotometric detection using HRP-coupled reactions can also have limitations. Direct reduction of the oxidized detector molecule by electron transport components can limit the utility of tetramethylbenzidine in  $\text{H}_2\text{O}_2$  determination, e.g., in mitochondria<sup>101</sup>. Although spectrophotometric detection of  $\text{H}_2\text{O}_2$  with phenol red has been used successfully in purified enzyme-substrate mixtures and to detect  $\text{H}_2\text{O}_2$  release from activated leukocytes<sup>102</sup>, the phenol red-HRP assay is pH-dependent and less sensitive



than fluorescent methods, reducing its utility when attempting to detect H<sub>2</sub>O<sub>2</sub> from vascular tissue.

#### **4.3.2.2. Dichlorofluorescein Fluorescence**

The oxidation of 2'-7'-dichlorofluorescein (DCFH) to the fluorescent compound 2'-7'-dichlorofluorescein (DCF) was initially thought to be a relatively specific indicator of H<sub>2</sub>O<sub>2</sub> formation<sup>103</sup> and has been used extensively in the detection of oxidants produced during the respiratory burst in inflammatory cells, either in cell lysates or in intact cells using flow cytometry<sup>104,105</sup>. The diacetate form of DCFH (DCFH-DA) is taken up by cells, where intracellular esterases cleave the molecule to DCFH, which has been suggested to remain trapped intracellularly. In the presence of H<sub>2</sub>O<sub>2</sub>, DCFH is oxidized to DCF and fluorescence is measured with excitation at 498 nm and emission at 522 nm. However, there are limitations to the interpretation of DCF fluorescence as a specific marker for quantitative intracellular H<sub>2</sub>O<sub>2</sub> formation.

First, the H<sub>2</sub>O<sub>2</sub>-dependent oxidation of DCFH to DCF occurs slowly, if at all, in the absence of ferrous iron<sup>106</sup>. DCF formation is greatly enhanced in the presence of hemecontaining substances, such as hematin, peroxidases, or cytochrome *c*<sup>106-108</sup>. Importantly, peroxidases are capable of inducing DCFH oxidation in the absence of H<sub>2</sub>O<sub>2</sub><sup>108-110</sup>. Thus, alterations in cellular peroxidase activity are likely to be equally if not more important than H<sub>2</sub>O<sub>2</sub> in determining rates of DCF formation and cellular fluorescence. Second, intracellularly formed DCFH does not necessarily remain within the confines of the intracellular space but rather can reaccumulate in extracellular media, where it would be available for reaction with extracellular oxidants<sup>110</sup>.

In addition to peroxidase-dependent oxidation of DCFH, other substances are capable of directly inducing DCF formation in the absence of  $\text{H}_2\text{O}_2$ , including  $\text{ONOO}^-$  and  $\text{HOCl}$ <sup>111,112</sup>. In the presence of heme-containing compounds, lipid peroxides are also capable of generating DCF fluorescence<sup>107</sup>.

Because of the multiple pathways that can lead to DCF fluorescence and the inherent uncertainty relating to endogenous versus artifactual oxidant generation, this assay may best be applied as a qualitative marker of cellular oxidant stress rather than a precise indicator of rates of  $\text{H}_2\text{O}_2$  formation.

#### **4.3.2.3. Ferrithiocyanate**

Hydrogen peroxide oxidizes ferrous iron to the ferric state. Addition of thiocyanate to the ferric ions results in the formation of a red complex with a peak in the 450 to 480 nm range<sup>113</sup>. This method has been used to estimate  $\text{H}_2\text{O}_2$  formation in hepatic microsomes<sup>114</sup>, fibroblasts<sup>115</sup>, and endothelial cells<sup>116</sup> when fluorescent quenching and interference by tissue chromophores prevented use of alternative approaches.

#### **4.3.2.4. Electrochemical Sensors**

Electrochemical detection is coming into widespread use for the trace determination of easily oxidizable and reducible organic compounds, because it provides an easy procedure for direct and selective detection. Additionally, microfabrication techniques can be implemented for miniaturization of the sensors which offer higher sensitivity than macroelectrodes of conventional size as an electroactive molecule can approach the microelectrode from every direction (spherical diffusion)<sup>117</sup>.

Among electrochemical techniques, amperometric biosensors are especially promising. They are based on the detection of electroactive species involved in the chemical or biological detection process. The signal transduction process is accomplished by controlling the potential of the working electrode at a fixed value (relative to a reference electrode) and monitoring the current as a function of time. The applied potential serves as the driving force for the electron transfer reaction of the electroactive species. The resulting current is a direct measure of the rate of electron transfer reaction. It is thus reflecting the rate of the recognition event, and is proportional to the concentration of the target analyte.

A great variety of schemes for implementing the electrochemical biosensing approach, based on different combinations of biocomponents and electrode transducers have been suggested. These rely on the immobilization of enzymes, antibodies, receptors or whole cells on the sensor electrodes. Fundamental aspects of these devices have been reviewed in the literature<sup>118,119</sup>.

In the past few years, various electrochemical biosensors of H<sub>2</sub>O<sub>2</sub> have been developed due to their possibility to couple the rapidity, selectivity, sensitivity and low cost of chemical analysis<sup>120-122</sup>. Amperometric biosensors of hydrogen peroxide based on electron transfer between an electrode and immobilized peroxidase, which catalyzes the reduction of H<sub>2</sub>O<sub>2</sub>, have been widely proposed<sup>123-126</sup>. These biosensors are highly selective towards H<sub>2</sub>O<sub>2</sub> and can offer very high sensitivities<sup>127-129</sup>.

The simplest form of an electrochemical sensor consists of a thin layer of protein (such as enzyme, antibody, DNA), which can be used for direct measurement. HRP is the

most widely used peroxidase for this purpose as it catalyses the reduction of  $\text{H}_2\text{O}_2$ <sup>128,130</sup>. The direct electron transfer of immobilized HRP has been reported to be achieved on different electrodes<sup>131-134</sup>. However, in addition to the problem of leaching of the protein, various factors can prohibit direct electron transfer between electrodes and proteins such as deep burial of the electroactive cofactors in the protein structure, denaturation of the protein at the electrode surface and unfavorable orientation of the protein. The long-term stability of these sensors is a problem, due to the limited thermostability of the biocatalytic layer, e.g. stability of the sensor based on HRP immobilized on colloidal gold/cysteamine was not more than 2 weeks at 4°C due to deactivation of HRP<sup>135</sup>.

A series of organic dyes have been used as electrode surface modifiers, such as methylene blue<sup>136</sup>, methylene green<sup>137</sup>, Prussian blue<sup>138</sup>, phenazines<sup>139</sup>, and thionin<sup>140</sup>, all displaying excellent mediating ability in bioelectrocatalytic reduction of hydrogen peroxide. Methylene blue (MB), a cationic dye whose electrochemical properties are well known in the solution phase, has been used as a redox indicator since its formal potential,  $E^0$ , is between 0.08 and -0.25V (versus standard calomel electrode) in solution with pH 2-8. This redox potential is close to that of most biomolecular redox potentials. A modified carbon electrode based on using this dye as an electron mediator system may be of great interest<sup>141</sup>. However, such low molecular weight soluble mediator is disadvantageous as it can leach out of the electrode, which may lead to a significant signal loss and affect the stability of biosensor.

#### **4.4. Nanocrystalline Cerium Oxide Based Biosensor for H<sub>2</sub>O<sub>2</sub> Detection**

Due to the importance of hydrogen peroxide in biological systems much research has been performed to identify it in the signaling network of oxidative stress. Although the most recent progress in this field has dealt with the origin and mechanism of oxidative stress at the cellular level, many questions are yet to be answered. For example, to date, there is still uncertainty of the in vivo concentration of H<sub>2</sub>O<sub>2</sub> and other ROS due to the limitations in the techniques used to quantify these species as discussed in the previous section. In order to overcome the shortcomings of the present electrochemical sensors, we have developed a new biosensor of hydrogen peroxide based on cerium oxide nanoparticles. As discussed in the previous chapters, cerium oxide nanoparticles possess some unique properties such as, lattice expansion; shifts in Raman allowed modes, formation of oxygen vacancies etc. These properties make cerium oxide nanoparticles suitable for applications in bio-sensing. Furthermore, because of the large specific surface area and high surface free energy, cerium oxide nanoparticles can promote faster electron transfer between the electrodes rendering high fast response time.

##### **4.4.1. Sensor Design, Fabrication and Characterization**

A 3-terminal amperometric sensor consisting of cerium oxide nanoparticles covered working electrode, an Ag/AgCl reference electrode and a gold counter electrode on a glass substrate was designed for H<sub>2</sub>O<sub>2</sub> measurement. The 3-terminal design approach ensures greater linearity in sensor response. The configuration acts like an electrochemical cell consisting of three electrodes: working, counter and reference.

Glass substrate was chosen because it is an inert, inexpensive, rigid material and easy to handle.

Figure 4.1 shows the schematic of the 3-terminal sensor developed for H<sub>2</sub>O<sub>2</sub> detection. The sensor design ensures a large working electrode area for adequate nanoceria deposition; easy access of the working electrode to both, the reference and counter electrode; and small gap between the electrodes to reduce any ohmic resistance drops in the solution and increase the signal to noise ratio. To provide equal access to the working electrode, which interact with both the reference and counter electrodes, the reference and counter electrodes were designed as equidistant crescent shaped structures. The larger length for the electrodes ensures easy handling of the sensor during usage which many times requires dipping of the sensor in testing solutions.

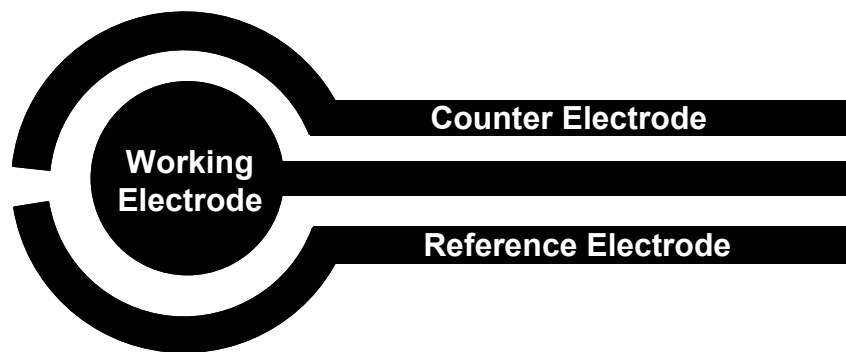


**Figure 4.1. Schematic of the 3-terminal H<sub>2</sub>O<sub>2</sub> sensor design**

A combination of photolithography, wet etching and electroplating technique was employed for microfabrication of the H<sub>2</sub>O<sub>2</sub> sensor. The masks were prepared using

AutoCAD based on the designed shown in Figure 4.1. The details of the fabrication process are as given below.

E-beam deposition was used to form metallic films of Cr/Au on 3-inch glass wafer. After electroplating with Cyanide-less silver electroplating solution from Technic Inc., chlorination of Ag was done with a 0.1 M KCl solution using a photolithographically patterned mold. This defines the Ag/AgCl reference electrode. An additional lithography and wet etching process step generated Au working and counter electrodes. The glass wafer with the number of sensors was then cleaned with acetone, methanol and water to remove the photoresist and dried. Nanocrystalline cerium oxide sol, prepared using the microemulsion technique as explained in previous chapters, was deposited on the working electrode of all the sensors by a microdroplet deposition process and dried at 150°C. Figure 4.2 shows the detailed fabrication process steps. The wafer consisting of multiple fabricated sensors is shown in Figure 4.3.

The fabricated sensors were characterized using scanning electron microscopy (SEM) and focused ion beam (FIB). The surface morphology of the sensor was studied using a JEOL T-300 SEM with an accelerating voltage of 7 kV. Figure 4.4 shows the SEM images of the sensor indicating a good coverage of cerium oxide sol on the working electrode.

The cross sectional analysis of the working electrode of the sensor was carried on a FIB (Model: FEI FIB 200TEM) using a liquid gallium metal ion source in a vacuum of  $10^{-9}$  Torr. 20 X 1 X 1µm platinum layer was deposited on the sensor surface of interest to protect it from ion milling during operational procedures. A cleaning cut was used in

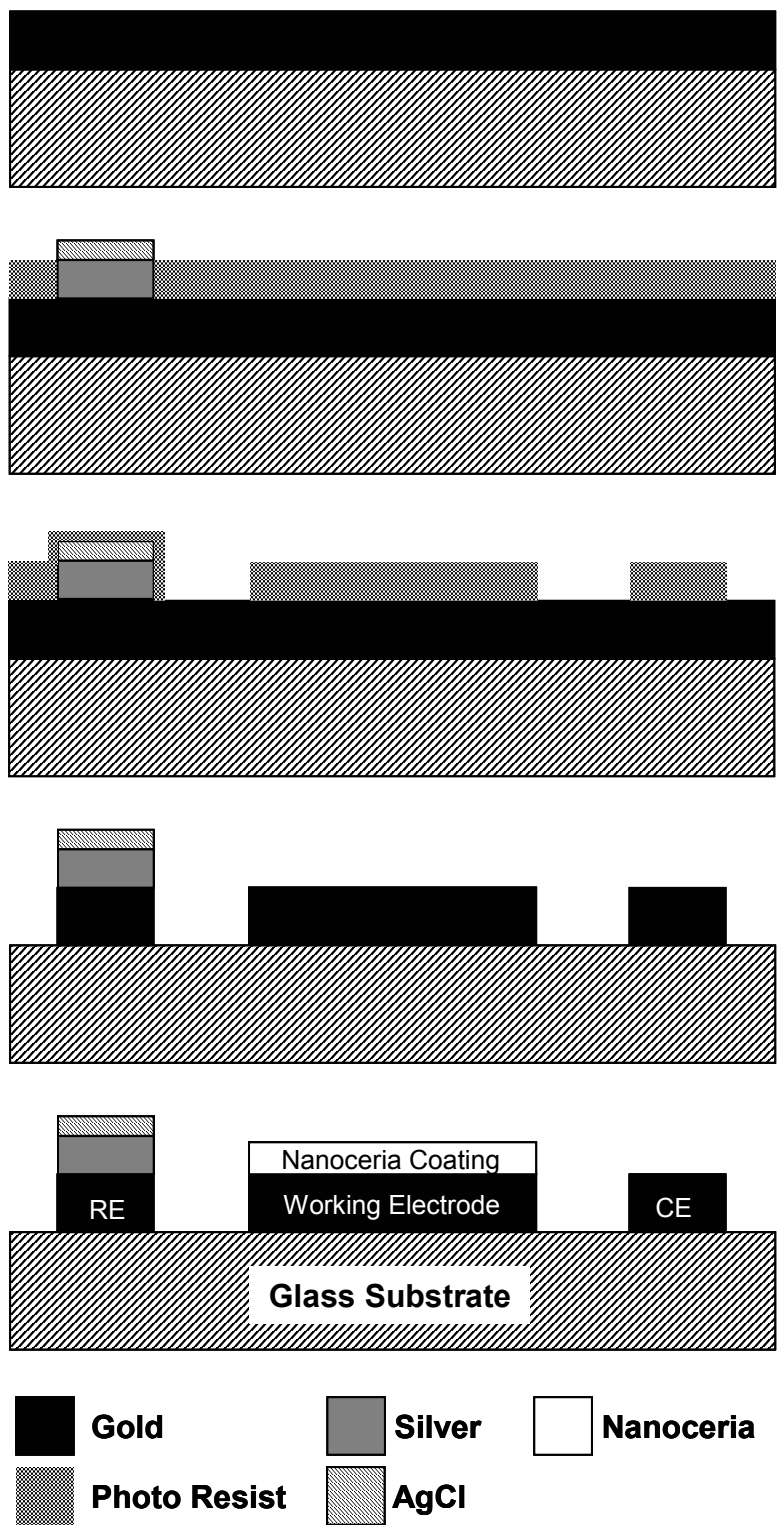
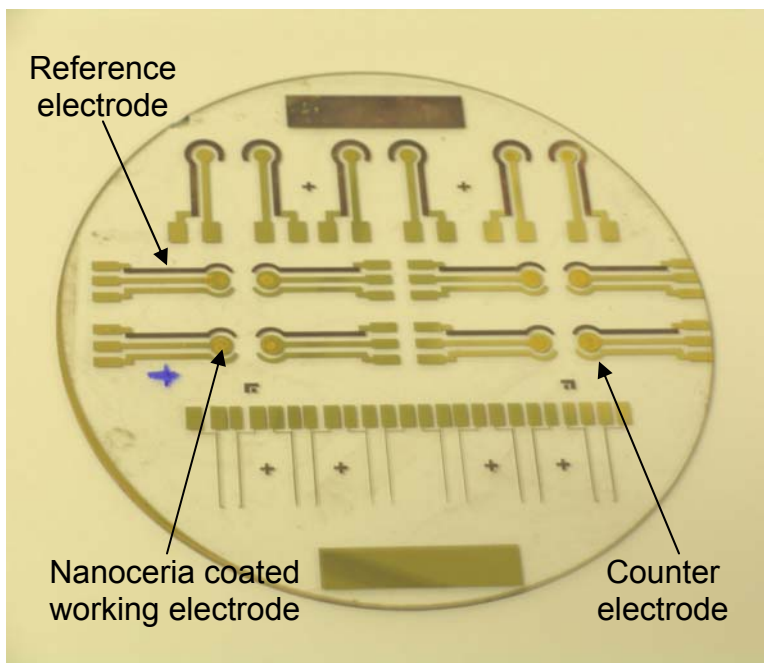


Figure 4.2. Stepwise fabrication process for hydrogen peroxide sensor



front of the deposited Pt layer to create a trench in the sample using a high energy ion beam and then small energy beam was used to finish the cross section for imaging. FIB image of the cross section of the working electrode coated with nanocrystalline ceria sol is shown in Figure 4.5. It reveals four distinct layers: top Pt-layer which was deposited for protecting the surface from the ion milling, nanoceria coating layer below the Pt, a thin Au-working electrode below the ceria coating, and the glass substrate. The nanocrystalline ceria coating thickness was approx. 2  $\mu\text{m}$  on the top of the 0.5  $\mu\text{m}$  thick Au-working electrode. The top portion of the FIB image shows the top surface of the ceria coating due to 45° tilt used to image the cross section. The working electrode was uniformly covered by the nanocrystalline cerium oxide.



**Figure 4.3. Photograph of the fabricated wafer showing multiple sensors**

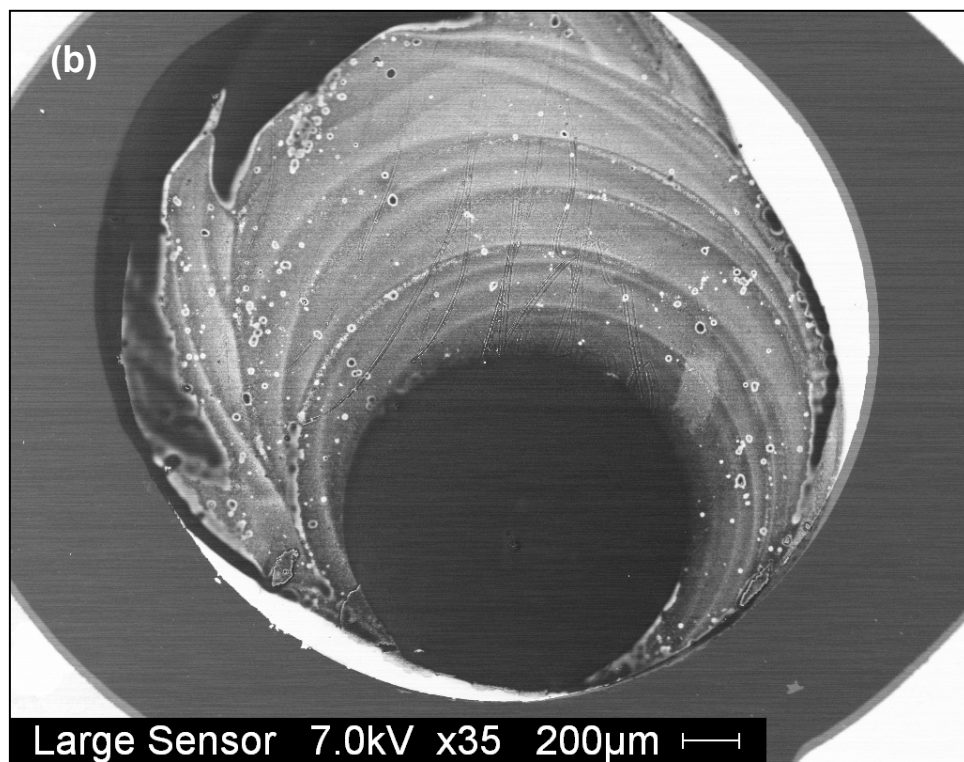
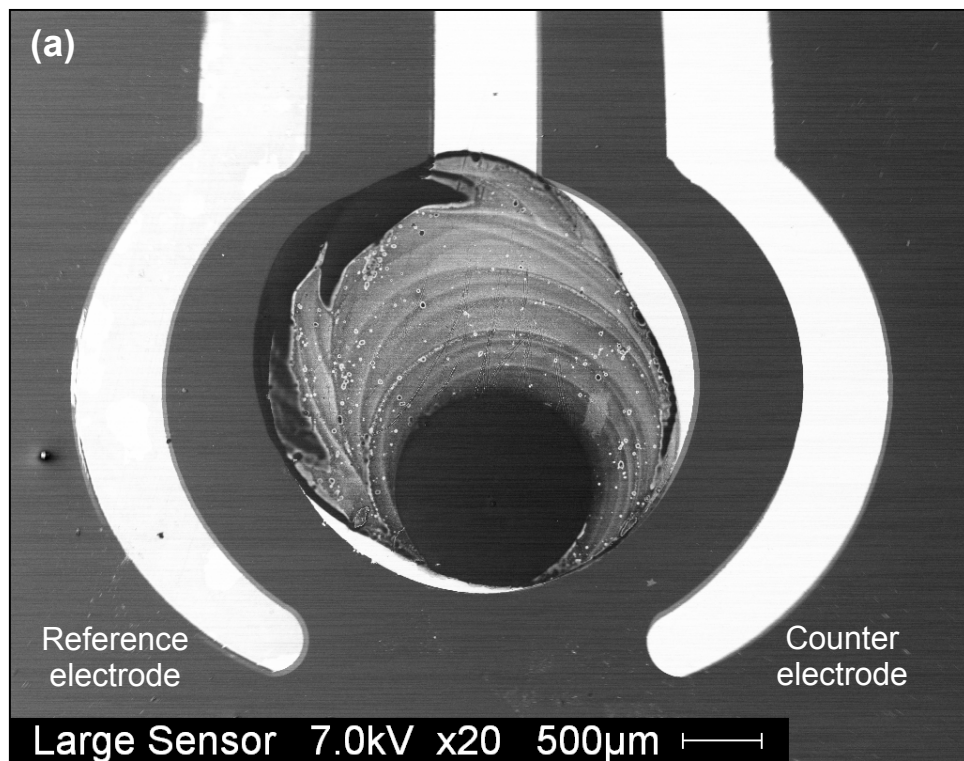
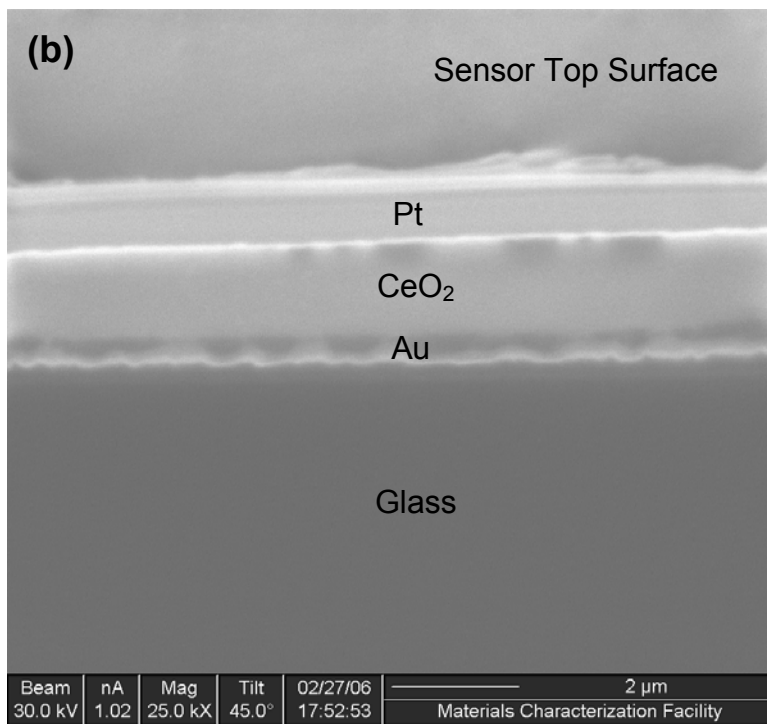
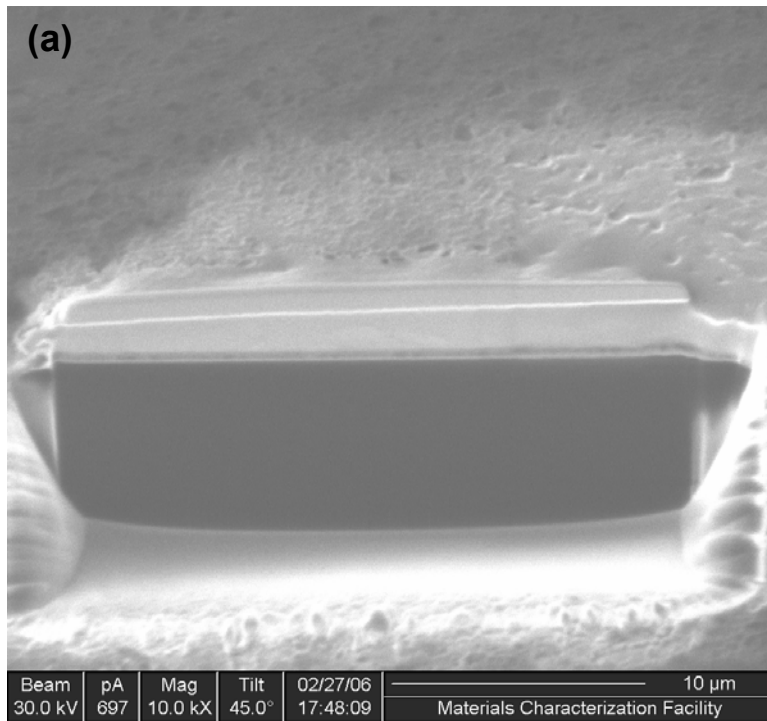


Figure 4.4. SEM images of the fabricated hydrogen peroxide sensor (a) overall sensor and (b) working electrode



**Figure 4.5. Cross sectional analysis of the working electrode studied using focused ion beam technique (a) Trench cut in the sensor working electrode and (b) cross section of the working electrode**

#### **4.4.2. Sensor Test Results and Discussion**

Cyclic voltammetry (CV) is an important analytical technique used in electrochemistry. Cyclic voltammograms trace the transfer of electrons during an oxidation-reduction (redox) reaction. The electrons that are released (oxidation) or taken up (reduction) can be measured as a current, the magnitude of which can be utilized to determine concentration of the analyte.

The three-electrode method, consisting of reference electrode, working electrode and counter electrode, is the most widely used because the electrical potential of the reference does not change significantly during the measurement. Electrodes are placed in an electrolyte solution containing the analyte that will undergo the redox reaction. The potential is measured between the reference electrode and the working electrode and the current is measured between the working electrode and the counter electrode. The potential of the working electrode in the solution is linearly cycled from a starting potential to the final potential and back to the starting potential and the current in the cell is measured as a function of the potential. The current will increase as the potential reaches the reduction potential of the analyte, but then falls off as the concentration of the analyte is depleted close to the electrode surface. As the applied potential is reversed, it will reach a potential that will re-oxidize the product formed in the first reduction reaction, and produce a current of reverse polarity from the forward scan.

Potentiostatic amperometry involves keeping the electrochemical potential at the working electrode constant, which results in an exponential decrease in current as the reaction proceeds. Maintaining the constant potential at the working electrode allows for

the primary component to react without the involvement of other components in the sample. A reference electrode with a known and constant potential is used to measure the potential difference, so that changes to the current can be made qualitatively. This can also be used to determine the analyte concentration.

In the present study, a combination of CV and potentiostatic amperometry was utilized to determine the  $\text{H}_2\text{O}_2$  concentration. As the current at the reduction/oxidation potential of the working electrode is proportional to the analyte concentration it can be used to determine the unknown analyte concentration from a calibration curve prepared with standard solutions. CV was used to find the working potential of the sensor while potentiostatic amperometry was used to determine the current to  $\text{H}_2\text{O}_2$  concentration relation for the sensor at the determined working potential.

All the electrochemical testing of the sensor was carried out using a Sycopel Multistat 2.0 potentiostat. The cyclic voltammogram was obtained by changing the working electrode potential between -1.0 to 1.0 V at the scanning rate of 250 mV/s. Figure 4.6 shows the cyclic voltammogram for 1 mM  $\text{H}_2\text{O}_2$  solution in water. The curve becomes almost flat at + 0.2 V vs. Ag/AgCl reference electrode. This result suggests that transport of hydrogen peroxide towards the electrode surface is not the rate determining step, but that the electron transfer itself or another kinetic step is rate determining<sup>142</sup>.

Earlier XPS studies have shown the presence of a mixed valence state ( $\text{Ce}^{3+}$  and  $\text{Ce}^{4+}$ ) for the synthesized cerium oxide nanoparticles<sup>14,66</sup>. The  $\text{Ce}^{3+}$  ions present in the nanocrystalline ceria can be converted to  $\text{Ce}^{4+}$  in the hydrogen peroxide solution.

Following reactions can be used to describe the chemistry of hydrogen peroxide with cerium oxide nanoparticles<sup>143</sup>:



Here, H<sub>2</sub>O<sub>2</sub> reacts electrochemically with the cerium oxide nanoparticles on the working electrode and oxidize them to form Ce<sup>4+</sup>. But due to various surface chemical reactions the Ce<sup>4+</sup> ions again go back to Ce<sup>3+</sup> valence state making the sensor regenerative.

The potentiostatic amperometry was used to determine the sensor response for varying concentrations of H<sub>2</sub>O<sub>2</sub>. The working potential of 0.2 V was used for all the potentiostatic sensor responses. Figure 4.7 (a) shows the potentiostatic response of the cerium oxide nanoparticles coated sensor for 0.1 mM H<sub>2</sub>O<sub>2</sub> concentration in water at 0.2 V. It can be observed that the current drops parabolically and stabilizes after 40 s. Therefore, the potentiostatic data for varying H<sub>2</sub>O<sub>2</sub> concentrations was obtained for 120 s to get a constant response from the sensor. Figure 4.7 (b) shows the sensor response to H<sub>2</sub>O<sub>2</sub> over a wide range of concentrations. The sensor gives almost linear relationship between current signal and H<sub>2</sub>O<sub>2</sub> concentration in both, micro-molar and mini-molar ranges. Different slopes of the curve at the two ranges can be due to different reaction mechanisms operational at the electrode surface in a competitive way. It is likely that these mechanisms do not act totally independent, and that only one or a limited number of steps of the mechanisms are different, but that these dissimilar steps result in different reaction orders for hydrogen peroxide<sup>131</sup>.

When the sensor was not in use, it was stored at room temperature with no special storage conditions. The response of the sensor was almost unchanged even after 30 days of storage. The stability of the sensor is much better than that of the many existing sensors which require special storage conditions, such as temperature, soaking in buffer solution etc., due to the enzymatic materials involved in the sensor<sup>131,135</sup>. The excellent storage stability of the sensor can be attributed to the stable cerium oxide nanoparticles, a ceramic material, and no enzymes or biological entities involved in the sensor.

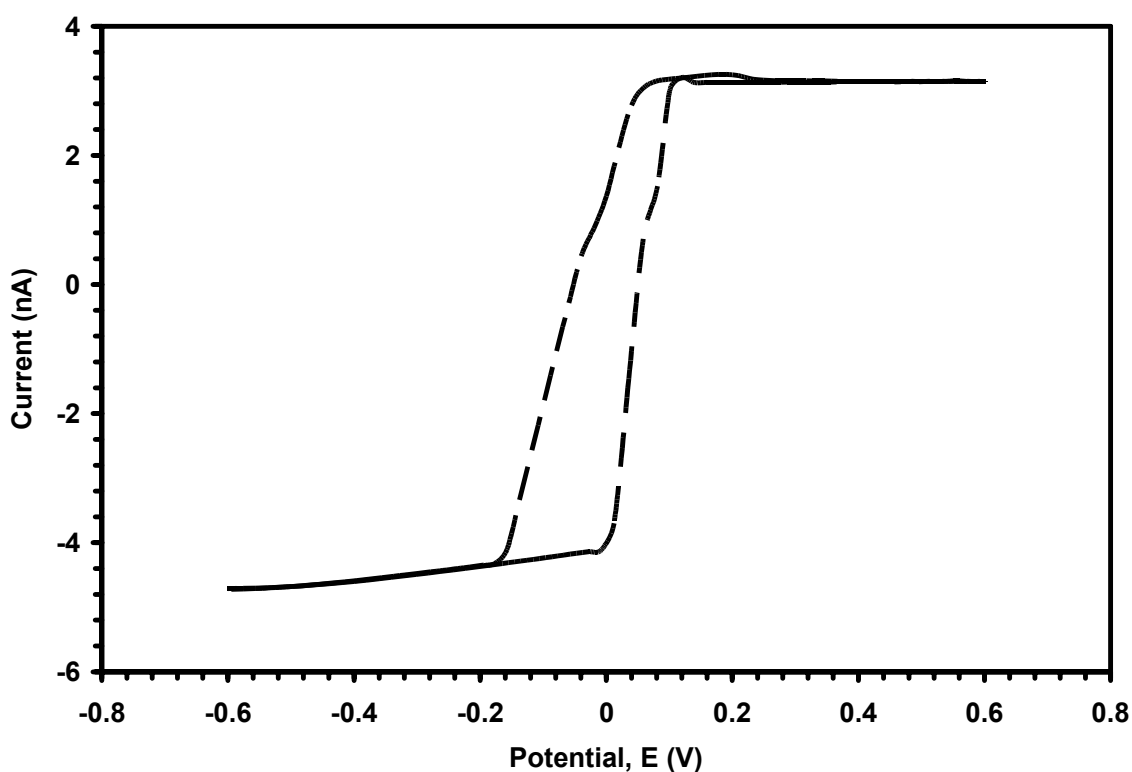


Figure 4.6. Cyclic voltammogram of the nanoceria coated sensor in 1 mM H<sub>2</sub>O<sub>2</sub> solution in water

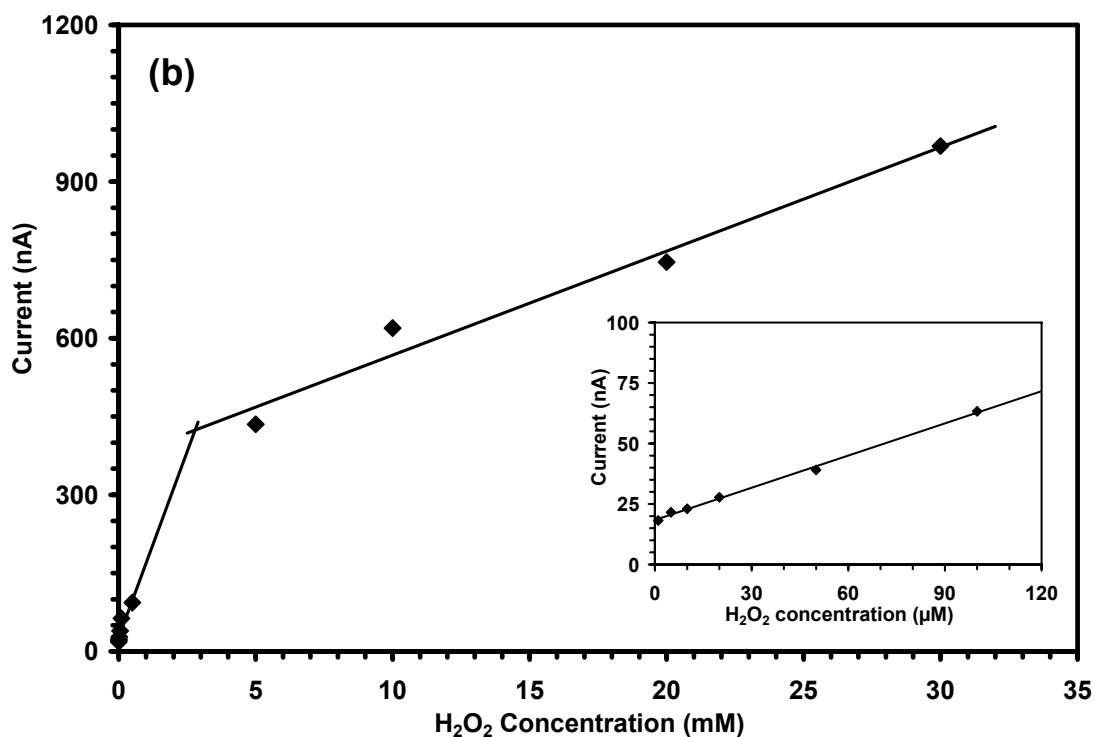
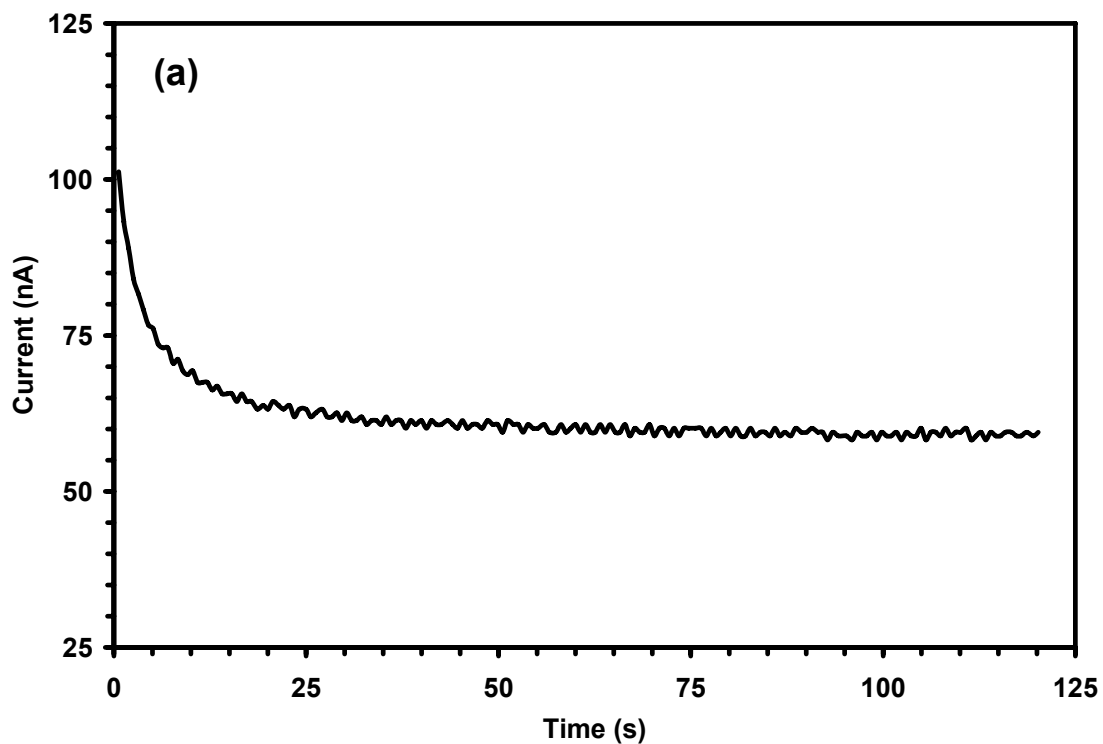


Figure 4.7. (a) Potentiostatic response of the nanoceria coated sensor for 0.1 mM H<sub>2</sub>O<sub>2</sub> concentration; (b) Potentiostatic current Vs H<sub>2</sub>O<sub>2</sub> concentration response of the nanoceria coated sensor, The inset graph is an enlargement of the low H<sub>2</sub>O<sub>2</sub> concentration region. The applied potential was 0.20 V



To test the feasibility of the cerium oxide nanoparticles sensor to measure  $\text{H}_2\text{O}_2$  from biological materials, preliminary studies to determine  $\text{H}_2\text{O}_2$  in leaf and stem tissues of tomato were conducted. Presently, conventional enzymatic assays such as KI-starch assay and the TMB (tetramethyl benzidine) assay are used to quantify  $\text{H}_2\text{O}_2$  in these tissues. KI-starch assay is sensitive up to approximately  $250 \mu\text{M}$   $\text{H}_2\text{O}_2$  concentration whereas the TMB assay has an increased sensitivity of  $\text{H}_2\text{O}_2$ /peroxidase of approximately  $5 \mu\text{M}$ <sup>144</sup>.

Leaves and stem sections (200 mg) from 6 to 8 week-old plants were frozen and ground to a powder in liquid nitrogen, the powder was extracted with 1mL of 0.2M  $\text{HClO}_4$ , incubated on ice for 5 min, and pelleted by centrifugation (10,000g) for 10 minutes at  $4^\circ\text{C}$ . The supernatant was adjusted to pH 7.5 with 0.2 M  $\text{NH}_4\text{OH}$  (pH 9.5) and was centrifuged at 3000g for 2 minutes. The extracts were passed through AG 1X-8 resin columns (ionic-form chloride; Biorad) and samples were eluted with double-distilled water<sup>145</sup>.

Figure 4.8 (a) shows the cyclic voltammograms for both healthy stem and leaf extracts. The different response of the sensor to different tissues can be attributed to different intracellular chemicals present in the stem and leaf. The reduction potential peak was obtained at 0.6 V and 0.35 V respectively for the stem and leaf extract. Therefore, these voltages were taken as working potentials for the  $\text{H}_2\text{O}_2$  determination in the respective samples.

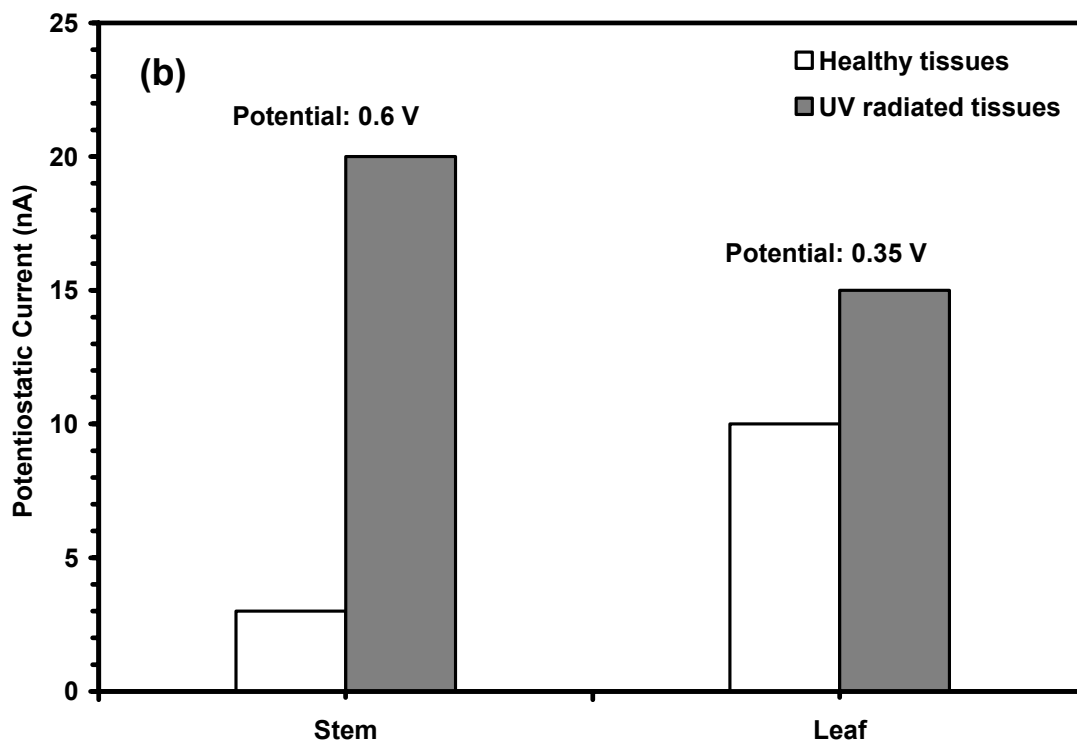
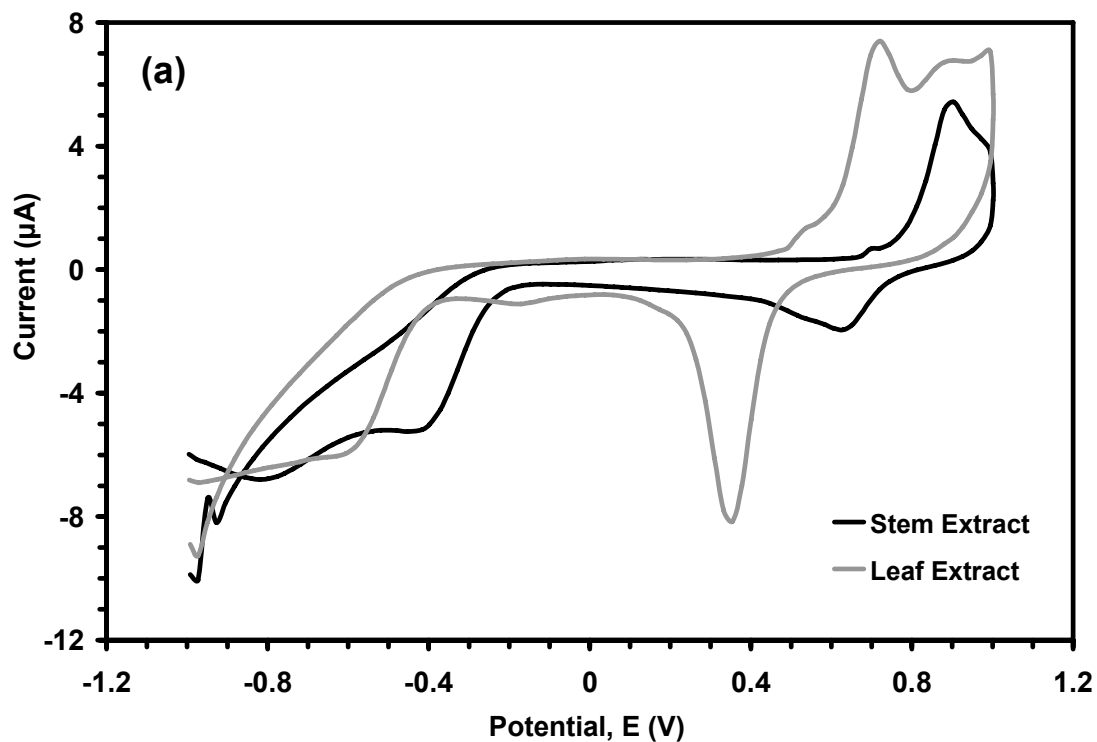


Figure 4.8. (a) Cyclic voltammograms of healthy stem and leaf extracts from a tomato plant; (b) Potentiostatic currents from the healthy and UV radiated stem (applied voltage: 0.60 V) and leaf (applied voltage: 0.35 V) extracts from a tomato plant.

To ensure that the sensor was able to detect changes in  $\text{H}_2\text{O}_2$  concentration in biological samples, the tissues were stressed by exposing to UV-C radiation for 4 hours. UV-C radiation induces apoptotic-like effects in plant cells, including the production of ROS and nuclear fragmentation and DNA laddering<sup>146</sup>. In previous studies, a greater amount of  $\text{H}_2\text{O}_2$  was found in wounded leaves versus healthy leaves,  $\sim 0.2$  vs.  $2.2 \mu\text{M}$  of  $\text{H}_2\text{O}_2/\text{g}$ -fresh weight, respectively<sup>147</sup>. The potentiostatic response of the healthy and UV-radiated tissue extracts is shown in Figure 4.8 (b). Higher current signal in case of the UV-radiated tissue extracts suggest presence of higher amount of  $\text{H}_2\text{O}_2$  as expected.

#### **4.4.3. Regenerative Property of Cerium Oxide Nanoparticles**

We propose that cerium oxide nanoparticles act as a regenerative material in sensing hydrogen peroxide.  $\text{Ce}^{3+}$  ions are converted to  $\text{Ce}^{4+}$  due to reaction with hydrogen peroxide as shown in equation (21). But another complex set of surface chemical reactions between the ions in the electrolyte medium and ceria nanoparticles renew the oxidation state from  $\text{Ce}^{4+}$  to  $\text{Ce}^{3+}$ <sup>148</sup>. Perhaps there is an auto-regenerative reaction cycle ( $\text{Ce}^{3+} \rightarrow \text{Ce}^{4+} \rightarrow \text{Ce}^{3+}$ ) continuing on the surface of cerium oxide nanoparticles.

To demonstrate the auto-regenerative property of the ceria nanoparticles, a UV-visible spectroscopic study of nanoceria sol treated with 10mM hydrogen peroxide was carried out (Figure 4.9). The UV-Visible spectrum of a sample of nanoceria solution was taken (black trace in the graph). Addition of hydrogen peroxide to this solution shifted the spectrum to right hand side (pink trace). This shift was due to the change in the oxidation state from  $\text{Ce}^{3+}$  to  $\text{Ce}^{4+}$ . The nanoceria sample treated with hydrogen peroxide

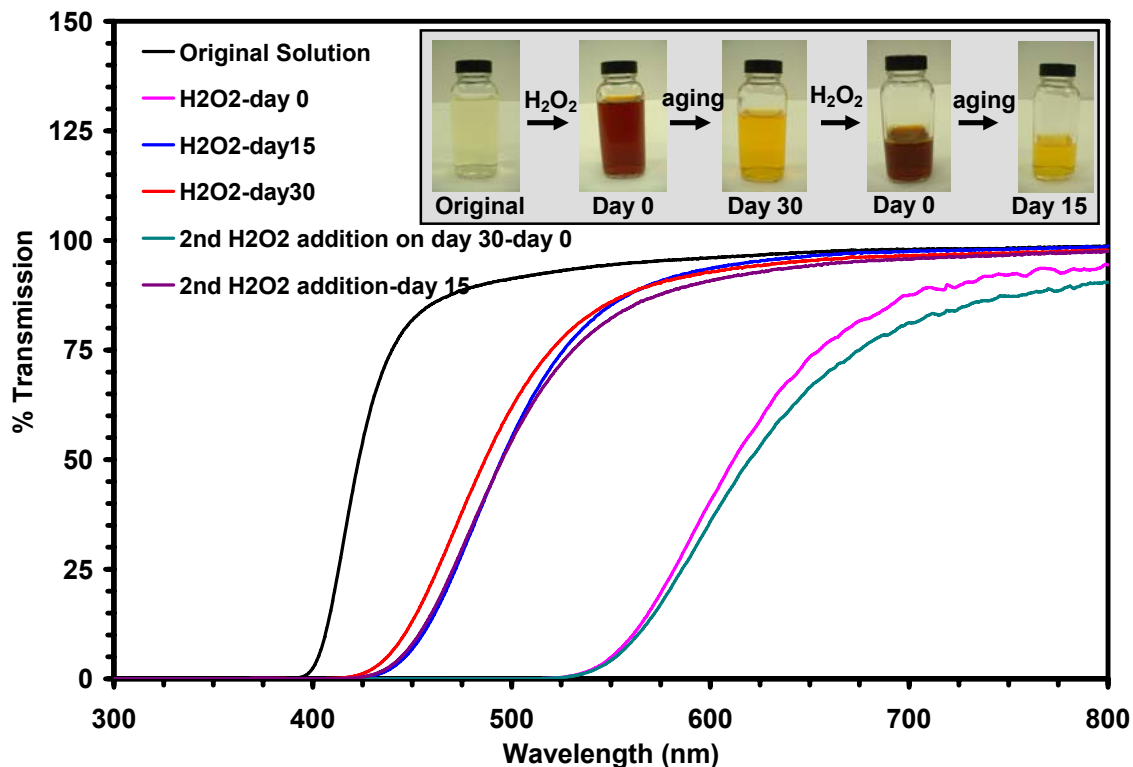


Figure 4.9. Study of regenerative property of cerium oxide nanoparticles using UV-visible spectroscopy

was kept in dark for the next 30 days. UV-Visible spectra of the solution were taken on day 15 and day 30 (blue and red traces show the day 15 and day 30 spectra respectively). A gradual shift in the spectra to the left hand side was seen over time. This gradual left hand shift reflects the gradual recovery process ( $\text{Ce}^{4+} \rightarrow \text{Ce}^{3+}$ ) of the cerium oxide nanoparticles. When additional hydrogen peroxide was added to the solution on day 30, the UV-Visible spectrum again shifted to the right hand side (green trace); followed by a gradual shift to the left similar to the initial response on day 15. The right shift on exposure to hydrogen peroxide with a recovery toward the left indicates that cerium oxide nanoparticles have a capacity for oxidative recovery ( $\text{Ce}^{3+} \rightarrow \text{Ce}^{4+} \rightarrow$

Ce<sup>3+</sup>) and this may be the mechanism by which it provides the material with an auto-regenerative property. The auto-regenerative property of these nanoparticles can be the reason for long term shelf life for the sensor with no significant change in the sensor response.

#### **4.5. Conclusion**

A 3-terminal amperometric biosensor based on cerium oxide nanoparticles was developed. The sensor response was linear with different slopes in both, millimolar and micromolar, H<sub>2</sub>O<sub>2</sub> concentration ranges indicating different mechanisms governing the sensor response in the respective ranges. Preliminary studies with tomato stem and leaf tissues showed promising results indicating the usefulness of the sensor in plant physiology studies as direct H<sub>2</sub>O<sub>2</sub> detection method.

The sensor had a storage life of more than 30 days with no special storage requirements. The long shelf life of the sensor can be attributed to the regenerative property of cerium oxide nanoparticles as studied by UV-vis spectroscopy.

## **CHAPTER 5. APPLICATIONS OF CERIUM OXIDE NANOPARTICLES IN BIOLOGY**

### **5.1. Introduction**

#### **5.1.1. Nanotechnology in Biomedical Applications**

Biomedical sciences and biotechnology have benefited significantly from technological advancement in many fields. Use of nanotechnology in biological and medical science holds a significant promise and the research in this area is rapidly developing. A nanometer is one-billionth of a meter; it is at this size scale – about 100 nanometers or less – that biological molecules and structures inside living cells operate. Nanomaterials can be used for intervention at the molecular scale to cure diseases or repair damaged tissues, such as bone, muscle, or nerve.

Recent advances in nanotechnologies have provided various nanostructure materials, such as quantum dots, metal nanospheres, nanoshells, nanorods, carbon nanotubes (CNTs)<sup>77,149-154</sup>, which have promising and highly controllable properties for medical purposes, ranging from diagnosing diseases to providing novel therapies. Site-specific targeted drug delivery (made possible by the availability of unique delivery platforms such as dendrimers, nanoparticles, and nanoliposomes) and personalized medicine (a result of advances in pharmacogenetics and pharmacogenomics) are few of these applications which may be on the horizon.

New approaches to using nanotechnology in medicine are continually being discovered, and more are anticipated in the very near future. Although the full potential of nanomaterials in biotechnology is years or decades distant, recent advances in nanotechnology- related drug delivery, diagnosis, and drug development are beginning to change the landscape of medicine. It has the potential to change medical science dramatically in the 21st century.

### **5.1.2. Reactive Oxygen Species (ROS): Role in Biology**

Reactive oxygen species (ROS) and free radicals, including superoxide ( $\bullet\text{O}_2^-$ ), hydrogen peroxide ( $\text{H}_2\text{O}_2$ ), hydroxyl radical ( $\bullet\text{OH}$ ) and nitrogen oxide ( $\text{NO}_x$ ), are generated *in vivo* as a result of aerobic metabolism or host defense mechanisms<sup>155</sup>. They play an important role in a number of biological processes, some of which are necessary for life, such as the intracellular killing of bacteria by neutrophil granulocytes. They can act as signal transduction and transcription agents in development, stress responses, and programmed cell death<sup>89</sup>. Under normal conditions, healthy cells ameliorate the damaging effects of ROS via innate natural enzymatic mechanisms. However, when production of ROS exceeds the capacities of the cellular defense mechanisms or when cell defense mechanisms are compromised by aging and other pathological states, it can damage cellular components. The burden of ROS imposed upon a cell with age or disease is termed as oxidative stress which is critical to the cell survival or dysfunction. Multitudes of disease pathologies implicate free radicals in tissue damage, including Alzheimer's disease, inflammatory disorders, Parkinson's disease, diabetes, atherosclerosis and hypertension<sup>156-160</sup>. External sources such as

mechanical injury, X-rays and UV radiation are also known to cause cellular dysfunction via excess ROS generation.

### **5.1.3. Free Radical Scavengers**

ROS influence carcinogenesis and cancer progression by causing oxidative damage to macromolecules such as protein, lipid and DNA. Damage to DNA<sup>161</sup>, changes in neuronal cell functions<sup>162</sup>, skeletal muscle atrophy and weakness<sup>163</sup> and changes of cell division and development<sup>164</sup> are all associated with oxidative stress.

Free radical scavengers may be useful therapeutic adjuncts in treatment and prevention of ROS associated disorders, improving the quality of life. The use of free radical scavengers as pharmacological therapy has been reported in many disorders<sup>160,165-168</sup>. Free radical scavengers such as Vitamin E, SOD mimetics, 21-aminosteroids, 2-methylaminochromans (lazaroids) and nitrosone spin traps have been utilized to lessen the severity of the disorder associated with free radical production. However many of these free radical scavengers have met with only limited success. Also the pharmacological use of free radical scavengers has several problematic aspects. The first is lack of penetration to the site of radical production. The second is repeated dosage requirement to replace molecular species that were utilized in free radical reduction.

Development of nanomaterials with a free radical scavenging ability will be a very attractive proposition to address the problems associated with present free radical scavengers. Such nanomaterials can penetrate through the cellular bodies and reach the radical producing sites directly and minimize the cellular damage. We hypothesize



that cerium oxide nanoparticles, acting as antioxidants, may provide substantial improvement in the decline in function and tissue damage associated with ROS.

#### **5.1.4. Cerium Oxide Nanoparticles as Free Radical Scavenger**

Investigations of nanocrystalline cerium oxide have revealed that its lattice constant increases with decreasing nanoparticle size. This has been attributed to an increase in oxygen vacancies in the crystal structure. It is implied that the migration enthalpy of the oxygen vacancy in cerium oxide is smaller at the nanoscale<sup>91</sup>. Additionally, at the nanoscale, the surface area of cerium oxide particles is dramatically increased, increasing the oxygen exchange and redox reactions. Thus, oxygen vacancies are likely to form more readily at the nanoscale.

Earlier studies have shown that nano-molar concentrations of cerium oxide nanoparticles in serum-free cell culture are not toxic. On the other hand, it was observed that the nanoparticles prolonged the brain cell longevity, in an organotypic tissue culture model of rat brain cells, by 2-3 fold or more<sup>169,170</sup>. Also they reduced free radical-induced cell injuries, hydrogen peroxide (H<sub>2</sub>O<sub>2</sub>) treatment and UV light exposure, by over 60%<sup>170</sup>.

We hypothesized that cerium oxide nanoparticles, due to their chemical and physical structure, protect the cells from free radical induced damages. The defects in the nanoparticles can act as chemical spin traps similar to nitrosone compounds, currently used as biological antioxidants. However, one cerium oxide particle may offer many sites of “spin trap” activity, where current pharmacological agents offer only a few per

molecule. Additionally, the defects in cerium oxide nanoparticles possess the potential for regeneration and does not require repetitive dosage as seen with vitamins E and C.

The present report gives additional applications of cerium oxide nanoparticles in various fields of biology to treat free radical induced cellular damage. The results discussed in this section are a collaborative work with various groups expert in their respective fields.

## **5.2. Radioprotection to Normal Cells in Cancer Treatment**

This work has been carried out in collaboration with Dr. Roy Tarnuzzer and his student from M. D. Anderson Cancer Center at Orlando Regional Healthcare Center. It has been published with the author in Nanoletters<sup>171</sup>.

### **5.2.1. Radiation Therapy in Cancer Treatment**

Radiation therapy is one of the most widely utilized procedures for the treatment of cancer. While it is quite efficient at reducing and eliminating cancer cells, the normal cells in close proximity to the treatment site are inevitably exposed to the harmful radiation. During the process, free radicals are formed through ionizing reactions that are then capable of destroying normal tissues. These newly formed free radicals react with both DNA and RNA, resulting in molecular alterations<sup>172</sup>. When cells are exposed to radiation, the level of protective enzymes released, such as superoxide dismutase (SOD), glutathione, and metallothionein increases and DNA repair mechanisms are intensified<sup>173</sup>. While the protective and repair mechanisms for cells are efficient, they are not capable of blocking or rectifying all of the damage. Those symptoms typically

associated with radiation therapy (nausea, vomiting, fatigue, hair loss, etc.) result from the death of the normal tissues.

Ways in which normal cells can be protected from radiation while targeting the tumor cells has been an important area of focus since the 1950's. In an effort to combat these harmful effects of radiation therapy, various free-radical scavengers have been tested for their ability to protect normal cells. The most effective free-radical scavenger to date is amifostine (Ethyol), whose active free thiol metabolite WR-1065 has been shown to prevent both radiation-induced cell death and mutagenesis while facilitating the repair of normal cells<sup>172,174</sup>. Although Amifostin is the only clinically relevant of the various free radical scavengers studied, it suffers from a very short half-life in serum.

Because of the potential of free radical scavenging compounds to act as radioprotectants, we wanted to see if cerium oxide nanoparticles could confer radio resistance to normal cells during ionizing radiation treatment.

### **5.2.2. Experimental Results**

CRL-8798, an immortalized normal breast epithelial cell line, and MCF-7, breast carcinoma cell line, obtained from American Type Culture Collection (Manassas, VA), were plated at 5,000 and 25,000 cells per well in a 96 well plate, respectively. These plates were tested for cytotoxicity of cerium oxide nanoparticles and then for radioprotection induced by cerium oxide nanoparticles as explained below.

To study the cytotoxicity of the cerium oxide nanoparticles, sterile filtered cerium oxide nanoparticles were added to each well at concentrations from 0 to 5  $\mu\text{M}$  and viability

was measured by MTT assay at 24 hours. It was observed that cerium oxide nanoparticles had no significant toxic effect on CRL8798 and only a slight effect on MCF-7 cells at concentrations greater than 50 nM as shown in Figure 5.1.

To study the damaging effects of different radiation dosage on the cell lines, the plates were irradiated at the dose of 0 to 10 Gy, returned to a 37°C incubator and viability measured at 24 and 48 hours by MTT assay. The viability assay at 48 hours for MCF-7, human breast tumor cell line, shown in Figure 5.2 reflected that 10 Gy irradiation was greater than LD<sub>50</sub> dose of ionizing radiation. Normal breast cell line CRL8798 showed a degree of radioresistance at high density plating, but this was negated when cells were plated such that they were actively dividing. Figure 5.3 shows the cell viability of both, CRL8798 and MCF-7, cell lines irradiated with 10 Gy at densities reflecting active cell growth. Both the cell types were killed at 40-50%, but when pretreated with 10 nM cerium oxide nanoparticles, CRL8798 cells were protected almost 100% whereas in MCF-7 cells, nanoceria showed no statistically significant protection from radiation-induced cell death.

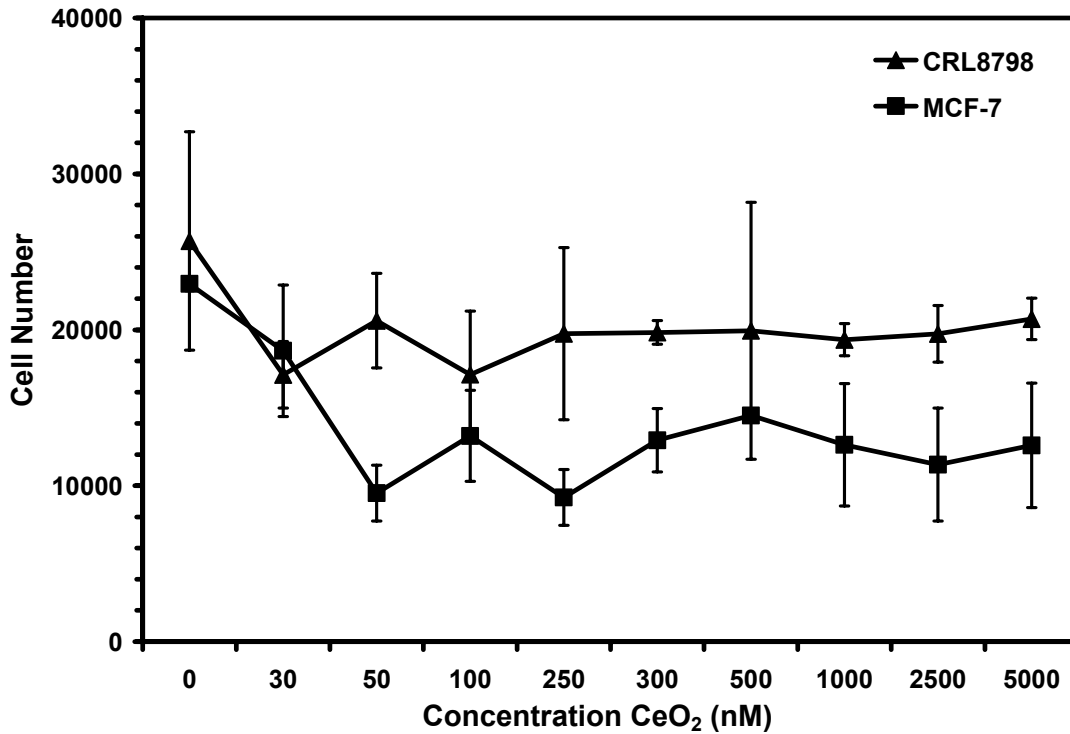


Figure 5.1. Cytotoxicity of cerium oxide nanoparticles on CRL8798 and MCF-7 cell lines in culture

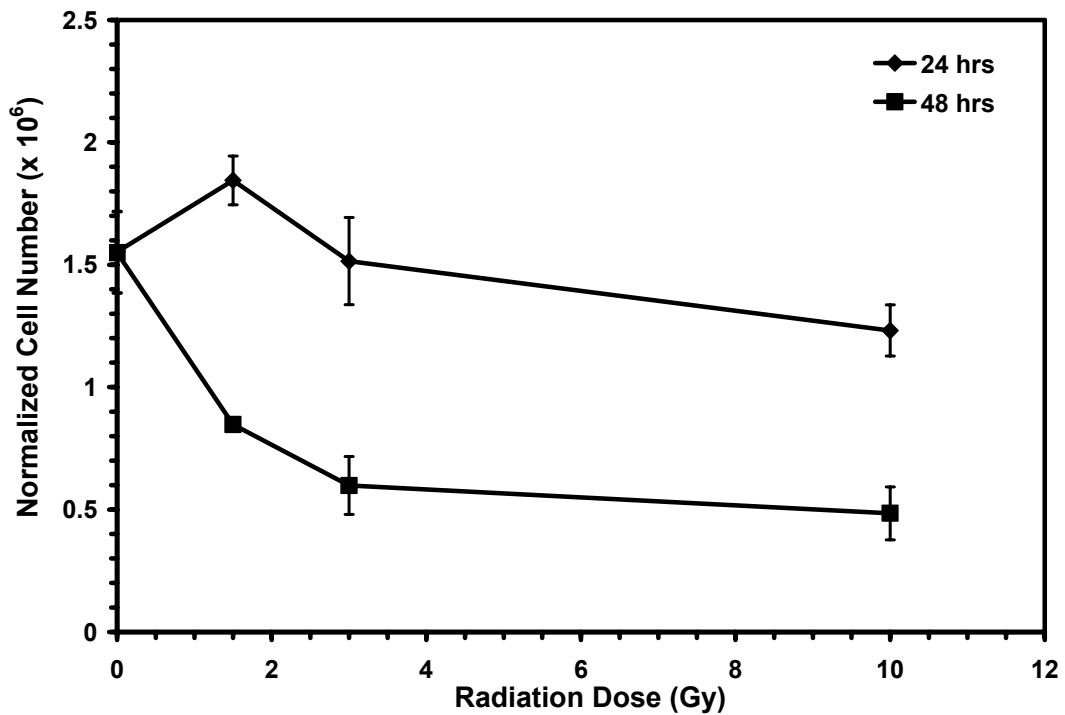


Figure 5.2. Dose response for ionizing radiation and effect on cell viability for MCF-7 cell line

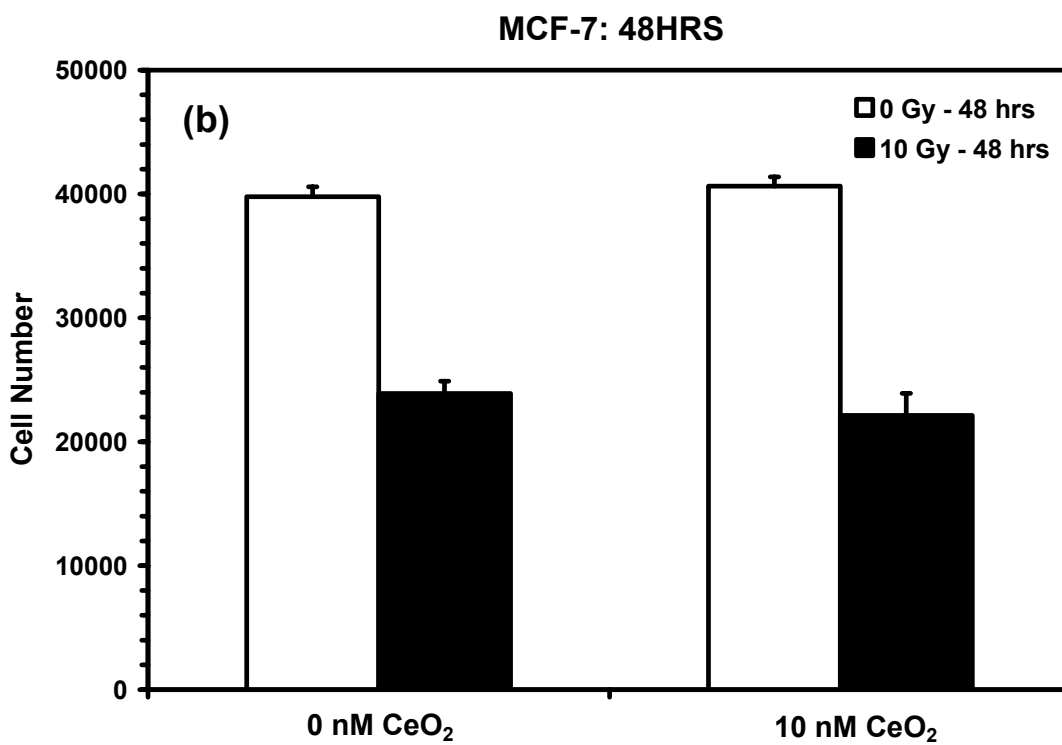
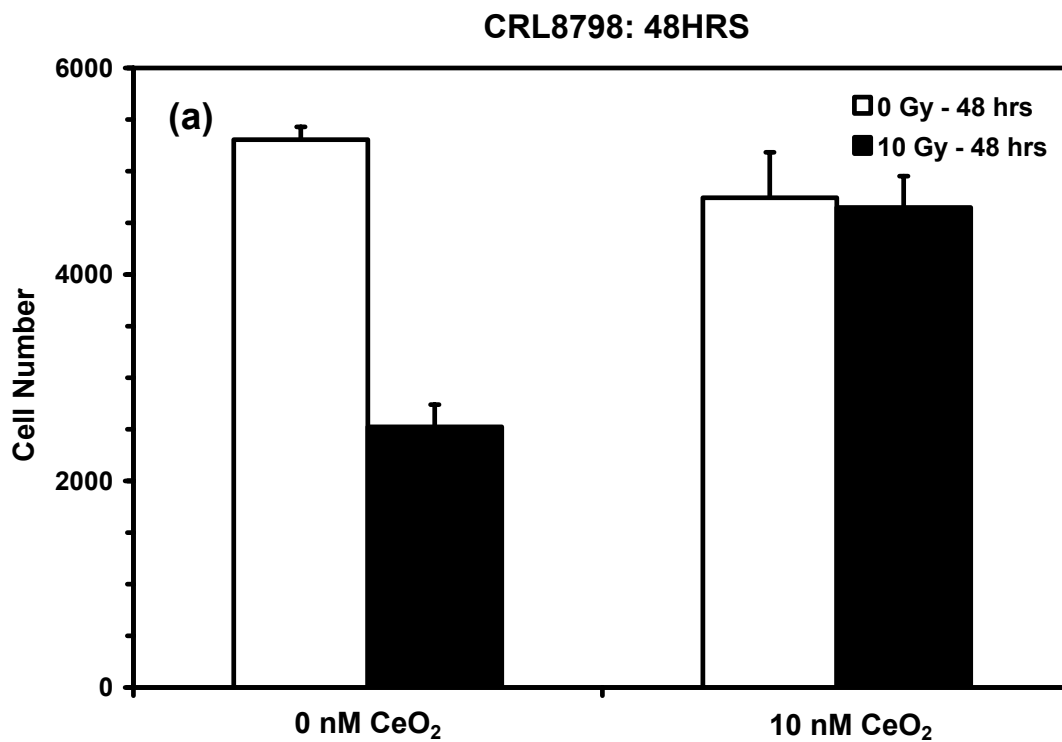
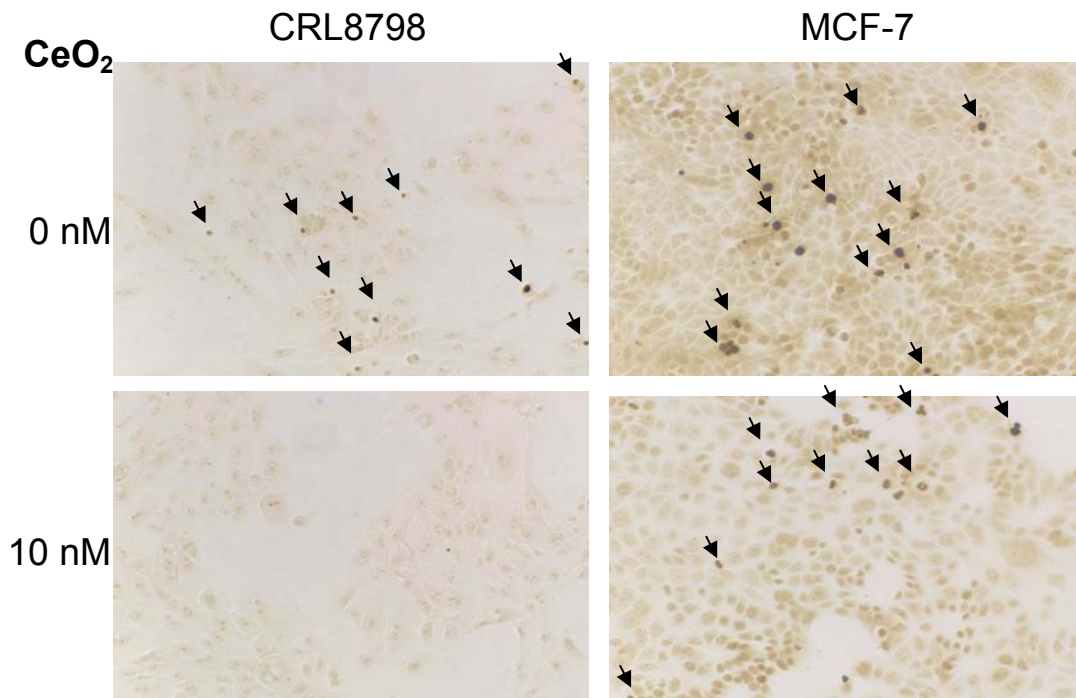


Figure 5.3. Cell viability of (a) CRL8798 and (b) MCF-7 cell lines either with or without 10 nM cerium oxide nanoparticles treatment at 48 hrs after 10 Gy irradiation.



**Figure 5.4. TUNEL staining of CRL8798 and MCF-7 cell lines either with or without 10 nM cerium oxide nanoparticles treatment at 48 hrs after 10 Gy irradiation studied using light microscopy (The arrows denote TUNEL positive apoptotic nuclei)**

To look at the protective effect of cerium oxide nanoparticles on radiation-induced apoptotic cell death, cells were grown on chamber slides and pretreated with 10 nM nanoceria for 24 hours. Slides were irradiated with 10 Gy and incubated at 37°C for 48 hours. Cell death, for adherent and non-adherent cells, was measured by TUNEL staining for both CRL8798 and MCF-7 cells. Figure 5.4 shows the light microscope images of the TUNEL staining assay for both the cell lines. As seen with MTT cell viability assays, both CRL8798 and MCF-7 can be induced to undergo apoptosis following radiation exposure. When pretreated for 24 hours with 10 nM nanoceria, CRL8798 cells showed almost 100% protection from radiation-induced apoptosis

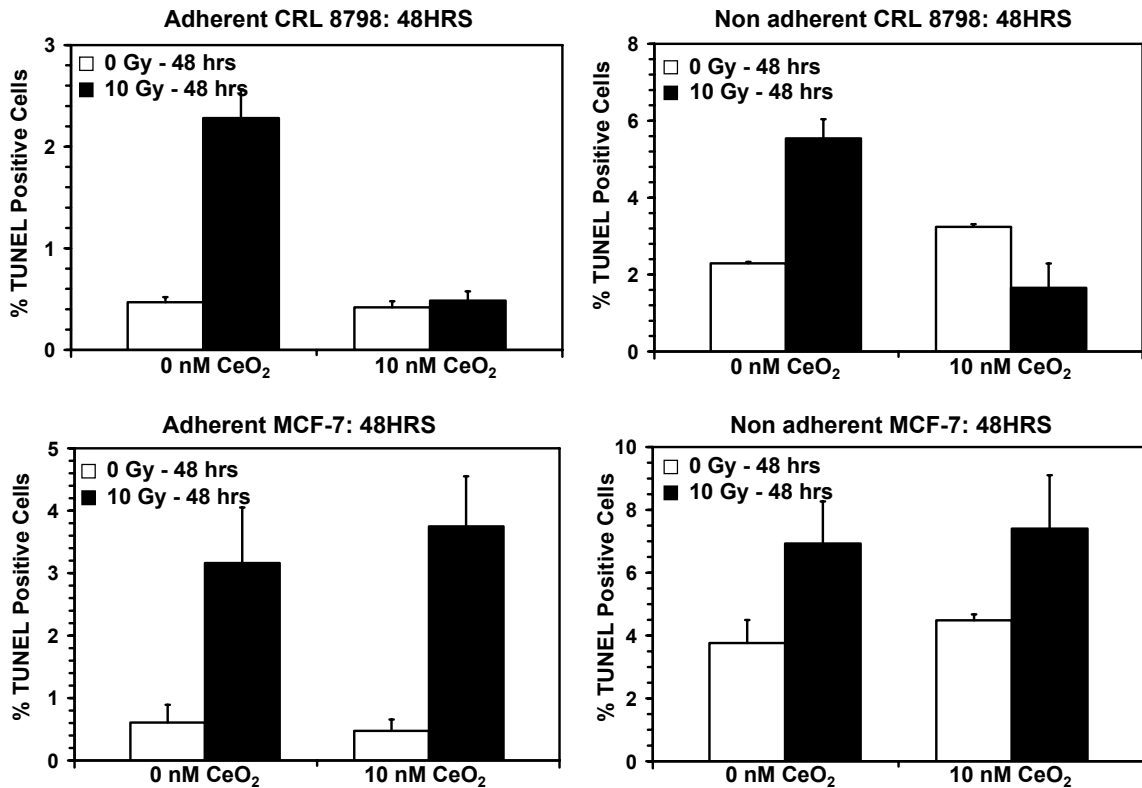


Figure 5.5. TUNEL staining data for, adherent and non-adherent cells, of CRL8798 and MCF-7 cell lines either with or without 10 nM cerium oxide nanoparticles treatment at 48 hrs after 10 Gy irradiation

whereas MCF-7 cells showed no statistically significant protection by nanoceria as can be observed in Figure 5.5.

### 5.2.3. Discussion

Effective long-lived radioprotectants with clinical applications are not well represented in most formularies. Amifostine is the only clinically relevant radioprotectant and it was synthesized in the 1950's at the Walter Reed Army Research Facility. Nanoceria shows some very promising characteristics that may allow it to be a useful radioprotectant. Our studies have demonstrated a differential efficacy in normal versus tumor cells in culture.



This could be due to several reasons such as differential uptake, differential intercellular activity or differences in chromatin structure or free-radical targets. Unpublished data in our lab has demonstrated that the nanoceria is taken up at the same rate by both normal and tumor cells. Inter- and extracellular pH differences are present in tumors versus normal tissue due to metabolic activity of the tumor cells<sup>172</sup> may contribute to the differences seen between normal and tumor cells. Tumor cells tend to have more relaxed chromatin structure that can expose more bases as targets for free-radical attack. A similar concentration of scavenger protecting fewer sites in normal cells versus the more relaxed chromatin and greater number of targets of tumor cells could help account for this observed difference.

In summary, cerium oxide nanoparticles have very low or no toxicity based on the cytotoxicity studies. We propose that nanoceria acts as an antioxidant because of the presence of the mixed valence states of  $Ce^{3+}$  and  $Ce^{4+}$  on the surface. Furthermore, cerium oxide nanoparticles are long-lived and can confer their beneficial effect for extended periods of time without re-dosing. Although not known at present for nanoceria *in vivo*, shortcomings of Amifostine are the following: very short half-life of less than 10 min in serum, toxicity at higher doses, and toxicity based on the route of administration<sup>175</sup>. The present studies suggest that cerium oxide nanoparticles could have a role as an effective radioprotectant for normal tissues as well as show a differential protection in normal cells as compared to tumor cells.

### **5.3. UV protection to Human Keratinocyte Cells**

This work was a collaborative effort with Dr. William Self from Department of Molecular Biology and Microbiology at University of Central Florida as a part of NSF grant (BES0541516).

#### **5.3.1. Toxic Effects of UV Radiation on the Skin: Role of ROS and Its Control**

The toxic effects of UV from natural sunlight and therapeutic artificial lamps are a major concern for human health<sup>176</sup>. Ultraviolet (UV) irradiation present in sunlight is an environmental human carcinogen. The major acute effects of UV irradiation on normal human skin comprise sunburn inflammation (erythema), tanning, and local or systemic immunosuppression. At the molecular level, UV irradiation causes DNA damage such as cyclobutane pyrimidine dimers and (6-4) photoproducts, which are usually repaired by nucleotide excision repair (NER). Chronic exposure to UV irradiation leads to photoaging, immunosuppression, and ultimately photocarcinogenesis. Photocarcinogenesis involves the accumulation of genetic changes, as well as immune system modulation, and ultimately leads to the development of skin cancers.

In the clinic, artificial lamps, emitting UVB (280–320 nm) and UVA (320–400 nm) radiation, in combination with chemical drugs are used in the therapy of many skin diseases including psoriasis and vitiligo. Although such therapy is beneficial, it is accompanied with undesirable side effects of damaging the normal skin cells during treatment leading to the effects similar to those discussed above.

UV radiation induces the formation of reactive oxygen species (ROS), which play an essential role in photoaging and skin carcinogenesis<sup>177</sup>. UV-generated ROS deplete and damage non-enzymatic and enzymatic antioxidant defense systems of the skin. As well as causing permanent genetic changes, ROS activate cytoplasmic signal transduction pathways in resident fibroblasts that are related to growth, differentiation, senescence and connective tissue degradation. While low levels of reactive oxygen species are continuously produced in vivo and are involved in physiological activities processes, there is accumulating evidence for the damaging effects of higher concentrations of ROS generated in vitro and in vivo following UVA and UVB irradiation of the skin<sup>178-180</sup>.

A decrease in the overall ROS load by efficient sunscreens or other protective agents may represent promising strategies to prevent or at least minimize ROS-induced damages to the skin cells. Cosmetic formulations required to absorb UV sunlight are often formulated using a mixture of inorganic sun filters (e. g. titanium dioxide, zinc oxide) and organic UV absorbers (e. g. dibenzoylmethanes and methoxycinnamates). These components are blended to obtain the required UV blocking rating values. During use such formulations react to sunlight in different ways<sup>181</sup>. Some organic UV absorbers can show reduced long term stability to UV light due to various chemical reactions being induced by either UV light or free radicals, which are formed in the formulation after absorption by UV radiation. Inorganic components are not susceptible to degradation by UV. There is, however, a significant probability that inorganic components will lose energy via the surface of the particle by forming free radicals which can go on to attack the organics. Conventionally, this is avoided by coating the inorganic material, although this process is usually only partially successful.

The drawbacks of the current technology induce a need to develop a photostable, UV protective material which minimizes free radicals formation due to UV-irradiation. We believe that cerium oxide nanoparticles, due to presence of mixed valence states ( $\text{Ce}^{3+}$  and  $\text{Ce}^{4+}$ ) can act as a free radical scavenger to protect the skin cells from UV radiation induced oxidative damages. Additionally, the switching between +3 and +4 valence states can lead to increase in the lifetime of the sunscreen developed using cerium oxide nanoparticles.

### **5.3.2. Experimental Results and Discussion**

Keratinocytes (HaCaT cell line) were cultivated in Dulbecco's Modified Eagle Medium (DMEM, Cellgro) containing 4500 mg glucose/lit, L-Glutamine and sodium bicarbonate. The media was prepared with 10% Fetal Bovine Serum (FBS) to ensure proper cell growth and 100 $\mu\text{g}/\text{ml}$  of streptomycin and 100 $\mu\text{g}/\text{ml}$  penicillin (Mediatech, Inc). The keratinocyte cells were pretreated with filter sterilized cerium oxide nanoparticles and irradiation with UV A-B light at 1500  $\text{J}/\text{m}^2$ . The cell viability of the untreated cultures was compared with the nanoparticles-treated cultures using MTT proliferation assay.

Figure 5.6 shows the cell viability data for the control as well as cells treated with varying concentrations of cerium oxide nanoparticles. The UV light reduced the cell viability by approximately 90% in the control sample. The nanoparticles partially protected the cells from the cytotoxic effects of UV irradiation and it was observed that concentrations between 7.5 nM and 10 nM were the optimal concentrations for protection of the cells.

The results obtained from the cerium oxide nanoparticles treated cell cultures prove the hypothesis that cerium oxide nanoparticles would protect keratinocytes from UV radiation induced ROS damage. It supports the earlier findings that cerium oxide in low doses (nM concentrations) is not toxic and has a protective effect against oxidative stress stimuli, such as UV exposure.

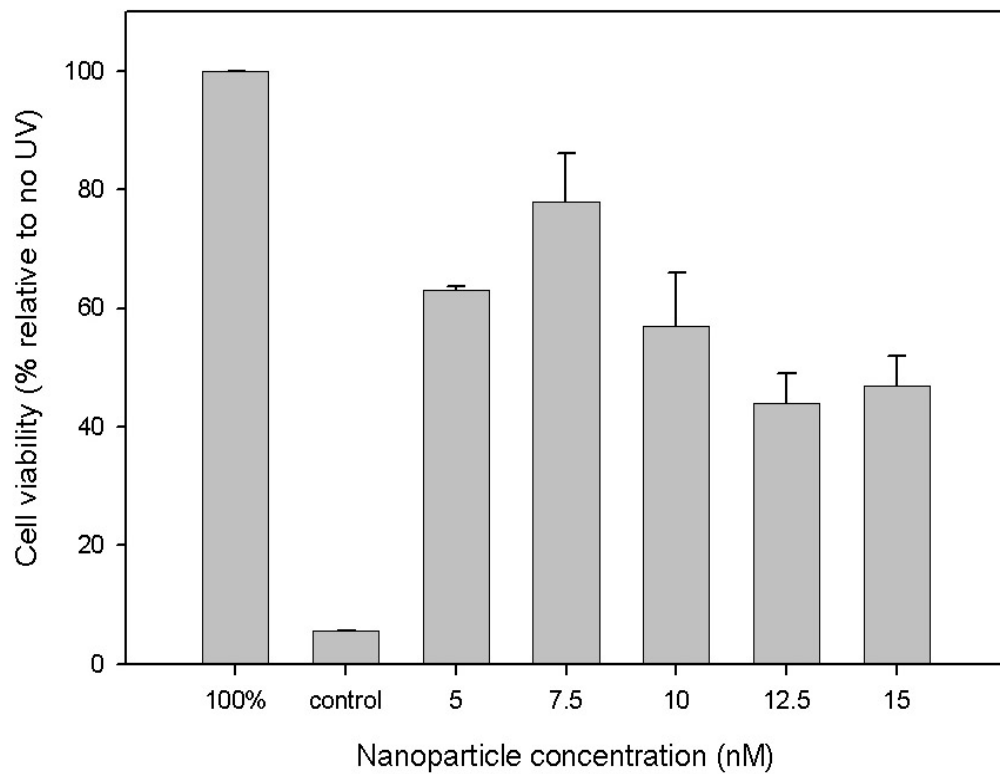


**Figure 5.6. Cell viability of keratinocytes to UVA-B radiation induces damage to varying concentrations of cerium oxide nanoparticles treatment**

## 5.4. Neuroprotection to Adult Spinal Cord Neurons in Culture

This study was carried out with Dr. James J. Hickman and his group from Nanoscience Technology Center at University of Central Florida. The work is to be published with the authors.

### 5.4.1. Introduction

Although the etiology of many diseases of the central nervous system (CNS) is still unclear, several lines of evidence indicate that the generation of ROS plays an important role many neuropathological conditions, such as cerebral ischemia and Parkinson's or Alzheimer's disease<sup>182,183</sup>. Consequently, there is a major interest in developing efficient antioxidants that can protect against neuronal cell injury and death without showing toxic effects.

Spinal cord neurons and other CNS neurons are also prone to damage due to oxidative stress both *in vitro* and *in vivo*. To maintain healthy *in vitro* cultures of spinal neurons and other CNS neurons, several antioxidants are used in the culture medium. The major source of anti-oxidant molecules in serum-free neuron culture medium is the B27 supplement. B27 contains five antioxidants vitamin E, vitamin E acetate, superoxide dismutase, catalase, and glutathione. The half-life of these antioxidants is limited. These antioxidants are replenished each time the medium is changed maintaining a healthy culture.

Presently, we studied the effect of cerium oxide nanoparticles for neuroprotection to adult rat spinal cord neurons. The regenerative property of cerium oxide nanoparticles can also be beneficial to maintain the healthy cultures for longer time.

#### **5.4.2. Experimental Results**

The in vitro studies of the synthesized nanoparticles were carried out in a serum-free cell culture model of adult rat spinal cord which has been shown to promote growth and long-term survival of dissociated adult rat spinal cord neurons<sup>184</sup>. The system consisted of a patternable, non-biological, cell growth promoting organosilane substrate (DETA), coated on a glass surface combined with an empirically derived, novel serum-free medium. The serum-free medium consisted of neurobasal A supplemented with B27, GlutaMAX™, acidic fibroblast growth factor, heparin sulphate, neurotrophin-3, neurotrophin-4, ciliary neurotrophic factor (CNTF), brain derived neurotrophic factor, glial derived neurotrophic factor, cardiotrophin-1 and vitronectin and antibiotic-antimycotic.

In each experiment, equal volume of cell suspension (1000 live cells at the rate of 2 cells/mm<sup>2</sup>) was plated in each coverslip. Of the total number of coverslips plated with cells, half the number was used for control cultures and the other half received a single dose of 10nM filter sterilized cerium oxide nanoparticles at the time of plating the cells. At two different time intervals, day 15 and day 30, live-dead assays and neuron-glia immunostaining assays were conducted to quantify cell viability and the surviving cell types in both control and nanoparticles treated cultures. In both the assays the total number of cells was counted on each of the coverslips. The statistical analysis was

carried out using a student's T-test and the results are expressed as, mean  $\pm$  SE, n=6 where n stands for number of coverslips.

Live-dead cell assays Figure 5.7 indicated a significantly higher cell survival at day 15 ( $617 \pm 34$ , n=6) and at day 30 ( $472 \pm 35$ , n=6) in cerium oxide nanoparticles treated cultures as compared to the control cultures at day 15 ( $479 \pm 37$ , n=6) and day 30 ( $328 \pm 32$ , n=6). A significantly lower cell death was also observed at day 15 ( $59 \pm 7$ , n=6) and day 30 ( $48 \pm 7$ , n=6) in the cerium oxide nanoparticles treated cultures as compared to the control cultures on day 15 ( $110 \pm 9$ , n=6) and day 30 ( $72 \pm 8$ , n=6).

Neurons and glial cells were identified by immunoreactivity for neurofilament 150 (neuronal marker) and glial fibrillary acidic protein (GFAP) (glial marker) antibodies respectively. Neuronal population was significantly higher in ceria nanoparticles treated cultures at day 15 ( $191 \pm 40$ , n=6) and at day 30 ( $221 \pm 12$ , n=6) compared to the control cultures on day 15 ( $71 \pm 26$ , n=6) and day 30 ( $148 \pm 9$ , n=6). There was no significant difference in glial cell population or populations of cells, which stained for both neuron and glial markers in Ceria treated cultures compared to control cultures at either time interval Figure 5.8.

In order to test, the extent of hydrogen peroxide-induced oxidative injury to an aging spinal cord culture, 100 mM hydrogen peroxide was added to 30 days old control and ceria nanoparticles treated cultures. After 1h of hydrogen peroxide treatment, the cell viability was carried out using live-dead assay kit and the results are shown in Figure 5.9. The cerium oxide nanoparticles treated cultures showed significantly higher number of live cells ( $82 \pm 18$ , n=6) as compared to the control cultures ( $29 \pm 6$ , n=6). This result



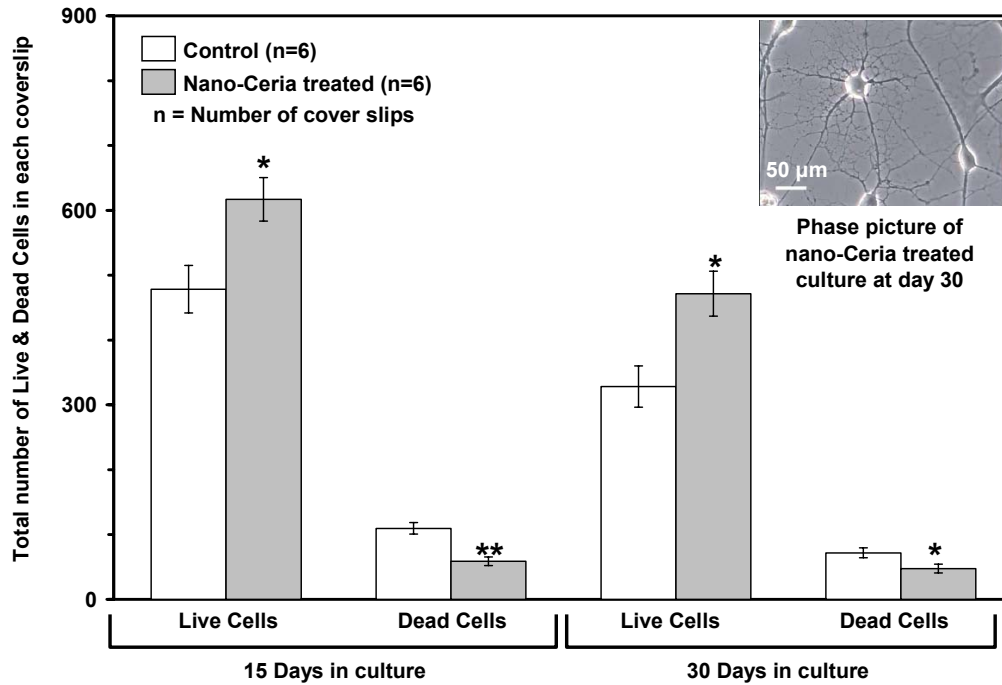


Figure 5.7. Live-dead cell assay indicated that Cerium oxide treated cultures had significantly higher cell survival and significantly less cell death at day 15 and day 30 in culture as compared to the control cultures (\* $p < 0.05$ ; \*\* $p < 0.01$ )

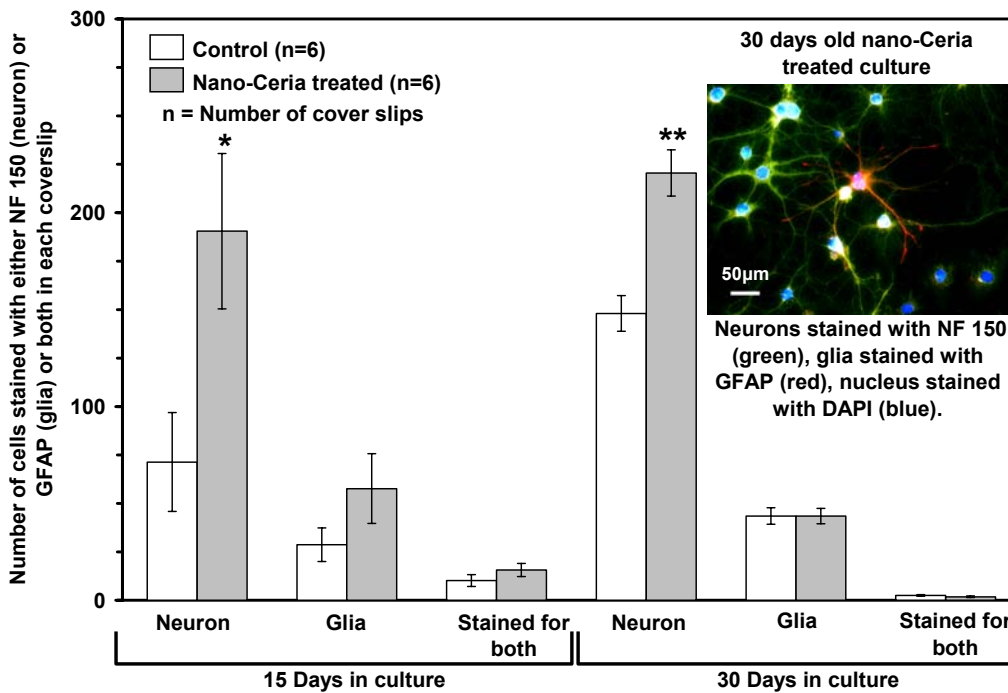


Figure 5.8. Neuron-glia cell assays indicated that a significantly high neuronal survival in Ceria treated culture at day 15 and day 30 as compared to the control cultures (\* $p < 0.05$ ; \*\* $p < 0.01$ )

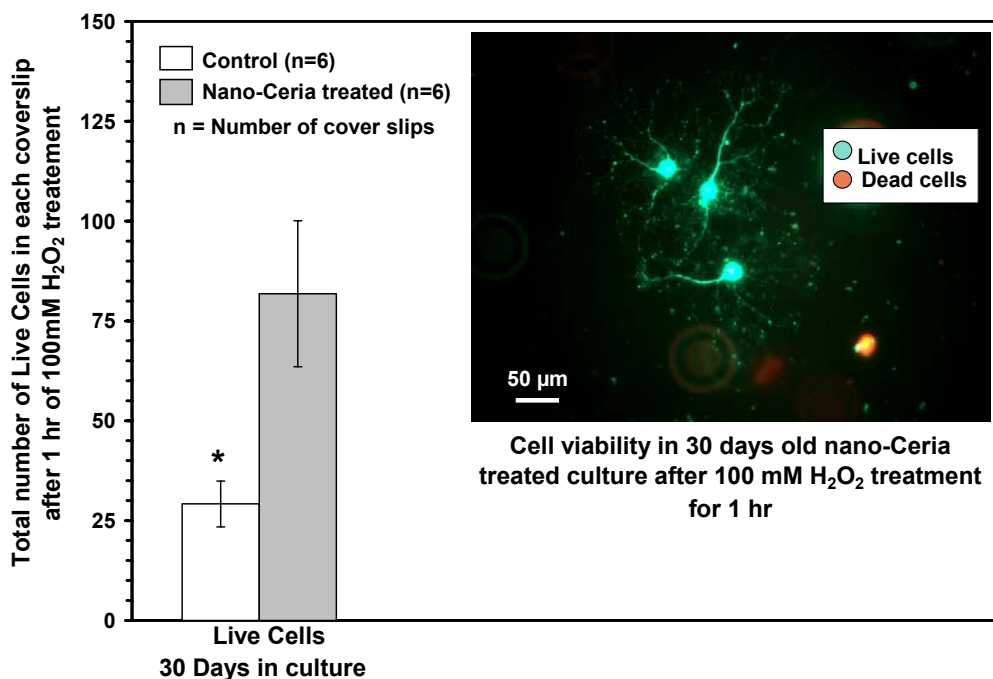


Figure 5.9. Live-dead cell assay after hydrogen peroxide treatment indicated that Cerium oxide treated cultures had significantly higher number of surviving cells as compared to the control (\*p < 0.05; \*\*p < 0.01)

indicates that cerium oxide nanoparticles treated cultures have significantly higher peroxide detoxification ability.

### 5.4.3. Discussion

In cerium oxide nanoparticles treated cultures, a significant rise in neuron survival as compared to the control culture was observed, which were supplemented only with B27. The antioxidant properties of the cerium oxide nanoparticles in culture may explain the significant neuroprotective effect seen in the nanoparticles treated culture. The regenerative property of the cerium oxide nanoparticles could explain the efficiency of a single dose of nanoparticles to provide a significantly high neuroprotective effect. Based

on the cell culture assays and hydrogen peroxide-induced oxidative injury assay, we conclude that the supplementation of neuronal cultures with cerium oxide nanoparticles in addition to the existing anti-oxidant molecules present in the B27 supplement has a significant synergistic effect in neuronal survival. The use of cerium oxide nanoparticles with other antioxidants may prove beneficial for the *in vivo* repair of spinal cord neurons.

## **5.5. Neuroprotection in Retinal Cells**

This work was carried out with Dr. James F. McGinnis and his student at Dean A. McGee Eye Institute, Oklahoma. It has been presented as a poster at 2005 ARVO Annual Meeting held at Fort Lauderdale, Florida.

### **5.5.1. Introduction**

Relative to other organs of body, the nervous system may be especially vulnerable to ROS mediated injury due to a number of biochemical, physiological and anatomical characteristics of neurons: high rate of oxidative metabolic activity, high concentration of readily oxidizable polyunsaturated fatty acids in membranes, endogenous generation of ROS by specific neurochemical reactions, high ratio of cell surface area to volume ratio, neuroanatomical network vulnerable to disruption and nonreplicating character of neuronal cells<sup>185</sup>. The retina is a part of the CNS and its injury from ROS has been implicated in several ophthalmologic diseases<sup>186,187</sup>. It is a tissue that also generates a lot of ROS which are involved in light-induced retina degeneration and age-related macular degeneration (AMD)<sup>188</sup>.

In this report, we tested the hypothesis that cerium oxide nanoparticles could promote the lifespan of retinal neurons in culture and protect them from apoptosis induced by  $H_2O_2$  *in vitro* by decreasing generation of intracellular reactive oxygen species.

### **5.5.2. Experimental Results and Discussion**

Retinae of Sprague-Dawley albino rat pups (0-2 day old) were dissected out and mechanically dissociated in 25 ml of DMEM/F12 medium. After filtered through 230  $\mu m$  and 140  $\mu m$  sieves, the dissociated cells were centrifuged at 1200 rpm for 5 min. The cell pellet were resuspended in the medium to  $10^5$  cells/ml. 1 ml of the cell suspension was plated in each well pre-treated with 10  $\mu g/ml$  of poly-D-lysine. The cells were maintained in the medium till day 7, when different concentrations of cerium oxide nanoparticles were added to the cultures. Apoptotic neurons were determined using flow cytometry (Beckman Coulter) at different time intervals.

Figure 5.10 shows the apoptotic retinal neurons in culture with/without 5nM cerium oxide nanoparticles treatment at time intervals of day 14, 19, 24 and 29. Statistical analysis was carried out using the Student t-test and shown as  $M \pm SD$  ( $n = 3$ ). The results clearly indicate that cerium oxide nanoparticles promote the longevity of retinal neurons *in vitro*.

The retinal neurons treated with 5 nM cerium oxide nanoparticles on day 7 were treated with 100  $\mu M$   $H_2O_2$  solution to test whether cerium oxide nanoparticles treatment inhibit the apoptosis of the neurons induced by  $H_2O_2$ . Figure 5.11 shows relative viable retinal neurons with/without incubation cerium oxide nanoparticles treatment for different time intervals. It shows that cerium oxide nanoparticles inhibit  $H_2O_2$  induced apoptosis of

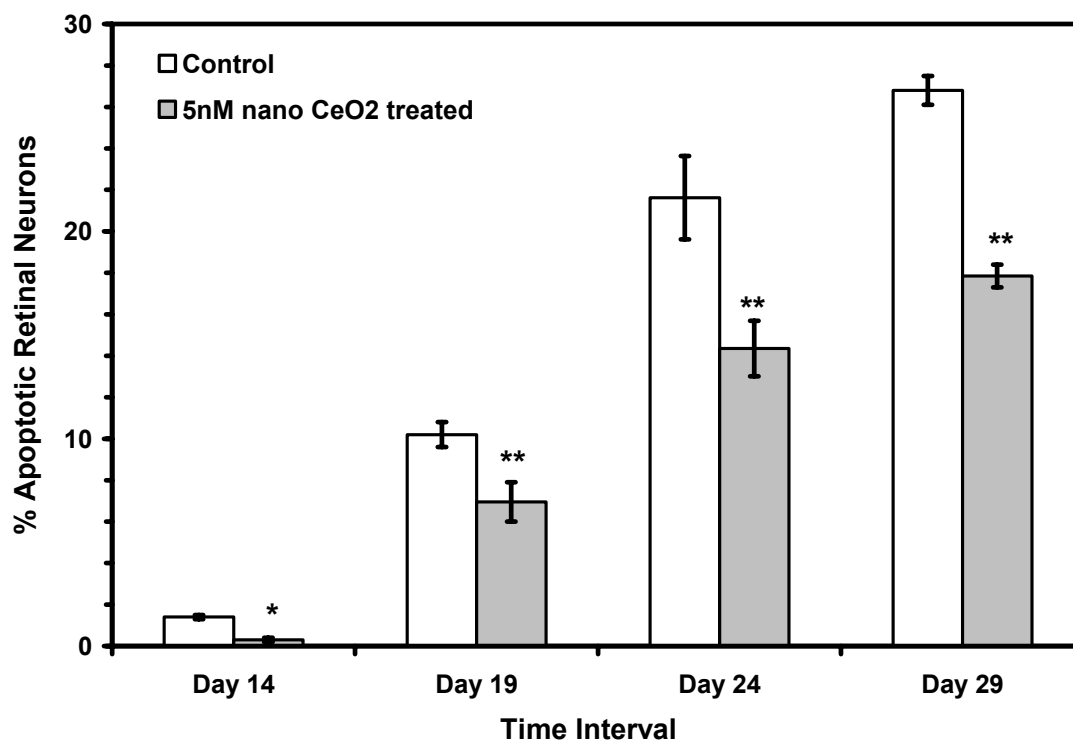


Figure 5.10. Percentage of apoptotic retinal neurons in culture with/without 5nM CeO<sub>2</sub> nanoparticle treatment at different time intervals (n=3, \*p < 0.05, \*\*p < 0.01)

retinal neurons *in vitro* in a time dependent manner. As incubation time increased, the protective effect from the nanoparticles was more significantly increased.

Intracellular reactive oxygen species (ROS) production was measured in both CeO<sub>2</sub> nanoparticle treated and control cells using 29,79-dichlorofluorescein diacetate (DCFH-DA, Sigma). The cells were incubated for different time intervals after 5 nM cerium oxide nanoparticles treatment at day 7. After the incubation time, the cells were first treated with 10 μM DCFH-DA (dissolved in DMSO) and then with 1mM H<sub>2</sub>O<sub>2</sub> at 37°C for 30 min after the excess DCFH-DA was washed with phosphate buffer solution. The data shown in Figure 5.12 indicates that the ROS generated in the cerium oxide nanoparticles

treated cells was statistically significantly less than the group without treatment as early as 12 hrs. This proves the hypothesis that cerium oxide nanoparticles treatment decreases the intracellular level of ROS of the retinal neurons.

In summary, cerium oxide nanoparticles promote longevity of retinal neurons *in vitro* and inhibit apoptosis induced by H<sub>2</sub>O<sub>2</sub> in a time dependent manner. The ROS generation is also decreased in a time dependent manner with the nanoparticles treatment.

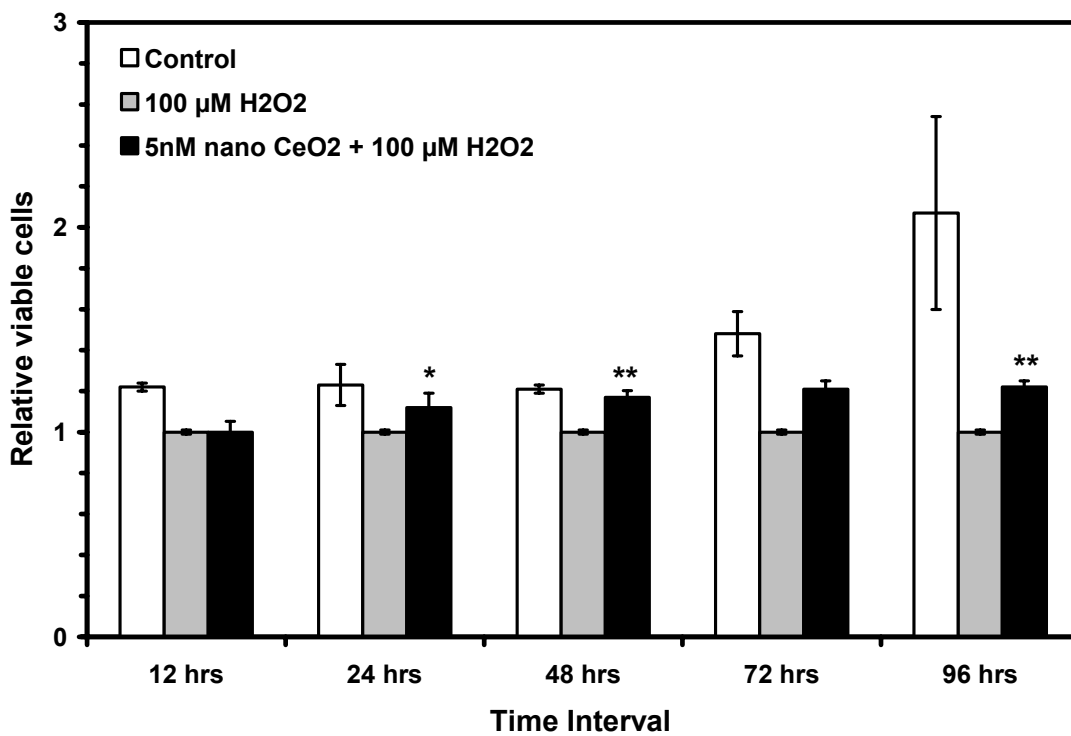


Figure 5.11. Relative viable retinal neurons with/without 5nM CeO<sub>2</sub> nanoparticle treatment at different time intervals for H<sub>2</sub>O<sub>2</sub> induced apoptosis, studied using flow cytometry (n=3, \*p < 0.05, \*\*p < 0.01)

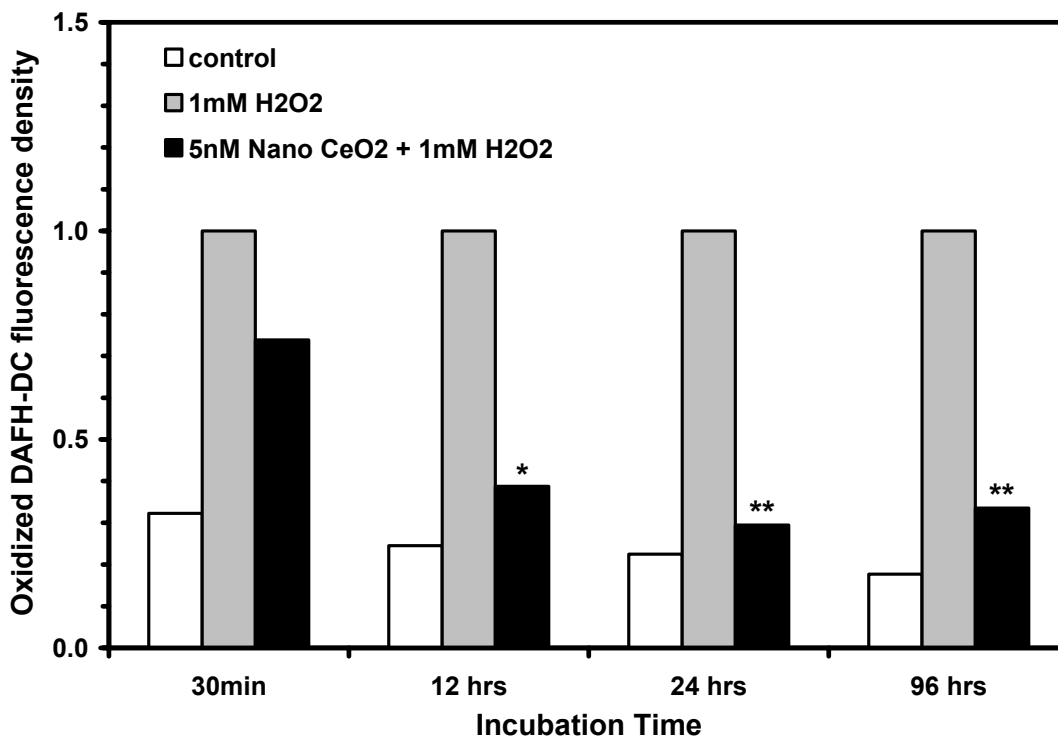


Figure 5.12. ROS generation in retinal neurons with/without 5nM CeO<sub>2</sub> nanoparticle treatment at different time intervals studied via oxidized DAFH-DC fluorescence density (n=3, \*p < 0.05, \*\*p < 0.01)

### 5.6. Role of Cerium Oxide Nanoparticles in Radical Induced Cellular Damage Protection

Based on our earlier experiments on organotypic mixed brain cell cultures of neonatal rats, it was hypothesized that cerium oxide nanoparticles act as a free radical scavenger to decrease the ROS-mediated cellular damage and increase cell survival *in vitro*. All the experiments presented in this chapter, radioprotection to normal cells, UV protection to Keratinocyte cells and neuroprotection to spinal cord neurons or retinal neurons, were also related to ROS mediated damage. As cerium oxide nanoparticles induce protection to cells *in vitro* in all these applications, the role of cerium oxide nanoparticles

in all these must be of reducing the cellular damages by acting as a free radical scavenger.

It has been found that nanocrystalline cerium oxide particles consist of mixed oxidation state i.e.  $Ce^{3+}$  and  $Ce^{4+}$ <sup>14,66</sup>. Additionally, this oxidation state of cerium can flip-flop between these two states very easily under different physicochemical states. We propose that cerium oxide nanoparticles act as free radical scavenger by switching between the +3 and +4 valence states via various surface chemical reactions. The radical scavenging mechanism can be given by a set of chemical reactions as follows.



Some preliminary studies also suggest that cerium oxide nanoparticles catalyze the same chemical reactions that SOD catalyzes *in vivo*.

Additionally, cerium oxide has the regenerative property which has been studied using UV visible spectroscopy as discussed in section 4.4.3. This regenerative property makes cerium oxide nanoparticles a very attractive proposition to treat ROS mediated cellular damages and diseases, as most of the present free radical scavengers do not have such property and need a repetitive dosage.

We believe that perhaps there is an auto-regenerative reaction cycle ( $Ce^{3+} \leftrightarrow Ce^{4+}$ ) continuing on the surface of cerium oxide nanoparticles and this may be the mechanism



by which it provides the material with an unprecedented antioxidant activity. The auto-regenerative antioxidant property of these nanoparticles appears to be a key component in all the biological applications discussed in the present chapter.

## CHAPTER 6. CONCLUSIONS

### 6.1. Fundamental Studies of Cerium Oxide Nanoparticles

- Cerium oxide nanoparticles with different size as well as doped with La/Nd were successfully synthesized using microemulsion process
- XRD studies showed increase in the lattice parameter with decrease in the particle size and increase in dopant concentration
- Raman allowed spectra shifted gradually to the lower energies and became broader and asymmetric (to lower energy side) due to decrease in the particle size of cerium oxide nanoparticles or increase in the dopant concentration
- Spatial correlation model developed to fit the experimental Raman spectra indicated increase in oxygen vacancies concentration as a function of decreasing particle size and increasing dopant concentration

### 6.2. Cerium Oxide Nanoparticles Based Biosensor of H<sub>2</sub>O<sub>2</sub>

- A 3-terminal amperometric electrochemical biosensor based on cerium oxide nanoparticles was developed for detection of H<sub>2</sub>O<sub>2</sub>
- The sensor was useful to detect H<sub>2</sub>O<sub>2</sub> in both, micromolar and minimolar ranges, with a response time of less than 1 min and preliminary studies on tomato stem and leaf extracts indicated the utility of the sensor in plant physiology studies

- The cerium oxide nanoparticles based biosensor was very stable and has a regenerative property which prolongs the shelf life of the sensor

### **6.3. Biological Applications of Cerium Oxide Nanoparticles**

- Nanomolar concentrations of cerium oxide nanoparticles is not toxic *in vitro* and reduce *in vitro* cellular damages induced by ROS
- Cerium oxide nanoparticles give radioprotection to breast epithelial cells while it does not protect the breast carcinoma cells. The selective protection by ceria nanoparticles can be useful in radiotherapy for cancer treatment to protect normal cells from radiation induced damages
- UV-induced damages to human Keratinocyte cells were decreased by cerium oxide nanoparticles treatment
- Also cerium oxide nanoparticles were found to be neuroprotective to adult rat spinal cord and rat retinal neurons
- Cerium oxide nanoparticles act as a free radical scavenger with an auto-regenerative property to reduce the cellular damages induced by ROS

## REFERENCES

- <sup>1</sup> R. Feynman, "There's plenty of room at the bottom," *Engineering and Science* **23**, 22-36 (1960).
- <sup>2</sup> B. Bharat, *Springer Handbook of Nanotechnology*. (Springer-Verlag, Heidelberg, Germany, 2004).
- <sup>3</sup> R. W. Whatmore and J. Corbett, "Nanotechnology in the Marketplace," *Computing & Control Engineering Journal* **6** (3), 106-107 (1995).
- <sup>4</sup> W.-x. Zhang, C.-B. Wang, and H.-L. Lien, "Treatment of chlorinated organic contaminants with nanoscale bimetallic particles," *Catalysis Today* **40** (4), 387-395 (1998).
- <sup>5</sup> W. C. W. Chan, D. J. Maxwell, Gao, Xiaohu, R. E. Bailey, Han, Mingyong, and S. Nie, "Luminescent quantum dots for multiplexed biological detection and imaging," *Current Opinion in Biotechnology* **13** (1), 40-46 (2002).
- <sup>6</sup> P. Brousseau and C. J. Anderson, "Nanometric aluminum in explosives," *Propellants Explosives Pyrotechnics* **27** (5), 300-306 (2002).
- <sup>7</sup> J. B. Hedrick, in *Minerals Yearbook* (US Geological Survey, Reston, VA, 1998), Vol. I, pp. 61.01-61.14.
- <sup>8</sup> T. Suzuki, I. Kosacki, H. U. Anderson, and P. Colomban, "Electrical conductivity and lattice defects in nanocrystalline cerium oxide thin films," *Journal of the American Ceramic Society* **84** (9), 2007-2014 (2001).
- <sup>9</sup> G. S. Herman, "Characterization of surface defects on epitaxial CeO<sub>2</sub>(001) films," *Surface Science* **437** (1-2), 207-214 (1999).
- <sup>10</sup> J. C. Conesa, "Computer Modeling of Surfaces and Defects on Cerium Dioxide," *Surface Science* **339** (3), 337-352 (1995).
- <sup>11</sup> P. L. Land, "Defect Equilibria for Extended Point-Defects, with Application to Nonstoichiometric Ceria," *Journal of Physics and Chemistry of Solids* **34** (11), 1839-1845 (1973).
- <sup>12</sup> E. Mamontov, T. Egami, R. Brezny, M. Koranne, and S. Tyagi, "Lattice defects and oxygen storage capacity of nanocrystalline ceria and ceria-zirconia," *Journal of Physical Chemistry B* **104** (47), 11110-11116 (2000).
- <sup>13</sup> C. Heinemann, H. H. Cornehl, D. Schroder, M. Dolg, and H. Schwarz, "The CeO<sub>2</sub><sup>+</sup> cation: Gas-phase reactivity and electronic structure," *Inorganic Chemistry* **35** (9), 2463-2475 (1996).
- <sup>14</sup> S. Patil, University of Central Florida, 2003.
- <sup>15</sup> R. Uyeda, "Morphology of Fine Metal Crystallites," *Journal of Crystal Growth* **24** (OCT), 69-75 (1974).
- <sup>16</sup> Y. Liu, Q. L. Zhang, F. K. Tittel, R. F. Curl, and R. E. Smalley, "Photodetachment and Photofragmentation Studies of Semiconductor Cluster Anions," *Journal of Chemical Physics* **85** (12), 7434-7441 (1986).

- <sup>17</sup> M. D. Morse, "Clusters of Transition-Metal Atoms," *Chemical Reviews* **86** (6), 1049-1109 (1986).
- <sup>18</sup> K. Laihing, R. G. Wheeler, W. L. Wilson, and M. A. Duncan, "Photoionization Dynamics and Abundance Patterns in Laser Vaporized Tin and Lead Clusters," *Journal of Chemical Physics* **87** (6), 3401-3409 (1987).
- <sup>19</sup> W. R. Cannon, S. C. Danforth, J. H. Flint, J. S. Haggerty, and R. A. Marra, "Sinterable Ceramic Powders from Laser-Driven Reactions .1. Process Description and Modeling," *Journal of the American Ceramic Society* **65** (7), 324-330 (1982).
- <sup>20</sup> P. Fayet and L. Woste, "Experiments on Size-Selected Metal Cluster Ions in a Triple Quadrupole Arrangement," *Zeitschrift Fur Physik D-Atoms Molecules and Clusters* **3** (2-3), 177-182 (1986).
- <sup>21</sup> R. B. Wright, J. K. Bates, and D. M. Gruen, "Matrix-Isolation Spectroscopy of Aluminum, Copper, and Nickel Hydrides and Deuterides Produced in a Hollow-Cathode Discharge," *Inorganic Chemistry* **17** (8), 2274-2278 (1978).
- <sup>22</sup> M. L. Mandich, V. E. Bondybey, and W. D. Reents, "Reactive Etching of Positive and Negative Silicon Cluster Ions by Nitrogen-Dioxide," *Journal of Chemical Physics* **86** (7), 4245-4257 (1987).
- <sup>23</sup> T. Takagi, "Ionized Cluster Beam Technique for Thin-Film Deposition," *Zeitschrift Fur Physik D-Atoms Molecules and Clusters* **3** (2-3), 271-278 (1986).
- <sup>24</sup> E. Matijevic, "Monodispersed Colloids - Art and Science," *Langmuir* **2** (1), 12-20 (1986).
- <sup>25</sup> T. Sugimoto, "Preparation of Monodispersed Colloidal Particles," *Advances in Colloid and Interface Science* **28** (1), 65-108 (1987).
- <sup>26</sup> M. Kagawa, M. Kikuchi, R. Ohno, and T. Nagae, "Preparation of Ultrafine Mgo by the Spray-Icp Technique," *Journal of the American Ceramic Society* **64** (1), C7-C8 (1981).
- <sup>27</sup> B. H. Robinson, "Colloid Chemistry - Applications of Microemulsions," *Nature* **320** (6060), 309-309 (1986).
- <sup>28</sup> M. A. Lopezquintela and J. Rivas, "Chemical-Reactions in Microemulsions - a Powerful Method to Obtain Ultrafine Particles," *Journal of Colloid and Interface Science* **158** (2), 446-451 (1993).
- <sup>29</sup> M. Boutonnet, J. Kizling, and P. Stenius, "The Preparation of Monodisperse Colloidal Metal Particles from Micro-Emulsions," *Colloids and Surfaces* **5** (3), 209-225 (1982).
- <sup>30</sup> S. P. Moulik and B. K. Paul, "Structure, dynamics and transport properties of microemulsions," *Advances in Colloid and Interface Science* **78** (2), 99-195 (1998).
- <sup>31</sup> E. Ruckenstein, "Thermodynamic approaches to microemulsions," *Journal of Colloid and Interface Science* **204** (1), 143-150 (1998).
- <sup>32</sup> S. Santra, P. Zhang, K. M. Wang, R. Tapeç, and W. H. Tan, "Conjugation of biomolecules with luminophore-doped silica nanoparticles for photostable biomarkers," *Analytical Chemistry* **73** (20), 4988-4993 (2001).
- <sup>33</sup> S. Santra, K. M. Wang, R. Tapeç, and W. H. Tan, "Development of novel dye-doped silica nanoparticles for biomarker application," *Journal of Biomedical Optics* **6** (2), 160-166 (2001).

- <sup>34</sup> S. Santra, Tapeç, R., N. Theodoropoulou, Dobson, J., A. Hebard, and W. H. Tan, "Synthesis and characterization of silica-coated iron oxide nanoparticles in microemulsion: The effect of nonionic surfactants," *Langmuir* **17** (10), 2900-2906 (2001).
- <sup>35</sup> F. J. Arriagada and K. Osseo-Asare, "Synthesis of nanosize silica in a nonionic water-in-oil microemulsion: Effects of the water/surfactant molar ratio and ammonia concentration," *Journal of Colloid and Interface Science* **211** (2), 210-220 (1999).
- <sup>36</sup> H. Yang and P. H. Holloway, "Enhanced photoluminescence from CdS : Mn/ZnS core/shell quantum dots," *Applied Physics Letters* **82** (12), 1965-1967 (2003).
- <sup>37</sup> M. Qhobosheane, S. Santra, P. Zhang, and W. H. Tan, "Biochemically functionalized silica nanoparticles," *Analyst* **126** (8), 1274-1278 (2001).
- <sup>38</sup> C. H. Chew, L. M. Gan, and D. O. Shah, "The Effect of Alkanes on the Formation of Ultrafine Silver Bromide Particles in Ionic W/O Microemulsions," *Journal of Dispersion Science and Technology* **11** (6), 593-609 (1990).
- <sup>39</sup> M. J. Hou, M. Kim, and D. O. Shah, "A Light-Scattering Study on the Droplet Size and Interdroplet Interaction in Microemulsions of Aot-Oil-Water System," *Journal of Colloid and Interface Science* **123** (2), 398-412 (1988).
- <sup>40</sup> U. Natarajan, K. Handique, A. Mehra, J. R. Bellare, and K. C. Khilar, "Ultrafine metal particle formation in reverse micellar systems: Effects of intermicellar exchange on the formation of particles," *Langmuir* **12** (11), 2670-2678 (1996).
- <sup>41</sup> R. Bandyopadhyaya, R. Kumar, K. S. Gandhi, and D. Ramkrishna, "Modeling of precipitation in reverse micellar systems," *Langmuir* **13** (14), 3610-3620 (1997).
- <sup>42</sup> C. Tojo, M. C. Blanco, and M. A. Lopez-Quintela, "Microemulsions as microreactors: a Monte Carlo simulation on the synthesis of particles," *Journal of Non-Crystalline Solids* **235**, 688-691 (1998).
- <sup>43</sup> C. Tojo, M. C. Blanco, F. Rivadulla, and M. A. Lopez-Quintela, "Kinetics of the formation of particles in microemulsions," *Langmuir* **13** (7), 1970-1977 (1997).
- <sup>44</sup> Z. H. Wu, R. E. Benfield, Guo, L., H. J. Li, Yang, Q. L., D. Grandjean, Li, Q. S., and H. S. Zhu, "Cerium oxide nanoparticles coated by surfactant sodium bis(2-ethylhexyl) sulphosuccinate (AOT): local atomic structures and X-ray absorption spectroscopic studies," *Journal of Physics-Condensed Matter* **13** (22), 5269-5283 (2001).
- <sup>45</sup> J. B. Nagy, in *Handbook of Microemulsion Science and Technology*, edited by P. Kumar and K. L. Mittal (Marcel Dekker, New York, 1999), p. 499.
- <sup>46</sup> T. Masui, H. Hirai, Imanaka, N., G. Adachi, Sakata, T., and H. Mori, "Synthesis of cerium oxide nanoparticles by hydrothermal crystallization with citric acid," *Journal of Materials Science Letters* **21** (6), 489-491 (2002).
- <sup>47</sup> F. Czerwinski and J. A. Szpunar, "The nanocrystalline ceria sol-gel coatings for high temperature applications," *Journal of Sol-Gel Science and Technology* **9** (1), 103-114 (1997).
- <sup>48</sup> R. D. Falcone, N. M. Correa, M. A. Biasutti, and J. J. Silber, "Properties of AOT aqueous and nonaqueous microemulsions sensed by optical molecular probes," *Langmuir* **16** (7), 3070-3076 (2000).

- 49 B. Tamamushi and N. Watanabe, "The Formation of Molecular Aggregation Structures in Ternary-System - Aerosol Ot-Water-Iso-Octane," *Colloid and Polymer Science* **258** (2), 174-178 (1980).
- 50 T. K. De and A. Maitra, "Solution Behavior of Aerosol Ot in Nonpolar-Solvents," *Advances in Colloid and Interface Science* **59**, 95-193 (1995).
- 51 T. Kawai, Y. Usui, and K. Kon-No, "Synthesis and growth mechanism of GeO<sub>2</sub> particles in AOT reversed micelles," *Colloids and Surfaces a-Physicochemical and Engineering Aspects* **149** (1-3), 39-47 (1999).
- 52 K. C. Song and J. H. Kim, "Synthesis of high surface area tin oxide powders via water-in-oil microemulsions," *Powder Technology* **107** (3), 268-272 (2000).
- 53 A. P. Herrera, O. Resto, J. G. Briano, and C. Rinaldi, "Synthesis and agglomeration of gold nanoparticles in reverse micelles," *Nanotechnology* **16** (7), S618-S625 (2005).
- 54 I. Lisiecki and M. P. Pileni, "Copper Metallic Particles Synthesized in-Situ in Reverse Micelles - Influence of Various Parameters on the Size of the Particles," *Journal of Physical Chemistry* **99** (14), 5077-5082 (1995).
- 55 G. Cassin, J. P. Badiali, and M. P. Pileni, "Aot Reverse Micelles - Depletion Model," *Journal of Physical Chemistry* **99** (34), 12941-12946 (1995).
- 56 M. Kotlarchyk, J. S. Huang, and S. H. Chen, "Structure of Aot-Reversed Micelles Determined by Small-Angle Neutron-Scattering," *Journal of Physical Chemistry* **89** (20), 4382-4386 (1985).
- 57 H. B. Bohidar and M. Behboudnia, "Characterization of reverse micelles by dynamic light scattering," *Colloids and Surfaces A: Physicochemical and Engineering Aspects* **178** (1-3), 313-323 (2001).
- 58 T. Masui, T. Ozaki, K. Machida, and G. Adachi, "Preparation of ceria-zirconia sub-catalysts for automotive exhaust cleaning," *Journal of Alloys and Compounds* **303**, 49-55 (2000).
- 59 I. Kosacki and H. U. Anderson, in *Encyclopedia of Materials: Science and Technology*, edited by K. H. J. Buschow, M. C. F. Robert W. Cahn, Bernard Ilshner, Edward J. Kramer, and S. Mahajan (Elsevier, Oxford, 2001), pp. 3609-3617.
- 60 H. Gleiter, "Nanocrystalline Materials," *Progress in Materials Science* **33** (4), 223-315 (1989).
- 61 A. Yokozeki and G. D. Stein, "Metal Cluster Generator for Gas-Phase Electron-Diffraction and Its Application to Bismuth, Lead, and Indium - Variation in Microcrystal Structure with Size," *Journal of Applied Physics* **49** (4), 2224-2232 (1978).
- 62 G. Schmid, "Metal-Clusters and Cluster Metals," *Polyhedron* **7** (22-23), 2321-2329 (1988).
- 63 D. L. LesliePelecky and R. D. Rieke, "Magnetic properties of nanostructured materials," *Chemistry of Materials* **8** (8), 1770-1783 (1996).
- 64 Y. M. Chiang, E. B. Lavik, I. Kosacki, H. L. Tuller, and J. Y. Ying, "Defect and transport properties of nanocrystalline CeO<sub>2-x</sub>," *Applied Physics Letters* **69** (2), 185-187 (1996).
- 65 F. Czerwinski and W. W. Smeltzer, "The Early-Stage Oxidation-Kinetics of Ceo<sub>2</sub> Sol-Coated Nickel," *Journal of the Electrochemical Society* **140** (9), 2606-2615 (1993).

- <sup>66</sup> S. Patil, S. C. Kuiry, and S. Seal, "Nanocrystalline ceria imparts better high-temperature protection," *Proceedings of the Royal Society of London Series A-Mathematical Physical and Engineering Sciences* **460** (2052), 3569-3587 (2004).
- <sup>67</sup> W. H. Weber, K. C. Hass, and J. R. McBride, "Raman-Study of CeO<sub>2</sub> - 2nd-Order Scattering, Lattice-Dynamics, and Particle-Size Effects," *Physical Review B* **48** (1), 178-185 (1993).
- <sup>68</sup> T. Sakurai and T. Sato, "Temperature Dependence of Vibrational Spectra in Calcite by Means of Emissivity Measurement," *Physical Review B* **4** (2), 583-591 (1971).
- <sup>69</sup> S. Kanakaraju, S. Mohan, and A. K. Sood, "Optical and structural properties of reactive ion beam sputter deposited CeO<sub>2</sub> films," *Thin Solid Films* **305** (1-2), 191-195 (1997).
- <sup>70</sup> M. Fujii, S. Hayashi, and K. Yamamoto, "Raman-Scattering from Quantum Dots of Ge Embedded in SiO<sub>2</sub> Thin-Films," *Applied Physics Letters* **57** (25), 2692-2694 (1990).
- <sup>71</sup> P. Parayanthal and F. H. Pollak, "Raman-Scattering in Alloy Semiconductors - Spatial Correlation Model," *Physical Review Letters* **52** (20), 1822-1825 (1984).
- <sup>72</sup> H. Richter, Z. P. Wang, and L. Ley, "The One Phonon Raman-Spectrum in Microcrystalline Silicon," *Solid State Communications* **39** (5), 625-629 (1981).
- <sup>73</sup> J. E. Spanier, R. D. Robinson, F. Zheng, S. W. Chan, and I. P. Herman, "Size-dependent properties of CeO<sub>2</sub>-y nanoparticles as studied by Raman scattering," *Physical Review B* **64** (24) (2001).
- <sup>74</sup> P. Parayanthal and F. H. Pollak, "Raman scattering in alloy semiconductors: 'spatial correlation' model," *Physical Review Letters* **52** (20), 1822-1825 (1984).
- <sup>75</sup> I. Kosacki, T. Suzuki, H. U. Anderson, and P. Colomban, "Raman scattering and lattice defects in nanocrystalline CeO<sub>2</sub> thin films," *Solid State Ionics* **149** (1-2), 99-105 (2002).
- <sup>76</sup> J. R. McBride, K. C. Hass, B. D. Poindexter, and W. H. Weber, "Raman and X-Ray Studies of Ce<sub>1-x</sub>Re<sub>x</sub>O<sub>2-y</sub>, Where Re=La, Pr, Nd, Eu, Gd, and Tb," *Journal of Applied Physics* **76** (4), 2435-2441 (1994).
- <sup>77</sup> M. C. Daniel and D. Astruc, "Gold nanoparticles: Assembly, supramolecular chemistry, quantum-size-related properties, and applications toward biology, catalysis, and nanotechnology," *Chemical Reviews* **104** (1), 293-346 (2004).
- <sup>78</sup> A. N. Shipway, E. Katz, and I. Willner, "Nanoparticle arrays on surfaces for electronic, optical, and sensor applications," *Chemphyschem* **1** (1), 18-52 (2000).
- <sup>79</sup> T. Trindade, P. O'Brien, and N. L. Pickett, "Nanocrystalline semiconductors: Synthesis, properties, and perspectives," *Chemistry of Materials* **13** (11), 3843-3858 (2001).
- <sup>80</sup> P. Schwerdtfeger, "Gold goes nano - From small clusters to low-dimensional assemblies," *Angewandte Chemie-International Edition* **42** (17), 1892-1895 (2003).
- <sup>81</sup> R. Gangopadhyay and A. De, "Conducting polymer nanocomposites: A brief overview," *Chemistry of Materials* **12** (3), 608-622 (2000).
- <sup>82</sup> I. Fridovich, "Biology of Oxygen Radicals," *Science* **201** (4359), 875-880 (1978).
- <sup>83</sup> B. Halliwell and J. M. C. Gutteridge, *Free Radicals in Biology and Medicine*, 3rd ed. (Oxford University Press, New York, 1999), p.936.



- <sup>84</sup> A. Boveris, B. Chance, and N. Oshino, "Cellular Production of Hydrogen-Peroxide," *Biochemical Journal* **128** (3), 617-630 (1972).
- <sup>85</sup> I. Fridovich, "Superoxide Radical - an Endogenous Toxicant," *Annual Review of Pharmacology and Toxicology* **23**, 239-257 (1983).
- <sup>86</sup> H. J. H. Fenton, "Oxidation of tartaric acid in the presence of iron.," *Journal of the Chemical Society, Transactions* **65**, 899-910 (1894).
- <sup>87</sup> F. Haber and J. Weiss, "The Catalytic Decomposition of Hydrogen Peroxide by Iron Salts," *Proceedings of the Royal Society of London. Series A, Mathematical and Physical Sciences* **147** (861), 332-351 (1934).
- <sup>88</sup> T. Gechev and J. Hille, "Hydrogen peroxide as a signal controlling plant programmed cell death," *The Journal of Cell Biology* **168** (1), 17-20 (2005).
- <sup>89</sup> K. Apel and H. Hirt, "Reactive oxygen species: Metabolism, oxidative stress, and signal transduction," *Annual Review of Plant Biology* **55**, 373-399 (2004).
- <sup>90</sup> H. P. Bais, R. Vepachedu, S. Gilroy, R. M. Callaway, and J. M. Vivanco, "Allelopathy and exotic plant invasion: From molecules and genes to species interactions," *Science* **301** (5638), 1377-1380 (2003).
- <sup>91</sup> T. Gechev, I. Gadjev, F. Van Breusegem, D. Inze, S. Dukiandjiev, V. Toneva, and I. Minkov, "Hydrogen peroxide protects tobacco from oxidative stress by inducing a set of antioxidant enzymes," *Cellular and Molecular Life Sciences* **59** (4), 708-714 (2002).
- <sup>92</sup> E. C. Hurdis and H. Romeyn Jr., "Accuracy of determination of hydrogen peroxide by cerate oxidimetry," *Analytical Chemistry* **26**, 320-325 (1954).
- <sup>93</sup> C. Matsubara, N. Kawamoto, and K. Takamura, "Oxo 5,10,15,20-Tetra(4-Pyridyl)Porphyrinato Titanium(Iv) - an Ultra-High Sensitivity Spectrophotometric Reagent for Hydrogen-Peroxide," *Analyst* **117** (11), 1781-1784 (1992).
- <sup>94</sup> M. G. Garguilo, N. Huynh, A. Proctor, and A. C. Michael, "Amperometric Sensors for Peroxide, Choline, and Acetylcholine Based on Electron-Transfer between Horseradish-Peroxidase and a Redox Polymer," *Analytical Chemistry* **65** (5), 523-528 (1993).
- <sup>95</sup> A. Boveris, "Determination of the Production of Superoxide Radicals and Hydrogen-Peroxide in Mitochondria," *Methods in Enzymology* **105**, 429-435 (1984).
- <sup>96</sup> A. Boveris, E. Martino, and A. O. M. Stoppani, "Evaluation of Horseradish Peroxidase-Scopoletin Method for Measurement of Hydrogen-Peroxide Formation in Biological-Systems," *Analytical Biochemistry* **80** (1), 145-158 (1977).
- <sup>97</sup> P. C. Hinkle, R. A. Butow, E. Racker, and B. Chance, "Partial Resolution of Enzymes Catalyzing Oxidative Phosphorylation .15. Reverse Electron Transfer in Flavin-Cytochrome B Region of Respiratory Chain of Beef Heart Submitochondrial Particles," *Journal of Biological Chemistry* **242** (22), 5169-5173 (1967).
- <sup>98</sup> P. A. Hyslop and L. A. Sklar, "A Quantitative Fluorimetric Assay for the Determination of Oxidant Production by Polymorphonuclear Leukocytes - Its Use in the Simultaneous Fluorimetric Assay of Cellular Activation Processes," *Analytical Biochemistry* **141** (1), 280-286 (1984).

- <sup>99</sup> W. Ruch, P. H. Cooper, and M. Baggiolini, "Assay of H<sub>2</sub>O<sub>2</sub> Production by Macrophages and Neutrophils with Homovanillic-Acid and Horseradish-Peroxidase," *Journal of Immunological Methods* **63** (3), 347-357 (1983).
- <sup>100</sup> G. Cohen, M. Kim, and V. Ogwu, "A modified catalase assay suitable for a plate reader and for the analysis of brain cell cultures," *Journal of Neuroscience Methods* **67** (1), 53-56 (1996).
- <sup>101</sup> K. Staniek and H. Nohl, "H<sub>2</sub>O<sub>2</sub> detection from intact mitochondria as a measure for one-electron reduction of dioxygen requires a non-invasive assay system," *Biochimica Et Biophysica Acta-Bioenergetics* **1413** (2), 70-80 (1999).
- <sup>102</sup> E. Pick and Y. Keisari, "A Simple Colorimetric Method for the Measurement of Hydrogen-Peroxide Produced by Cells in Culture," *Journal of Immunological Methods* **38** (1-2), 161-170 (1980).
- <sup>103</sup> A. S. Keston and R. Brandt, "Fluorometric Analysis of Ultramicro Quantities of Hydrogen Peroxide," *Analytical Biochemistry* **11** (1), 1-5 (1965).
- <sup>104</sup> B. Paul and A. J. Sbarra, "Role of Phagocyte in Host-Parasite Interactions .13. Direct Quantitative Estimation of H<sub>2</sub>O<sub>2</sub> in Phagocytizing Cells," *Biochimica Et Biophysica Acta* **156** (1), 168-178 (1968).
- <sup>105</sup> D. A. Bass, J. W. Parce, L. R. Dechatelet, P. Szejda, M. C. Seeds, and M. Thomas, "Flow Cytometric Studies of Oxidative Product Formation by Neutrophils - a Graded Response to Membrane Stimulation," *Journal of Immunology* **130** (4), 1910-1917 (1983).
- <sup>106</sup> G. Rothe and G. Valet, "Flow Cytometric Analysis of Respiratory Burst Activity in Phagocytes with Hydroethidine and 2',7'-Dichlorofluorescein," *Journal of Leukocyte Biology* **47** (5), 440-448 (1990).
- <sup>107</sup> R. Cathcart, E. Schwiers, and B. N. Ames, "Detection of Picomole Levels of Hydroperoxides Using a Fluorescent Dichlorofluorescein Assay," *Analytical Biochemistry* **134** (1), 111-116 (1983).
- <sup>108</sup> C. P. Lebel, H. Ischiropoulos, and S. C. Bondy, "Evaluation of the Probe 2',7'-Dichlorofluorescein as an Indicator of Reactive Oxygen Species Formation and Oxidative Stress," *Chemical Research in Toxicology* **5** (2), 227-231 (1992).
- <sup>109</sup> L. N. Larsen, E. Dahl, and J. Bremer, "Peroxidative oxidation of leuco-dichlorofluorescein by prostaglandin H synthase in prostaglandin biosynthesis from polyunsaturated fatty acids," *Biochimica Et Biophysica Acta-Lipids and Lipid Metabolism* **1299** (1), 47-53 (1996).
- <sup>110</sup> C. Rota, C. F. Chignell, and R. P. Mason, "Evidence for free radical formation during the oxidation of 2'-7'-dichlorofluorescein to the fluorescent dye 2'-7'-dichlorofluorescein by horseradish peroxidase: Possible implications for oxidative stress measurements," *Free Radical Biology and Medicine* **27** (7-8), 873-881 (1999).
- <sup>111</sup> J. P. Crow, "Dichlorodihydrofluorescein and dihydrorhodamine 123 are sensitive indicators of peroxynitrite in vitro: Implications for intracellular measurement of reactive nitrogen and oxygen species," *Nitric Oxide-Biology and Chemistry* **1** (2), 145-157 (1997).
- <sup>112</sup> N. W. Kooy, J. A. Royall, and H. Ischiropoulos, "Oxidation of 2',7'-dichlorofluorescein by peroxynitrite," *Free Radical Research* **27** (3), 245-254 (1997).
- <sup>113</sup> L. M. Melnick, *Iron*. (Interscience Publishers, New York, NY, 1962), pp.247-310.
- <sup>114</sup> R. G. Thurman, R. Scholz, and H. G. Ley, "Hepatic Microsomal Ethanol Oxidation - Hydrogen-Peroxide Formation and Role of Catalase," *European Journal of Biochemistry* **25** (3), 420-430 (1972).

- <sup>115</sup> M. Shi, E. Gozal, H. A. Choy, and H. J. Forman, "Extracellular Glutathione and Gamma-Glutamyl-Transpeptidase Prevent H<sub>2</sub>O<sub>2</sub>-Induced Injury by 2,3-Dimethoxy-1,4-Naphthoquinone," *Free Radical Biology and Medicine* **15** (1), 57-67 (1993).
- <sup>116</sup> M. M. Tarpey, C. R. White, E. Suarez, G. Richardson, R. Radi, and B. A. Freeman, "Chemiluminescent detection of oxidants in vascular tissue - Lucigenin but not coelenterazine enhances superoxide formation," *Circulation Research* **84** (10), 1203-1211 (1999).
- <sup>117</sup> Y. Iwasaki and M. Morita, "Electrochemical measurements with interdigitated array microelectrodes," *Current Separations* **14** (1), 2-8 (1995).
- <sup>118</sup> J. E. Frew and H. A. Hill, "Electrochemical biosensors," *Analytical Chemistry* **59** (15), 933A-944A (1987).
- <sup>119</sup> R. K. Kobos, "Enzyme-based electrochemical biosensors," *TrAC Trends in Analytical Chemistry* **6** (1), 6-9 (1987).
- <sup>120</sup> S. B. Khoo and F. Chen, "Studies of sol-gel ceramic film incorporating methylene blue on glassy carbon: An electrocatalytic system for the simultaneous determination of ascorbic and uric acids," *Analytical Chemistry* **74** (22), 5734-5741 (2002).
- <sup>121</sup> Y. T. Kong, M. Boopathi, and Y. B. Shim, "Direct electrochemistry of horseradish peroxidase bonded on a conducting polymer modified glassy carbon electrode," *Biosensors & Bioelectronics* **19** (3), 227-232 (2003).
- <sup>122</sup> C. Kurzawa, A. Hengstenberg, and W. Schuhmann, "Immobilization method for the preparation of biosensors based on pH shift-induced deposition of biomolecule-containing polymer films," *Analytical Chemistry* **74** (2), 355-361 (2002).
- <sup>123</sup> C. M. Ruan, F. Yang, C. H. Lei, and J. Q. Deng, "Thionine covalently tethered to multilayer horseradish peroxidase in a self-assembled monolayer as an electron-transfer mediator," *Analytical Chemistry* **70** (9), 1721-1725 (1998).
- <sup>124</sup> P. N. Bartlett, P. R. Birkin, F. Palmisano, and G. DeBenedetto, "A study on the direct electrochemical communication between horseradish peroxidase and a poly(aniline) modified electrode," *Journal of the Chemical Society-Faraday Transactions* **92** (17), 3123-3130 (1996).
- <sup>125</sup> J. Wang, A. Ciszewski, and N. Naser, "Stripping Measurements of Hydrogen-Peroxide Based on Biocatalytic Accumulation at Mediatorless Peroxidase Carbon Paste Electrodes," *Electroanalysis* **4** (8), 777-782 (1992).
- <sup>126</sup> L. Gorton, G. Jonssonpettersson, E. Csoregi, K. Johansson, E. Dominguez, and G. Markovarga, "Amperometric Biosensors Based on an Apparent Direct Electron-Transfer between Electrodes and Immobilized Peroxidases - Plenary Lecture," *Analyst* **117** (8), 1235-1241 (1992).
- <sup>127</sup> T. Delumleywoodyear, P. Rocca, J. Lindsay, Y. Dror, A. Freeman, and A. A. Heller, "Polyacrylamide-Based Redox Polymer for Connecting Redox Centers of Enzymes to Electrodes," *Analytical Chemistry* **67** (8), 1332-1338 (1995).
- <sup>128</sup> W. O. Ho, D. Athey, C. J. McNeil, H. J. Hager, G. P. Evans, and W. H. Mullen, "Mediatorless Horseradish-Peroxidase Enzyme Electrodes Based on Activated Carbon - Potential Application to Specific Binding Assay," *Journal of Electroanalytical Chemistry* **351** (1-2), 185-197 (1993).
- <sup>129</sup> M. Vreeke, R. Maidan, and A. Heller, "Hydrogen-Peroxide and Beta-Nicotinamide Adenine-Dinucleotide Sensing Amperometric Electrodes Based on Electrical Connection of Horseradish-

- Peroxidase Redox Centers to Electrodes through a 3-Dimensional Electron Relaying Polymer Network," *Analytical Chemistry* **64** (24), 3084-3090 (1992).
- <sup>130</sup> U. Wollenberger, J. Wang, M. Ozsoz, E. Gonzalezromero, and F. Scheller, "Bulk Modified Enzyme Electrodes for Reagentless Detection of Peroxides," *Bioelectrochemistry and Bioenergetics* **26** (2), 287-296 (1991).
- <sup>131</sup> S.-Q. Liu and H.-X. Ju, "Renewable reagentless hydrogen peroxide sensor based on direct electron transfer of horseradish peroxidase immobilized on colloidal gold-modified electrode," *Analytical Biochemistry* **307** (1), 110-116 (2002).
- <sup>132</sup> S. L. Chut, J. Li, and S. N. Tan, "Reagentless amperometric determination of hydrogen peroxide by silica sol-gel modified biosensor," *Analyst* **122** (11), 1431-1434 (1997).
- <sup>133</sup> U. Wollenberger, V. Bogdanovskaya, S. Bobrin, F. Scheller, and M. Tarasevich, "Enzyme Electrodes Using Bioelectrocatalytic Reduction of Hydrogen-Peroxide," *Analytical Letters* **23** (10), 1795-1808 (1990).
- <sup>134</sup> V. J. Razumas, A. V. Gudavicius, and J. J. Kulys, "Redox Conversion of Peroxidase on Surface-Modified Gold Electrode," *Journal of Electroanalytical Chemistry* **151** (1-2), 311-315 (1983).
- <sup>135</sup> Y. Xiao, H. X. Ju, and H. Y. Chen, "Direct electrochemistry of horseradish peroxidase immobilized on a colloid/cysteamine-modified gold electrode," *Analytical Biochemistry* **278** (1), 22-28 (2000).
- <sup>136</sup> M. Arvand, S. Sohrabnezhad, M. F. Mousavi, M. Shamsipur, and M. A. Zanjanchi, "Electrochemical study of methylene blue incorporated into mordenite type zeolite and its application for amperometric determination of ascorbic acid in real samples," *Analytica Chimica Acta* **491** (2), 193-201 (2003).
- <sup>137</sup> F. D. Munteanu, L. T. Kubota, and L. Gorton, "Effect of pH on the catalytic electro oxidation of NADH using different two-electron mediators immobilised on zirconium phosphate," *Journal of Electroanalytical Chemistry* **509** (1), 2-10 (2001).
- <sup>138</sup> A. A. Karyakin, E. A. Puganova, I. A. Budashov, I. N. Kurochkin, E. E. Karyakina, V. A. Levchenko, V. N. Matveyenko, and S. D. Varfolomeyev, "Prussian Blue based nanoelectrode arrays for H<sub>2</sub>O<sub>2</sub> detection," *Analytical Chemistry* **76** (2), 474-478 (2004).
- <sup>139</sup> C. A. Pessoa, Y. Gushikem, L. T. Kubota, and L. Gorton, "Preliminary electrochemical study of phenothiazines and phenoxazines immobilized on zirconium phosphate," *Journal of Electroanalytical Chemistry* **431** (1), 23-27 (1997).
- <sup>140</sup> S. A. John and R. Ramaraj, "Microenvironment effects on the electrochemical and photoelectrochemical properties of thionine loaded Nafion (R) films," *Journal of Electroanalytical Chemistry* **561** (1-2), 119-126 (2004).
- <sup>141</sup> S. L. P. Dias, S. T. Fujiwara, Y. Gushikem, and R. E. Bruns, "Methylene blue immobilized on cellulose surfaces modified with titanium dioxide and titanium phosphate: factorial design optimization of redox properties," *Journal of Electroanalytical Chemistry* **531** (2), 141-146 (2002).
- <sup>142</sup> P. Westbroek, E. Temmerman, and P. Kiekens, "Measurement and control of hydrogen peroxide concentration in alkaline solution by means of amperometric sensor system," *Analytica Chimica Acta* **385** (1-3), 423-428 (1999).
- <sup>143</sup> B. Djuricic and S. Pickering, "Nanostructured cerium oxide: Preparation and properties of weakly-agglomerated powders," *Journal of the European Ceramic Society* **19** (11), 1925-1934 (1999).

- <sup>144</sup> A. R. Barcelo, "Hydrogen peroxide production is a general property of the lignifying xylem from vascular plants," *Annals of Botany* **82** (1), 97-103 (1998).
- <sup>145</sup> M. V. Rao, H.-i. Lee, R. A. Creelman, J. E. Mullet, and K. R. Davis, "Jasmonic Acid Signaling Modulates Ozone-Induced Hypersensitive Cell Death," *Plant Cell* **12** (9), 1633-1646 (2000).
- <sup>146</sup> A. Danon and P. Gallois, "UV-C radiation induces apoptotic-like changes in *Arabidopsis thaliana*," *Febs Letters* **437** (1-2), 131-136 (1998).
- <sup>147</sup> M. L. Orozco-Cardenas and C. A. Ryan, "Polygalacturonase beta-subunit antisense gene expression in tomato plants leads to a progressive enhanced wound response and necrosis in leaves and abscission of developing flowers," *Plant Physiology* **133** (2), 693-701 (2003).
- <sup>148</sup> S. Tsunekawa, R. Sahara, Y. Kawazoe, and K. Ishikawa, "Lattice relaxation of monosize CeO<sub>2</sub>-x nanocrystalline particles," *Applied Surface Science* **152** (1-2), 53-56 (1999).
- <sup>149</sup> V. P. Zharov, J.-W. Kim, D. T. Curiel, and M. Everts, "Self-assembling nanoclusters in living systems: application for integrated photothermal nanodiagnostics and nanotherapy," *Nanomedicine: Nanotechnology, Biology and Medicine* **1** (4), 326-345 (2005).
- <sup>150</sup> K. K. Jain, "Nanodiagnostics: application of nanotechnology in molecular diagnostics," *Expert Review of Molecular Diagnostics* **3** (2), 153-161 (2003).
- <sup>151</sup> J. L. West and N. J. Halas, "Engineered nanomaterials for biophotonics applications: Improving sensing, imaging, and therapeutics," *Annual Review of Biomedical Engineering* **5**, 285-292 (2003).
- <sup>152</sup> L. R. Hirsch, J. B. Jackson, A. Lee, N. J. Halas, and J. West, "A whole blood immunoassay using gold nanoshells," *Analytical Chemistry* **75** (10), 2377-2381 (2003).
- <sup>153</sup> J. L. West and N. J. Halas, "Applications of nanotechnology to biotechnology - Commentary," *Current Opinion in Biotechnology* **11** (2), 215-217 (2000).
- <sup>154</sup> H. Pinto-Alphandary, A. Andremont, and P. Couvreur, "Targeted delivery of antibiotics using liposomes and nanoparticles: research and applications," *International Journal of Antimicrobial Agents* **13** (3), 155-168 (2000).
- <sup>155</sup> J. L. Cleveland and M. B. Kastan, "Cancer - A radical approach to treatment," *Nature* **407** (6802), 309-311 (2000).
- <sup>156</sup> C. Tortorella, G. Piazzolla, and S. Antonaci, "Neutrophil oxidative metabolism in aged humans: A perspective," *Immunopharmacology and Immunotoxicology* **23** (4), 565-572 (2001).
- <sup>157</sup> K. Uchida, "Cellular response to bioactive lipid peroxidation products," *Free Radical Research* **33** (6), 731-737 (2000).
- <sup>158</sup> K. B. Beckman and B. N. Ames, "The free radical theory of aging matures," *Physiological Reviews* **78** (2), 547-581 (1998).
- <sup>159</sup> L. J. S. Greenlund, T. L. Deckwerth, and E. M. Johnson, "Superoxide-Dismutase Delays Neuronal Apoptosis - a Role for Reactive Oxygen Species in Programmed Neuronal Death," *Neuron* **14** (2), 303-315 (1995).
- <sup>160</sup> N. Kaul, S. Devaraj, and I. Jialal, "alpha-Tocopherol and Atherosclerosis," *Experimental Biology and Medicine* **226** (1), 5-12 (2001).

- <sup>161</sup> M. Fenech, J. Crott, J. Turner, and S. Brown, "Necrosis, apoptosis, cytostasis and DNA damage in human lymphocytes measured simultaneously within the cytokinesis-block micronucleus assay: description of the method and results for hydrogen peroxide," *Mutagenesis* **14** (6), 605-612 (1999).
- <sup>162</sup> A. Crestini, C. Zona, P. Sebastiani, M. Pieri, V. Caracciolo, L. Malvezzi-Campeggi, A. Confaloni, and S. Di Loreto, "Effects of simulated microgravity on the development and maturation of dissociated cortical neurons," *In Vitro Cellular & Developmental Biology-Animal* **40** (5-6), 159-165 (2004).
- <sup>163</sup> J. M. Lawler, W. Song, and S. R. Demaree, "Hindlimb unloading increases oxidative stress and disrupts antioxidant capacity in skeletal muscle," *Free Radical Biology and Medicine* **35** (1), 9-16 (2003).
- <sup>164</sup> R. Mittler, "Oxidative stress, antioxidants and stress tolerance," *Trends in Plant Science* **7** (9), 405-410 (2002).
- <sup>165</sup> R. R. Leker and E. Shohami, "Cerebral ischemia and trauma - different etiologies yet similar mechanisms: neuroprotective opportunities," *Brain Research Reviews* **39** (1), 55-73 (2002).
- <sup>166</sup> A. J. Maxwell, "Mechanisms of dysfunction of the nitric oxide pathway in vascular diseases," *Nitric Oxide-Biology and Chemistry* **6** (2), 101-124 (2002).
- <sup>167</sup> R. J. Carmody and T. G. Cotter, "Signalling apoptosis: a radical approach," *Redox Report* **6** (2), 77-90 (2001).
- <sup>168</sup> J. M. Carney, P. E. Starkereed, C. N. Oliver, R. W. Landum, M. S. Cheng, J. F. Wu, and R. A. Floyd, "Reversal of Age-Related Increase in Brain Protein Oxidation, Decrease in Enzyme-Activity, and Loss in Temporal and Spatial Memory by Chronic Administration of the Spin-Trapping Compound N-Tert-Butyl-Alpha-Phenylnitron," *Proceedings of the National Academy of Sciences of the United States of America* **88** (9), 3633-3636 (1991).
- <sup>169</sup> P. Callahan, J. Colon, S. Merchant, S. C. Kuiry, S. Patil, S. Seal, and B. Rzigalinski, "Deleterious effects of microglia activated by in vitro trauma are blocked by engineered oxide nanoparticles," *Journal of Neurotrauma* **20** (10), 1057-1057 (2003).
- <sup>170</sup> B. A. Rzigalinski, D. Bailey, L. Chow, S. C. Kuiry, S. Patil, S. Merchant, and S. Seal, "Cerium oxide nanoparticles increase the lifespan of cultured brain cells and protect against free radical and mechanical trauma," *Faseb Journal* **17** (4), A606-A606 (2003).
- <sup>171</sup> R. W. Tarnuzzer, J. Colon, S. Patil, and S. Seal, "Vacancy engineered ceria nanostructures for protection from radiation-induced cellular damage," *Nano Lett* **5** (12), 2573-2577 (2005).
- <sup>172</sup> E. Cohen-Jonathan, E. J. Bernhard, and W. G. McKenna, "How does radiation kill cells?," *Current Opinion in Chemical Biology* **3** (1), 77-83 (1999).
- <sup>173</sup> D. S. Pradhan, C. K. K. Nair, and A. Sreenivasan, "Radiation injury repair and sensitization of microorganisms," *Proceedings of Indian National Science Academy B* **39**, 516-530 (1973).
- <sup>174</sup> D. J. Grdina, J. S. Murley, and Y. Kataoka, "Radioprotectants: Current status and new directions," *Oncology* **63**, 2-10 (2002).
- <sup>175</sup> C. K. K. Nair, D. K. Parida, and T. Nomura, "Radioprotectors in radiotherapy," *Journal of Radiation Research* **42** (1), 21-37 (2001).
- <sup>176</sup> Y. Matsumura and H. N. Ananthaswamy, "Toxic effects of ultraviolet radiation on the skin," *Toxicology and Applied Pharmacology*

Toxicology of the Skin **195** (3), 298-308 (2004).

- <sup>177</sup> M. Wlaschek, I. Tantcheva-Poor, L. Naderi, W. Ma, L. A. Schneider, Z. Razi-Wolf, J. Schuller, and K. Scharffetter-Kochanek, "Solar UV irradiation and dermal photoaging," *Journal of Photochemistry and Photobiology B: Biology* **63** (1-3), 41-51 (2001).
- <sup>178</sup> H. Yasui and H. Sakurai, "Chemiluminescent detection and imaging of reactive oxygen species in live mouse skin exposed to UVA," *Biochemical and Biophysical Research Communications* **269** (1), 131-136 (2000).
- <sup>179</sup> B. A. Jurkiewicz and G. R. Buettner, "EPR detection of free radicals in UV-irradiated skin: Mouse versus human," *Photochemistry and Photobiology* **64** (6), 918-922 (1996).
- <sup>180</sup> H. Masaki, T. Atsumi, and H. Sakurai, "Detection of Hydrogen-Peroxide and Hydroxyl Radicals in Murine Skin Fibroblasts under Uvb Irradiation," *Biochemical and Biophysical Research Communications* **206** (2), 474-479 (1995).
- <sup>181</sup> G. Wakefield and J. Stott, in *Soap, Perfumery & Cosmetics* (2005), Vol. SPC 0405, pp. 41-44.
- <sup>182</sup> M. Gerlach, D. Benshachar, P. Riederer, and M. B. H. Youdim, "Altered Brain Metabolism of Iron as a Cause of Neurodegenerative Diseases," *Journal of Neurochemistry* **63** (3), 793-807 (1994).
- <sup>183</sup> B. Halliwell, "Reactive Oxygen Species and the Central-Nervous-System," *Journal of Neurochemistry* **59** (5), 1609-1623 (1992).
- <sup>184</sup> M. Das, N. Bhargava, C. Gregory, L. Riedel, P. Molnar, and J. J. Hickman, "Adult rat spinal cord culture on an organosilane surface in a novel serum-free medium," *In vitro cellular & developmental biology. Animal.* **41** (10), 343-348 (2005).
- <sup>185</sup> P. H. Evans, "Free-Radicals in Brain Metabolism and Pathology," *British Medical Bulletin* **49** (3), 577-587 (1993).
- <sup>186</sup> J. A. Dykens, A. Stern, and E. Trenkner, "Mechanism of Kainate Toxicity to Cerebellar Neurons In vitro Is Analogous to Reperfusion Tissue-Injury," *Journal of Neurochemistry* **49** (4), 1222-1228 (1987).
- <sup>187</sup> E. W. Kellogg and I. Fridovich, "Liposome Oxidation and Erythrocyte Lysis by Enzymically Generated Superoxide and Hydrogen-Peroxide," *Journal of Biological Chemistry* **252** (19), 6721-6728 (1977).
- <sup>188</sup> T. H. Margrain, M. Boulton, J. Marshall, and D. H. Sliney, "Do blue light filters confer protection against age-related macular degeneration?," *Progress in Retinal and Eye Research* **23** (5), 523-531 (2004).